Humboldt Universität zu Berlin – Geographisches Institut

Dissertation

Pedogenic iron oxide determination of soil surfaces from laboratory spectroscopy and HyMap image data

A case study in Cabo de Gata-Níjar Natural Park, SE Spain

zur Erlangung des akademischen Grades

doctor rerum naturalium

eingereicht von

Nicole Richter

an der Mathematisch-Naturwissenschafltichen Fakultät II

der Humboldt-Universität zu Berlin

Dekan: Prof. Dr. Peter Frensch

Gutachter

Prof. Dr. Patrick Hostert

Prof. Dr. Hermann Kaufmann

Prof. Dr. Eyal Ben-Dor

eingereicht am 21. August 2009

Datum der Promotion: 20. Januar 2010

Acknowledgements

First of all I would like to thank *Prof. Herrmann Kaufmann* and *Dr. Sabine Chabrillat* for the opportunity to work on this project and being my supervisors from the very beginning. I am especially grateful to *Sabine* for keeping work not related to the project off my desk and giving me the freedom to focus on the research. Her guidance in the field, intensive discussions and valuable suggestions improved the quality of this thesis.

I am deeply thankful to *Dr. Thomas Jarmer* for his continuous interest in this work, for sharing his knowledge and intensive discussions about soils, spectroscopy and statistics. His approach to scientific working, encouragement and support have been of great value for the successful completion of the thesis.

Prof. Cecilio Oyonarte from the University Almeria is appreciated for funding and performing the soil samples chemical analysis within the *Incamar Project*, for technical support of the field work, sharing his knowledge of the study site and enabling a five week research stay in Almeria.

Acknowledgements are due to *Prof. Patrick Hostert* for being available as supervisor and giving me the opportunity to submit the thesis at the Humboldt University. Through our discussions and his initiative to meet *Thomas* the thesis was pushed to a stage where it could be completed.

I wish to extend my warmest thanks to all my colleagues from the remote sensing section of the GFZ Potsdam. *Dr. Jan Anderssohn* and *Daniel Spengler* are gratefully acknowledged for being great officemates and friends, for all the fruitful discussions and nice chats over a beer. Thanks for an unforgettable PhD time! *Sylvia Magnussen* is thanked for her assistance with all types of technical problems - at any time, and *Dr. Karl Segl* for discussions and his little software tools that were faster programmed than I could wish for.

My warmest thanks go to *Andrea Neumann* for her help with optical measurements, discussions and invaluable field assistance. The field work would not have been accomplished in time without her help. Thanks also for showing me around in Berlin, long open talks and always being there in the phases of frustration. It will not be forgotten.

I am grateful to *Dr. Martin Bachmann* from the DLR for HyMap data processing and μMESMA calculations, the *EU Desurvey-IP Project* under leadership of *Prof. Juan Puigdefabregas* for generous funding of the project and *Prof. Eyal Ben-Dor* for being available as referee for this thesis.

The support and encouragement of my family and friends were invaluable for completing this thesis. I want to thank in particular *Birgit*, *Christiane* and *Trond* for continuous moral support, understanding the problems of a PhD student and finding numerous arguments against giving up;

Dorothea and *Silke* for the great time singing together and enjoying Italian food on Monday night;

Arthur, *Luise*, *Johannes*, *Tim*, *Milo*, and *Ruth*, the newborn babies of family and friends, for the wonderful hours together that cleared my mind;

My family and *family Naumann* for their love, trust and encouragement;

My parents for their love, care, support and for funding me all those years that I could finish my education and realize my dreams.

For those of you whom I forgot to thank, my true apologies, please be assured that your support is highly appreciated.

Finally, I am forever indebted to *Marcel* for his endless patience reading the manuscript and transforming my abstract "pseudo-english" structures into better understandable sentences and paragraphs. Without his love, encouragement, support and him just being there, this thesis would still not be finished. I am sure he is just as happy that I finished the project.

Viva la vida!

Abstract

The knowledge of the soil condition and development is decisive when characterizing and monitoring the change of ecosystems. The global presence of iron oxides and their highly variable concentration and mineralogy reflecting different soil conditions make them a suitable indicator. Optical remote sensing methods are employed to determine and map the soil iron oxide concentrations on the example of the Cabo de Gata-Níjar Natural Park, a semi-arid ecosystem in SE Spain. In an initial laboratory spectroscopy study, a methodology is developed that links iron oxide content (Fe_d, citrate-dithionite extractable iron oxides) with iron spectral absorption bands. Texture-dependent Fe_d prediction models are developed for sand- and clay-silt-dominated samples. They yield highly accurate estimations with less than 15 % prediction error. Similar accuracies are achieved from texture-independent models.

Texture-independent models are applied to the HyMap image data because a pixel-wise determination of the predominating soil texture is not possible. However, the spatial distribution of Fe_d concentration in the study area is determined with comparable accuracy as in the laboratory. Laboratory analysis of vegetation vitality and density impact on the soil reflectance spectra and Fe_d prediction accuracy has shown that reliable estimations are possible until about 20 % leaf cover. Accordingly, three Fe_d prediction accuracy levels are defined based on the joint detectability of vegetation and iron absorption features. The final Fe_d prediction map is used to evaluate the current soil conditions and identify potentially eroded soils surfaces. The present method has due to low complexity a high potential for the global monitoring of such sensitive areas from current and future spaceborne sensors.

Zusammenfassung

Kenntnisse über den Zustand und die Entwicklung von Böden sind entscheidend für die Charakterisierung von Ökosystemen und deren Veränderungen. Die weltweite Verbreitung von Eisenoxiden und ihre von der Bodenentwicklung abhängige Konzentration und mineralogische Zusammensetzung machen sie zu geeigneten Indikatoren. Methoden der optische Fernerkundung wurden angewandt, um am Beispiel des Cabo de Gata-Níjar Naturparks, einem semi-ariden Ökosystem in Südostspanien, die Konzentrationen von Eisenoxiden im Boden zu bestimmen und zu kartieren. In der zuerst durchgeführten labor-spektroskopischen Studie wurde eine Methode entwickelt, welche den Eisenoxidgehalt (Fe_d, Citrat-Dithionit extrahierbares Eisenoxid) mit den Eisenabsorptionsbanden verknüpft. Korngrößenabhängige Fe_d-Vorhersagemodelle wurden sowohl für sand- als auch ton-schluff-haltige Proben erstellt. Beide liefern hochgenaue Schätzungen mit weniger als 15% Vorhersagefehler. Ähnliche Werte wurden für korngrößenunabhängige Modelle erreicht.

Korngrößenunabhängige Modelle wurden zur Analyse der HyMap-Bilddaten verwendet, da eine pixelbezogene Bestimmung der vorherrschenden Bodentextur nicht möglich war. Die räumliche Verteilung der Fe_d Konzentration im Untersuchungsgebiet wurde mit einer den Laborergebnissen vergleichbaren Genauigkeit bestimmt. Laboruntersuchungen zum Vegetationseinfluss in Bezug auf Vitalität und Bedeckungsgrad auf die Bodenreflektions-spektren und die Fe_d Vorhersagegenauigkeit zeigten, dass zuverlässige Abschätzungen bis zu einer Vegetationsbedeckung von ca. 20 % möglich sind. Dementsprechend wurden drei Vorhersagegenauigkeitsklassen definiert, basierend auf der gemeinsamen Detektierbarkeit von Vegetation und Eisenabsorptionsbanden im Bildpixel. Die abgeleitete Fe_d Verteilungs-karte dient der Einschätzung des vorliegenden Bodenzustands und dem Ausweisen von erodierten Oberflächen. Die entwickelte Methode hat aufgrund ihrer Einfachheit ein großes Potential für ein globales Monitoring von sensitiven Gebieten unter der Verwendung von gegenwärtig verfügbaren als auch zukünftigen satellitengestützten Sensoren.

Contents

Acknowledgements		i
Abstract		iii
Zusammenfassung		v
Contents		vii
List of Figures		xi
List of Tables		xv
Abbreviations		xvii
Chapter 1:	**Introduction and objectives**	**1**
Chapter 2:	**Fundamentals of soil remote sensing**	**5**
2.1	Interaction of radiation and soil surfaces	5
2.1.1	Mechanisms of absorption	6
2.1.2	Geometrical considerations	8
2.2	Reflectance properties of pedogenic iron oxides	9
2.3	Effects of other soil constituents on soil reflectance	11
2.3.1	Mineral composition	12
2.3.2	Soil organic matter	13
2.3.3	Soil moisture	14
2.4	Natural parameters affecting soil reflectance	15
2.4.1	Soil texture and surface roughness	15
2.4.2	Vegetation coverage	16
Chapter 3:	**Study area**	**19**
3.1	Landscape evolution	20
3.2	Climate	22
3.3	Soils	22
3.4	Vegetation and land use	27

Chapter 4:	**Materials and methods**	**31**
4.1	Soil sampling and chemical analysis	31
4.2	Spectrometric data	34
4.2.1	Laboratory data	34
4.2.2	Hyperspectral image data	37
4.3	Spectral absorption feature analysis	41
4.3.1	Spectral feature extraction	41
4.3.2	Modeling and validation	42
Chapter 5:	**Laboratory spectral determination of pedogenic iron oxide content**	**45**
5.1	Statistical description of soil samples	46
5.1.1	Rock and soil XRF analysis	46
5.1.2	Soil quantitative chemical analysis	49
5.1.3	Texture analysis	50
5.2	Spectral influence of soil physicochemical properties on surface reflectance	52
5.2.1	Pedogenic iron oxides	52
5.2.2	Soil organic carbon (SOC)	57
5.2.3	Clay mineralogy	57
5.2.4	Soil texture	58
5.3	Modeling pedogenic iron oxide content	60
5.3.1	Relationships between Fe_d content and spectral iron features	60
5.3.2	Texture-dependent models	63
5.3.3	Texture-independent models	66
5.4	Vegetation influence on Fe_d modeling	67
5.4.1	Leaf cover experiment	68
5.4.2	Impact on Fe-VIS absorption	70
5.4.3	Impact on Fe-NIR absorption	71
5.4.4	Impact on Fe_d prediction accuracy	74
Chapter 6:	**Mapping pedogenic iron oxide from hyperspectral image data**	**77**
6.1	Spectral absorption features extraction	77
6.2	Transferring laboratory model to image data	81
6.2.1	Location and assignment of soil samples in the image	81
6.2.2	Soil texture influence	82
6.2.3	Comparison of laboratory and image soil spectra	83
6.3	Determining pedogenic iron oxide content	86
6.4	Evaluating vegetation impact on Fe_d prediction accuracy	88
6.5	Spatial distribution of pedogenic iron oxides	91
6.5.1	Development of soil iron surface map and prediction accuracy	91
6.5.2	Fe_d concentration as pedogenic indicator	95

Chapter 7: Discussion **101**
7.1 Modeling assumptions 101
7.2 Model evaluation 102
7.2.1 Model variables 102
7.2.2 Calibration range 105
7.2.3 Model performance 105
7.3 Sensor-related impact factors 108
7.3.1 Spatial and spectral resolution 108
7.3.2 SNR and radiometric resolution 109
7.3.3 Atmospheric correction 110
7.3.4 View conditions 111
7.4 Soil surface-related impact factors 112
7.4.1 Soil texture and surface roughness 112
7.4.2 Vegetation cover 115

Chapter 8: Conclusion and outlook **119**

Chapter 9: References **125**

List of Figures

Figure 2.1: Different kinds of reflection. 8

Figure 2.2: Schematic view of the energy levels. 9

Figure 2.3: Reflectance spectra of different iron oxides. 10

Figure 2.4: Bidirectional reflectance spectra of clay minerals and carbonates. 13

Figure 2.5: Bidirectional reflectance spectra of three soils with different level of decomposition. 13

Figure 2.6: Laboratory spectra of soil samples (quaternary sand) with different moisture percentages. 14

Figure 2.7: Reflectance spectra of soils with different predominate particle size. 15

Figure 2.8: Reflectance spectra of photosynthetic and non-photosynthetic active vegetation. 17

Figure 3.1: Location of study area. 19

Figure 3.2: Geological map of Rodalquilar area. 21

Figure 3.3: Climate diagram from Almería station for the year 2005. 22

Figure 3.4: Soil type map of the study area. 23

Figure 3.5: Transition from reddish volcanic to grayish-white carbonatic soils due to change of geological parent material. 25

Figure 3.6: Quaternary alluvial fan near La Isleta. 26

Figure 3.7: Profile of Calcic Luvisol at the Qf1 surface of the La Isleta alluvial fan. 26

Figure 3.8: Overview of main plant species in the study area. 28

Figure 3.9: Overview of agricultural region in Cortijo del Fraile. 29

Figure 3.10: Renaturation of abandoned cultivated areas: *Ziziphus* plantation near the village La Isleta del Moro. 30

Figure 3.11: Typical series of vegetation types along a slope after abandonment of cultivation and beginning vegetation succession. 30

Figure 4.1: Pictures of one sample before (2-mm sieved fraction) and after homogenization. 33

Figure 4.2: Setup for spectral measurement in the laboratory. 35

Figure 4.3: Pictures of iron-dominated soil surface with about dry, green and mixed grass leaf coverage. 36

Figure 4.4: Evaluation of geometric correction by field GPS measurements. 38

Figure 4.5: Evaluation of radiometric calibration. 40

Figure 4.6: Scheme of hull-normalization (continuum removal). 41

Figure 5.1: XRF results for volcanic and carbonatic rock and soil samples. 47

Figure 5.2: Soil chemical composition of 33 volcanic (volc), 5 carbonatic (carb) and 12 soil samples from the transition between volcanic and carbonatic bedrock (trans volc/carb). 50

Figure 5.3: Particle size distribution and indicated soil texture groups of all samples. ... 51

Figure 5.4: Influence of different Fe_d contents on iron absorption bands. 54

Figure 5.5: Relationship between Fe_d content and hull-normalized Fe-VIS and Fe-NIR absorption features. 55

Figure 5.6: Relationship between Fe_d content and area and width of Fe-VIS and Fe-NIR absorption band. 56

Figure 5.7: Spectral influence of high SOC concentration on soil reflectance. 57

Figure 5.8: Comparison of reflectance and hull-normalized spectra of non-heated and heated soil samples. 58

Figure 5.9: VIS/NIR reflectance and hull-normalized spectra of two soil samples with two different processed grain sizes fractions (2-mm sieved and homogenized). 59

Figure 5.10: Relationships between Fe_d and hull-normalized Fe-VIS and Fe-NIR depth in logarithmic data space. 62

Figure 5.11: Cross-validated results of texture dependent Fe_d prediction models based on Fe-NIR absorption depth. 64

Figure 5.12: Cross-validated results of texture dependent Fe_d prediction models based on Fe-VIS absorption depth. 65

Figure 5.13: Cross-validated results of texture independent Fe_d prediction models. 67

Figure 5.14: VIS/NIR reflectance spectra of leaf cover experiments with increasing dry (NPV), green (PV) and mixed (MIX) leaf cover. 69

Figure 5.15: Relationships between normalized Fe-VIS and Fe-NIR absorption depths and wavelength position and leaf cover (PV, NPV, MIX). 71

Figure 5.16: Spectral impact of increasing PV cover on hull-normalized iron absorption bands. 72

Figure 5.17: Relationships between leaf cover and normalized Fe-NIR absorption depth and cellulose absorption depth. 73

Figure 5.18: Potential underestimation of Fe_d concentration for partial leaf cover on soil surface (Fe-VIS and Fe-NIR texture-independent models). 74

Figure 6.1: Maps of extracted soil and vegetation-related absorption features. 80

Figure 6.2: Soil texture influence on normalized Fe-NIR absorption depth in laboratory and image spectra. 83

Figure 6.3: Comparison of samples laboratory and image Fe-NIR absorption, and laboratory model performance. 84

Figure 6.4: Hull-normalized Fe-NIR absorption feature: comparison of image and laboratory (homogenized and 2-mm sieved) spectra for selected samples. .. 85

Figure 6.5: Relationship between Fe_d content and normalized Fe-NIR depth of 876 nm spectral band. 87

Figure 6.6: Image-calibrated Fe_d prediction model: scatter plot of the cross-validated results. 88

Figure 6.7: Fe_d prediction results for pure soil and vegetation-influenced soil samples. 89

Figure 6.8: Spatial distribution of pedogenic iron oxide (Fe_d) concentration. 93

Figure 6.9: Prediction accuracy of Fe_d modeling. 94

Figure 6.10: Characterization of a natural soil profile (road cut) on the alluvial fan near the village La Isleta del Moro. 96

Figure 6.11: Map of potentially capped soil profiles near Casas los Precillas based on joint occurrence of pedogenic iron oxides and carbonates on the soil surfaces. 97

Figure 6.12: Map of potentially capped soil profiles near La Isleta de Moro based on joint occurrence of pedogenic iron oxides and carbonates on the soil surfaces. 98

Figure 6.13: Characteristic geomorphologic surface types of the La Isleta alluvial fan. .. 99

Figure 6.14: Fe_d content map of La Isleta alluvial fan with delimitated fan surface age groups integrated from Harvey et al. (1999). 100

Figure 7.1: Correlation spectra for Fe_d content. 103

Figure 7.2: Impact of different SNR to Fe_d prediction. 110

Figure 7.3: Location of the soil samples across the image. 112

Figure 7.4: Image model results for texture-dependent and independent soil sample groups. 113

Figure 7.5: Fe_d modeling results indicating µMESMA fractional vegetation cover. 117

List of Tables

Table 4.1: Summary of soil samples classified by parent material and land use. 32

Table 4.2: Characteristics of ASD Field Spectrometer. 34

Table 4.3: Summary of HyMap data acquisition (asl = above sea level). 37

Table 4.4: Absorption maximum position and wavelength ranges of soil and vegetation spectral features for automatic extraction procedure. 42

Table 5.1: XRF analysis of typical volcanic materials in the study area. 48

Table 5.2: Descriptive statistics of chemical analysis results for all 50 soil samples and test of normality. 49

Table 5.3: Soil texture variability in the sand-dominated and clay-silt-dominated groups. 51

Table 5.4: Literature values of ferric ion absorption maxima in the VIS/NIR (Hm = hematite, Gt = goethite). 52

Table 5.5: Laboratory wavelength position of iron absorption maxima in the VIS/NIR range. 53

Table 5.6: Coefficient of determination (R^2) for Fe_d content and selected hull-normalized spectral features calculated in linear and n-log transformed data space. 61

Table 6.1: Comparison of Fe_d model performance for cross-validated pure soil samples and vegetation samples. 90

Table 7.1: Summary of Fe_d prediction results from laboratory study (Fe-NIR only) and HyMap image data on volcanic soils. 106

Abbreviations

ASD	analytical spectral devices
asl	above sea level
DEM	digital elevation model
DLR	Deutsches Zentrum für Luft- und Raumfahrt (German Aerospace Center)
ENVI	ENvironment for Visualizing Images (image analyzing software)
Fe_d	citrate-dithionite extractable iron oxide content
Fe-NIR	iron absorption band in the near infrared spectrum ($^6A_{1g} \rightarrow {}^4T_{1g}$)
Fe_o	oxalate-soluble iron oxides content
Fe_t	total iron oxide content
Fe-VIS	iron absorption band in the visible infrared spectrum ($^6A_{1g} \rightarrow {}^4A_{1g}, {}^4E$)
FOV	field of view
GFZ	Helmholtz Zentrum Potsdam, Deutsches GeoForschungsZentrum GFZ (German Research Centre for Geosciences)
HyMap	Hyperspectral Mapper
MIX	mixture of photosynthetic and non-photosynthetic active vegetation
N	number (of)
n-log	natural logarithmus
NIR	near infrared wavelength range
NPV	non-photosynthetic active vegetation
NSMI	Normalized Difference Soil Moisture Index
PV	photosynthetic active vegetation
R	Pearson's correlation coefficient
R^2	coefficient of determination
rel. RMSE	relative root mean-squared error
RMSE	standard error of prediction
RPD	residual prediction deviation
S.D.	standard deviation
SMA	spectral mixture analysis
SNR	signal to noise ratio
SOC	soil organic content
SWIR	short-wave infrared wavelength range

UTC	coordinated universal time
UTM	universal transverse mercator
UV	ultraviolet wavelength range
v	index added for cross-validated results
VIS	visible wavelength range
XRF	X-ray fluorescence
α	absorptance
ρ	reflectance
τ	transmittance
μMESMA	iterative multiple endmember spectral mixture analysis

Chapter 1: **Introduction and objectives**

Soils are important elements of land surface ecosystems. Characterizing these ecosystems and monitoring their changes requires an accurate knowledge of the soil development. As pedogenesis is an ongoing process driven by various factors including climate, geology, geomorphology and vegetation, changed environmental conditions may consequently lead to different soil development. This will be reflected in the soils physicochemical properties (Birkeland 1999; Malley et al. 2004).

The semi-arid Mediterranean areas are sensitive ecosystems, where major changes in the soil-vegetation system are expected to occur with changing climate. The rising anthropogenic pressure and expansion of intensive agriculture have already increased the lands vulnerability to soil degradation processes (Perez-Trejo 1994; Latorré et al. 2001). Suitable indicators are required for locating and monitoring of over-exploited regions. They need to be readily observable over large areas and must allow for quantitative measurement and regular updating (Diouf and Lambin 2001).

In this context, iron oxides are of great pedological interest because their content and mineralogical composition reflect the duration and intensity of pedogenesis (Arduino et al. 1986; Bech et al. 1997). The global presence of iron oxides makes them a suitable pedogenic indicator (Cornell and Schwertmann 1996). Pedogenic iron oxides form primarily as weathering products from parent rocks with iron-bearing mineralogy. They remain close to the site of weathering and can precipitate as coatings on other soil particles or cementing agents. Their continuous accumulation in the soil profile during pedogenesis produces intense colors (Birkeland 1999).

Soil colors have been used in various studies to assess the iron oxide mineralogy and content to describe soil development and discriminate between soils (Torrent et al. 1983; Scheinost and Schwertmann 1999; Fontes and Carvalho Jr. 2005). However, soil color is

affected by numerous soil properties such as moisture content and mineralogical, organic, and textural composition (Stoner et al. 1980). Alternative measurements that are less biased by other soil properties are needed to determine the iron oxide content.

Such a promising approach is the application of reflectance spectroscopy and in particular the associated spectral absorption feature analysis. It uses diagnostic absorption bands in the reflectance spectrum that are result of material specific dielectric properties. These wavelength-dependent properties generate a unique spectral reflectance signature from which materials can be characterized and distinguished (Clark 1995; Ben-Dor et al. 1999).

The fact that soil spectral reflectance characteristics are influenced by soil properties such as the presence of iron oxides is well-known (Baumgardner et al. 1985). For the description and quantification of soil properties, spectral reflectance measurement is a timesaving, less expensive and non-destructive alternative to conventional methods. It allows a reasonable estimation and is especially useful, when large numbers of samples and analyses are required (Malley et al. 2004; Brown et al. 2006; McBratney et al. 2006).

Measurements of the spectral reflectance are commonly performed in laboratory, field, from air or space. Controlled laboratory conditions are most advantageous for analyzing the relationships between materials and their absorption characteristics, subsequent model development and input parameter derivation. Here, typical difficulties of field measurements like varying viewing geometry, lighting conditions, surface roughness and vegetation can be minimized or even ruled out (Ben-Dor et al. 1999). This is of special interest because absorption characteristics in soils are often much weaker developed than in pure substances due to lower concentrations.

Although feasible, ground-based data collection and subsequent laboratory spectroscopic analysis is in practice not suitable for mapping spatial variation of soil properties over wide regions. Instead hyperspectral remote sensing sensors with spatial synoptic view overcome these limitations and can monitor soil conditions over large areas. The high spectral resolution of these sensor systems compared to current multispectral systems facilitates the transferability and applicability of laboratory findings. The suitability of reflectance spectroscopy on remote sensing scale for the determination of soil properties has been shown in various studies e.g. Palacios-Orueta and Ustin (1998); Bullard and White (2002); Ben-Dor et al. (2006); Bartholomeus et al. (2007).

When measuring natural soil surfaces, their reflectance characteristics are influenced by a number of parameters. Soil texture for example has an impact on the albedo and intensity of the absorption bands (van der Meer 1995). Vegetation can diminish or totally mask the soils spectral response (Richter et al. 2006). The spectral behavior of soil-vegetation mixtures has been studied repeatedly but mostly focusing on the soil impact on spectral characterization of photosynthetic active vegetation e.g. Huete (1987). However, the largely open soils in semi-arid and arid regions are dominated by dry non-photosynthetic plants apart from a short green season. A thorough investigation on the effects of vegetation density and vitality on soil spectral characterization has rarely been performed until now.

Based on the above described problematic, the following research questions arise:

1. Can reflectance spectroscopy be used to predict accurately pedogenic iron oxide content?

2. Can hyperspectral remote sensing be used to map and monitor key soil iron oxide parameter more accurately in a quantitative way?

3. Which impact has soil texture on the predictability of pedogenic iron oxide concentration?

4. What is the influence of vegetation cover in a semi-arid environment for the remote sensing of pedogenic iron oxide content?

This thesis was performed in the frame of the EU project DeSurvey-IP "A Surveillance System for Assessing and Monitoring of Desertification". The first part of the manuscript (chapter 1 to 4) describes the background of the study, test site and methods used. The second part (chapter 5) covers laboratory studies to develop a prediction model for pedogenic iron oxides and to evaluate the impact of soil texture and vegetation cover and status. The iron model and soil texture impact was published in Richter et al. (2009). The third part of the manuscript (chapter 6) deals with the application of the model on airborne hyperspectral image data and soil texture and vegetation impacts on the prediction accuracy. The spatial distribution of pedogenic iron oxide concentration in the Cabo de Gata-Níjar Natural Park is derived. In the fourth part (chapter 7 and 8) model performance, natural surface and sensor related impact factors are assessed, potential new application fields for the developed model are indicated and final conclusions are drawn.

Chapter 2: **Fundamentals of soil remote sensing**

2.1 Interaction of radiation and soil surfaces

Remote sensing of soils and other materials (minerals and vegetation) uses predominately the electromagnetic spectrum between 400 and 2500 nm for material identification and determination of chemical and mineralogical characteristics. In this wavelength region, covering the visible (VIS: 400-700 nm), near infrared (NIR: 700-1100 nm) and short-wave infrared (SWIR: 1100-2500 nm), important interactions between radiation and material occur at the atomic and molecular level stimulating material specific absorption.

Three main processes occur when electromagnetic radiation (e.g. sun light, lamp) interacts with the Earth's surface. Parts of the incident energy ($E_i(\lambda)$) can be reflected ($E_r(\lambda)$), absorbed ($E_a(\lambda)$), or transmitted ($E_t(\lambda)$) by the surface as a function of its unique characteristics and the wavelength at which it is observed:

$$E_i(\lambda) = E_r(\lambda) + E_a(\lambda) + E_t(\lambda) \quad 2\text{-}1$$

When dividing each of the energy quantities by the incident energy

$$\frac{E_i(\lambda)}{E_i(\lambda)} = \frac{E_r(\lambda)}{E_i(\lambda)} + \frac{E_a(\lambda)}{E_i(\lambda)} + \frac{E_t(\lambda)}{E_i(\lambda)} \quad 2\text{-}2$$

the dimensionless reflectance ρ, absorptance α, and transmittance τ, can be derived

$$1 = \rho + \alpha + \tau \quad 2\text{-}3$$

According to the law of conservation of energy, the sum of the three components equals one but their magnitudes are not constant, and will vary with wavelength.

2.1.1 Mechanisms of absorption

The spectroscopy of soils is limited to the immediate soil surface as there is very little penetration of electromagnetic energy through the opaque soil medium. The bidirectional reflectance spectrum of a soil reflects its heterogeneous mixture of different chemical constituents (mineral and organic) and physical properties (particle size, soil moisture). The soil constituents show distinct material-specific features which are caused generally by two different types of processes; electronic or vibrational transition. Electronic processes comprise transitions between electronic energy levels of the constituent metal and/or impurity ions, transitions between such energy levels after modifying them from those of the free ion by interaction with crystal or ligand fields and so-called charge transfer where an electron is transferred from one ion to another. Vibrational processes are the excitation of overtones and combination tones of the fundamental (normal) modes of anion groups (OH^-, CO_3^{2-} SO_4^{2-}) and molecules (e.g. H_2O, CO_2) in the crystal lattice including vibrations of such groups as a whole against the lattice structure (Hunt and Salisbury 1970).

In the following a short overview will be given of the main electronic and vibrational processes that produce features relevant for soil spectroscopy investigations. The descriptions are based on the work of Hunt and Salisbury (1970); Hunt (1977); Geerken (1991) and Clark (1999).

Electronic processes (VIS/NIR region)

Crystal field effects produce features in the VIS/NIR (in exception until 1800 nm) due to electron transition between the discrete energy states of atoms and ions. The absorption or emission of specific wavelengths of the electromagnetic radiation takes place as changes from one energy state to another occur. In solids, the electronic levels of the isolated ion may be split and displaced by interaction with the surrounding crystal field. In case of all transition metals, in particular iron, the unfilled *d*-orbitals, which have almost identical energies in the isolated free ion, interact with the surrounding ions and as a result assume different energies. The main features of the spectrum are primarily determined by valence state of the ion (Fe^{2+}, Fe^{3+}), its coordination number and the site symmetry (Hunt and Salisbury 1970).

Charge transfer bands describe inter-element electron transitions where the absorbed energy causes an electron to migrate between ions or between ions and ligands. Such transitions can also occur between adjacent ions of the same metal in different valence states (e.g. between Fe^{2+} and Fe^{3+}). The absorption features produced by charge transfer are

usually hundred to thousand times more intense than those of crystal field transitions. High energies are required to stimulate the charge transfer processes; hence the appearing absorption maxima of most metals are located in the ultraviolet (UV) wavelength region, and wings of the band extending into the visible. The red color of iron oxides and hydroxides are mainly caused by charge transfer absorption (Hunt 1977; Geerken 1991; Clark 1999).

Vibrational processes (SWIR region)

Vibrational induced absorption bands appear when the ions in a molecule or crystal lattice are stimulated to vibrate. The frequency of the vibration depends on the strength of the bond between the ions and their mass. A molecule with N ions has 3N-6 normal modes of vibration, so called *fundamentals*. The frequencies of fundamental vibrations are traditionally labeled with the Greek letter v and a subscript, v_1, v_2, etc. *Overtone* modes (e.g. labeled $2v_1$, $3v_1$) are multiples of the single fundamental mode, and *combination* modes (e.g. v_1+v_2, v_1+2v_3) combine different modes of vibration. Typically, each higher overtone or combination is 30 to 100 times weaker than the previous (Clark 1999). The characteristic and intensive fundamental vibration bands occur at wavelength > 3000 nm and thus are located outside the spectral range investigated in the study. The overtones and combinations produce mineral-specific narrow absorption bands between 1000 and 2500 nm which allow the diagnostic analysis of the spectral data. But vibrational absorption band in the infrared spectrum appears only when the molecule responsible shows a dipole moment (Geerken 1991; Clark 1999). There are a few specific molecules which produce these absorption: water, hydroxyl (OH^-) groups either free or bond in mineral lattice (e.g. in clays, iron hydroxides), and the CO_3^{2-} ion of carbonates.

Water and OH^- produce particularly diagnostic absorption bands in almost all materials. Water has 3 fundamental vibrations which are v_1, symmetric OH^- stretch at 3106 nm, v_2, H-O-H bend at 6079 nm, and v_3, asymmetric OH^- stretch at 2903 nm. In the reflectance spectra of vegetation where water molecules appear isolated, vibrational bands occur at 1875 nm (v_2+v_3), at 1454 nm ($2v_2+v_3$), 1379 nm (v_1+v_3), at 1135 nm ($v_1+v_2+v_3$) and at 942 nm ($2v_1+v_3$). In mineral and soil spectra, absorption feature appears near 1400 nm ($2v_3$) and 1900 nm (v_2+v_3) (Hunt and Salisbury 1970). The appearance of the 1400 nm absorption band in minerals alone indicates that OH^- is present only, whereas the 1900 nm band is an indication for molecular water. The OH^- group in minerals is typically attached to metal ions and produces very diagnostic features between 2200 to 2300 nm due to the

combination mode of metal-OH bend and OH^- stretching (Hunt and Salisbury 1970; Clark 1999).

The fundamental vibrational modes of CO_3^{2-} ion are v_1, symmetric stretch 9407 nm, v_2, the out-of-plane bend at 11400 nm, v_3, the asymmetric stretch at 7067 nm, and v_4, the in-of-plane bend at 14700 nm (Clark 1999). Combination and overtone modes produce absorption bands in the near-infrared reflectance spectrum bands. The two strongest features appear at 2500-2550 nm (v_1+2v_3) and 2300-2350 nm (3v_3). Three weaker bands occur near 2120-2160 nm (v_1+2v_3+v_4 or 3v_1+2v_4), 1970-2000 nm (2v_1+2v_3), and 1850-1870 nm (v_1+3v_1) (Hunt and Salisbury 1971; Clark 1999). Gaffey (1986) identified additional two weaker bands between 1600 and 1800 nm.

2.1.2 Geometrical considerations

The radiation reaching the detector is not only influenced by the absorption of the material but also by the complex reflectance characteristics of the surface. There are two general ways in which the incident radiation is returned from a surface (Figure 2.1). In the first case the incident radiation is reflected with the angle of reflection equal to the angle of incidence (specular reflection). These specular reflectors are flat surfaces that act like a mirror. The other case characterizes rough surfaces that reflect the incident radiation uniformly in all directions (diffuse reflection). An ideal diffuse (isotropic) surface, also called Lambertian surface, reflects the incident radiation constantly for any angle of reflection. However, most earth surfaces reflect incident radiation neither perfectly specular nor diffuse but differently with varying observation angle. The proportion of reflecting (single-scattered) and diffuse (multiple-scattered) reflection depends on surface roughness, the wavelength and the illumination and observation geometry. Further specific parameters of the participating minerals such as the internal absorption and scattering coefficients are important.

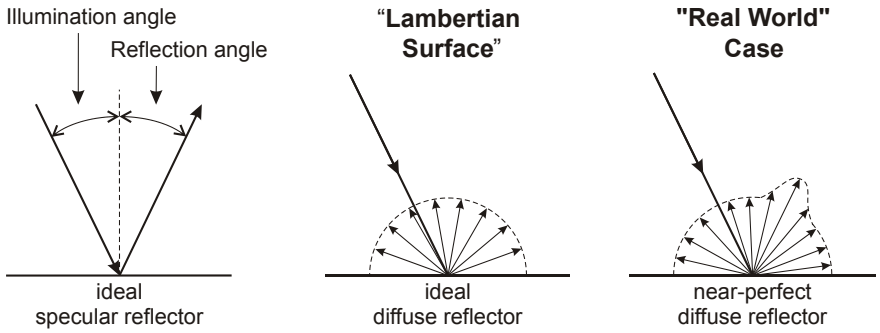

Figure 2.1: Different kinds of reflection (modified after Lillesand and Kiefer (1994)).

Under constant illumination and observation conditions, surface roughness, particle shape and orientation affect the preferred direction of reflection. A modification of these parameters causes different reflection intensity. Small particles or arranged particle orientation lead to a smoother surface and increasing portion of the specular reflection. Conversely, interparticle spaces caused by increasing particle size or uniform particle distribution lead to higher absorption of incident radiation and increased portion of the multiple-scattered reflection. In addition, changes in the compactness of packing or porosity affect surface formation and the single and multiple-scattered radiation (Geerken 1991).

2.2 Reflectance properties of pedogenic iron oxides

Iron, when occurring as main constituent of oxides or impurities in minerals (and consequently also in soils and rocks), produces absorption bands in the VIS/NIR due to electronic transition processes of the iron cations (Figure 2.2). The ferrous iron (Fe^{2+}) produces a broad absorption band at 1000 nm, which results from crystal field transition between ^5E_g and $^5T_{2g}$ energy levels in the octahedral crystal field (Hunt et al. 1971). Other

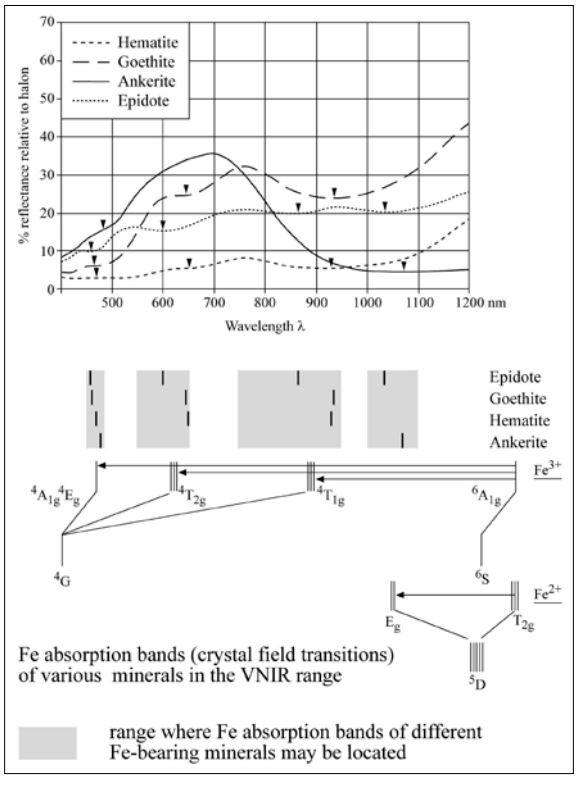

Figure 2.2: Schematic view of the energy levels illustrating the splitting of the ground states (^5D, ^5S) and the first level (^5G) in an octahedral ligand system and their possible electron transitions of Fe^{2+} and Fe^{3+} (modified after Geerken (1991)).

ferrous iron bands are produced by transition from $^5T_{2g}$ to $^5T_{1g}$ at 550 nm, to $^1A_{1g}$ at 510 nm, to $^3T_{2g}$ at 450 nm and to $^3T_{1g}$ at 430 nm. The ferric iron (Fe^{3+}) produces three major absorption bands in the spectrum as a result of transition from $^6A_{1g}$ ground state to energy level $^4T_{1g}$ at ~900 nm and to $^4T_{2g}$ at ~650 nm. The rapid decline of reflectance intensity towards the UV wavelength range is caused by charge transfer bands of iron. The maximum absorption is centered in the UV region but extend into the visible region. This is overlain by less intensive absorption due to crystal field transition of Fe^{3+} from $^6A_{1g}$ to either $^4A_{1g}$ or ^4E_g near 450 nm (Hunt et al. 1971; Hunt and Ashley 1979; Geerken 1991).

Pedogenic iron oxides are formed during the weathering of iron-bearing rocks and minerals (e.g. biotite, pyroxene, amphibole). Trivalent iron oxides are formed under aerobic soil conditions whereas bivalent iron compounds dominate under anaerobic conditions. The trivalent iron oxides occur either uniformly distributed in soils with a great coloring impact or accumulate in form of spots, congregation and entire horizons (Scheffer and Schachtschabel 2002). The most common iron oxides and hydroxides in soils are goethite and hematite. Goethite is present worldwide in most well-drained soils, whereas hematite forms in soils under relative high surface temperature (deserts, subtropics, tropics) (Schwertmann 1988; Birkeland 1999). Due to different crystal structures their absorption bands vary in position (Figure 2.3).

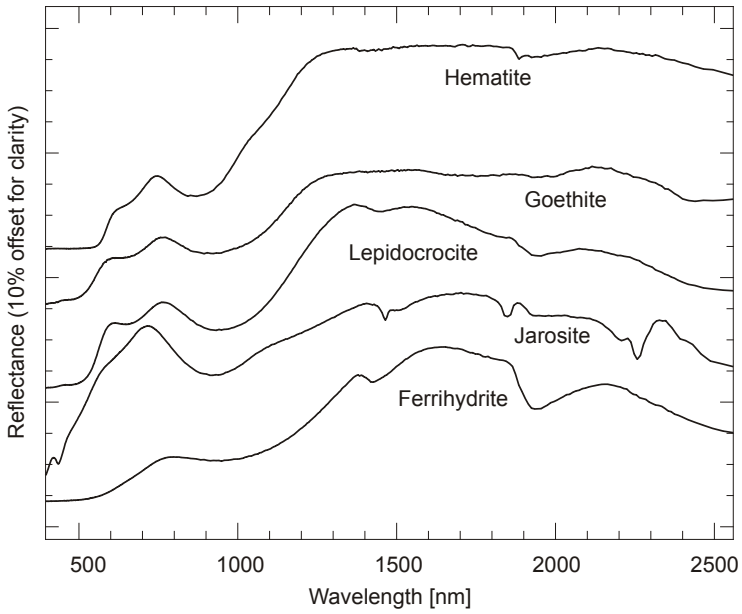

Figure 2.3: Reflectance spectra of different iron oxides (after Clark et al. (1993)).

In hematite (α-Fe_2O_3), the Fe^{3+} is in octahedral coordination with oxygen and shows absorption features at 550 nm (from $^6A_{1g}$ to $^4A_{1g}$), 630 nm (from $^6A_{1g}$ to $^4T_{2g}$) and 860 nm (from $^6A_{1g}$ to $^4T_{1g}$). Goethite (α-FeOOH) has Fe^{3+} in octahedral coordination, but different site distortions along with OH^- and shows absorption features at 480 nm (from $^6A_{1g}$ to $^4A_{1g}$), 650 nm (from $^6A_{1g}$ to $^4T_{2g}$) and 920 nm (from $^6A_{1g}$ to $^4T_{1g}$). The feature near 650 nm usually appears as a shoulder and is most apparent in goethite (Hunt et al. 1971; Morris et al. 1985; Ben-Dor et al. 2002). Neither hematite nor goethite exhibit water and OH^- absorption bands when in their pure forms. An often necessary precursor for the formation of hematite and goethite is ferrihydrite ($5Fe_5HO_8 \cdot 4H_2O$), a water containing iron hydroxide, which forms in groundwater and stagnant water soils (Birkeland 1999). It shows ferric absorption at 1000 nm, weak OH^- absorption near 1400 nm and a characteristic absorption band of molecular water near 1900 nm (Figure 2.3). Lepidocrocite (γ-FeOOH) occurs besides goethite predominately in clay-rich, noncalcareous and anaerobic soils and exhibits ferric absorption at 450, 700 and 980 nm, and only weakly developed OH^- absorption and molecular water absorption. Under very acid soil condition, jarosite ($KFe_3(OH)_6(SO_4)_2$) is formed instead of other ferric iron oxides incorporating the potassium from the feldspar and mica. The ferric absorption bands are located at 430 and 930 nm. OH^- absorption and molecular water absorption are located at 1470 and 1865 nm, and at 2265 nm absorption occurs due to a Fe-OH bend (Clark et al. 1990).

Shifts in the absorption positions are observed due to substitutions Fe^{3+} by other cations (Al^{3+}) and alter the geometry and wavelength of these spectral features (Hunt et al. 1971). However, different iron oxides often occur together and produce a combined absorption band at intermediate wavelength. Ben-Dor et al. (2006) investigated the spectral reflectance characteristics of hematite and goethite mixtures. The VIS absorption band for mixture with equal amounts of both oxides shifts to 510 nm which is located between the original pure mineral absorption. Similar spectral shift occurs for the NIR absorption bands.

2.3 Effects of other soil constituents on soil reflectance

The composition of soils is very complex and their components contribute in various ways to the reflectance spectrum. Beside the iron oxides, clay minerals and carbonates are e.g. the dominant spectrally-active mineral components of soils in the study area. The influence

of the single soil properties on the soil spectral behavior was characterized in detail by different authors (Baumgardner et al. 1985; Ben-Dor et al. 1999). Based on these works, a brief overview of relevant soil properties for this study is given.

2.3.1 Mineral composition

The reflectance spectra of clay minerals are in general dominated by overtone and combination modes of water and OH^- fundamental vibrations. Smectites and kaolinites are the most common clays in soils of the study area. The smectites are a clay mineral group, which spectra are characterized by very strong hydroxyl and molecular water absorption bands at 1400 and 1900 nm and a symmetric hydroxyl band near 2200 nm. This latter feature is very variable depending on the cation the OH^- group is bound to (Figure 2.4). The Al-OH band causes a feature at 2200 nm (e.g. montmorillonite - Al smectite), Fe-OH near 2265 nm (e.g. nontronites - Fe smectite) and Mg-OH near 2300 nm (e.g. hectorites - Mg smectite) (Hunt and Salisbury 1970; Hunt and Ashley 1979; Clark et al. 1990; Ben-Dor et al. 2002). Typical for kaolinites are strong hydroxyl bands centered at 1400 and 2200 nm. The 1900 nm appears only weak due to the lack of appreciable bound water (Hunt and Salisbury 1970). The 2200 nm Al-OH band in kaolinite appears as a diagnostic doublet absorption band (2163 and 2208 nm) and thus allows the differentiation to the smectites (Figure 2.4a). The presence of ferrous and ferric iron in the clay mineral may also produce absorption bands of different strength in the VIS/NIR, for nontronites, they are centered at 450, 660 and 970 nm.

Carbonates, especially calcite and dolomite, are found in soils that formed on carbonatic parent material or allowed the precipitation of secondary soil carbonates. As described above, the seven diagnostic spectral features appear due to overtone and combination modes of CO_3^{2-} fundamental vibrations (Gaffey 1986; Clark 1999). The absorption band occurring between 2300-2350 nm is used for identifying carbonates in soil and due to its intense appearance and location in the measuring range of most hyperspectral instruments. In combination with different cations (Ca^{2+}, Mg^{2+}) its position can vary. In calcite, the band is centered at 2335 nm. With increasing amount of Mg-ions the band center is shifted towards shorter wavelengths. In dolomite the band center is located between 2312-2323 nm (Figure 2.4b). Additional broad absorption bands may appear near 1000 nm indicating the presence of Fe^{2+}. In general, the carbonate absorption bands appear only weak in the soil spectra due to strong overlapping absorption of other soil constituents, such as clay-OH and bond water.

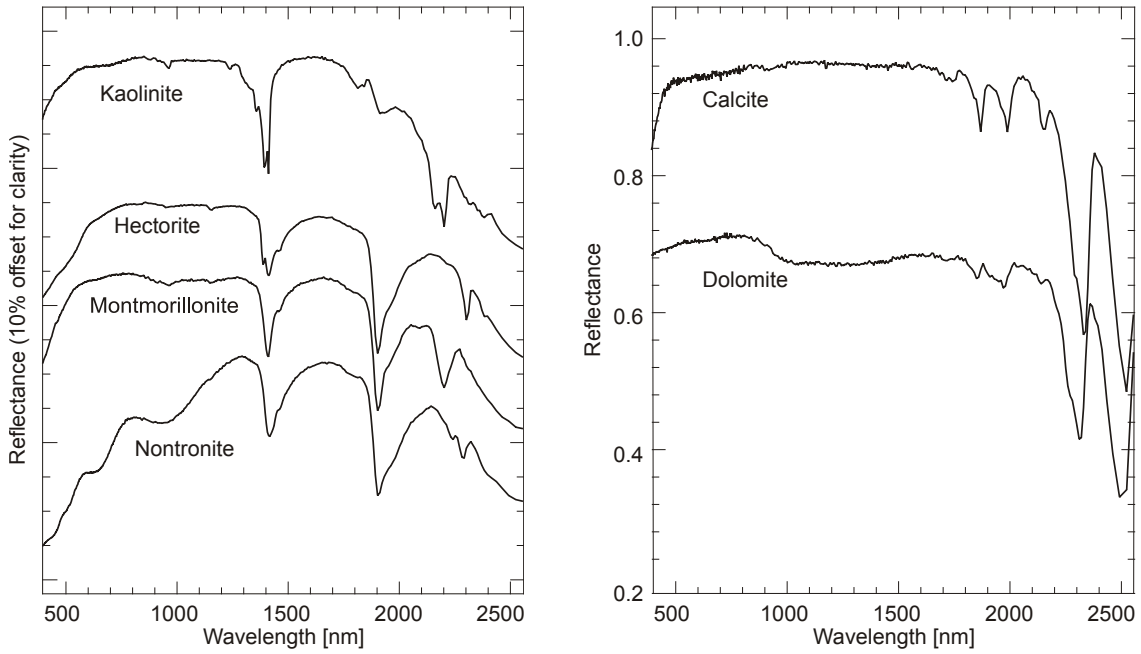

(a) clay mineral spectra

(b) carbonate spectra

Figure 2.4: Bidirectional reflectance spectra of clay minerals and carbonates (after Clark et al. (1993).

2.3.2 Soil organic matter

Soil organic matter and the composition of the organic components have a strong influence on the soil reflectance (Baumgardner et al. 1985; Ben-Dor et al. 2002). When organic matter content exceeds a concentration of 20 g kg^{-1}, it causes reflectance to decrease, particularly in the VIS, and can mask absorption bands of other materials. These masking properties become less effective as the organic matter content drops below 20 g kg^{-1} (Baumgardner et al. 1985; Ben-Dor et al. 2002). The different organic constituents are known to affect the soil reflectance in different degrees as illustrated in Figure 2.5.

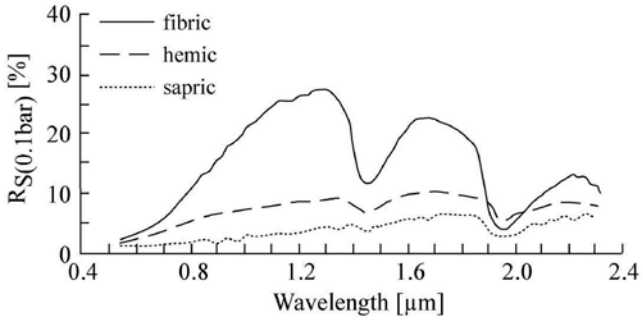

Figure 2.5: Bidirectional reflectance spectra of three soils with different level of decomposition (a) fibric, (b) hemic, and (c) sapric (Baumgardner et al. 1985).

Ben-Dor et al. (1997) investigated the change of the reflectance spectra of organic matter in the VIS/NIR to SWIR regions (400-2500 nm) during a biological decomposition process and revealed that OH^- and C-H_x groups of hygroscopic water, starch, cellulose, and lignin correlate highest with composting time and may be used for estimation of organic matter contents.

2.3.3 Soil moisture

Moist soils have an overall lower reflectance than their dry counterpart in the VIS to SWIR wavelength region; they appear generally darker. With the wetting of the soil, the presence of the absorption bands at 1400 and 1950 nm and occasionally weaker absorptions at 900 and 1200 nm increases and strongly affects the shape of the soil reflectance spectra in the NIR and SWIR. In a recent study, Haubrock et al. (2008) investigated the spectral influence of surface soil moisture contents for sandy soils (Figure 2.6) and estimated successfully the surface soil moisture content from reflectance data based on the new developed Normalized Difference Soil Moisture Index (NSMI) that combines the reflectance values at 1800 and 2119 nm.

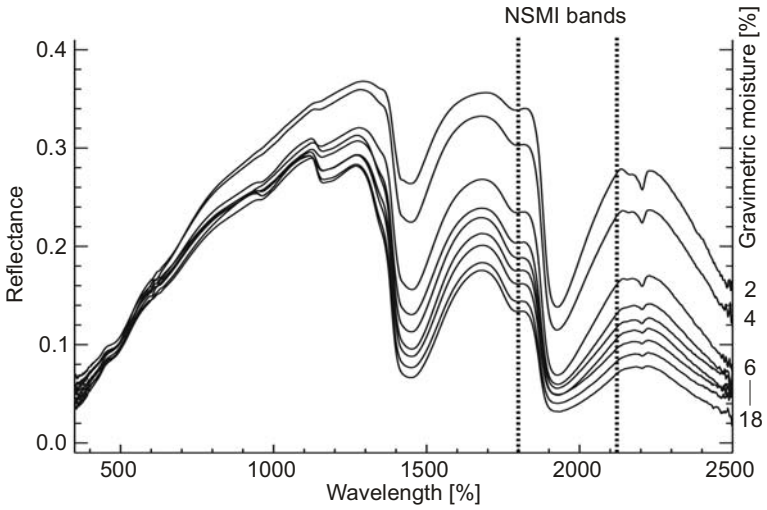

Figure 2.6: Laboratory spectra of soil samples (quaternary sand) with different moisture percentages. With increasing soil moisture the water absorption bands at 1400 and 1900 nm become deeper and wider, finally masking the 2200 nm OH^- absorption (modified after Haubrock et al. (2008)).

2.4 Natural parameters affecting soil reflectance

2.4.1 Soil texture and surface roughness

The soil reflectance is not only characterized by its mineral and organic components but also by soil particle and aggregate sizes. These soil physical properties mainly influence the spectra's albedo, which is the relative area under the reflectance curve. They often dominate over the chemical properties (Ben-Dor et al. 2003).

In general, the increase in particle or aggregate size causes a decreasing overall reflectance and increasing absorption band depth in the spectrum (Baumgardner et al. 1985; van der Meer 1995), so fine-grained soils have a higher reflectance as coarse-grained soils. This behavior is characteristic for transparent materials such as most silicates in the SWIR (Salisbury and Hunt 1968). Opaque materials will show the opposite behavior where reflectance decreases with decreasing particle size. Iron oxides show a transopaque behavior, which is related to the high absorption coefficients in the visible wavelength region. This behavior is evident for grain size decrease where the albedo increases for wavelength greater than 550 nm (transparent) but decreases for wavelength less than 550 nm (opaque) (Hunt et al. 1971).

Gaffey (1986) studied the effects of particle size (between < 38 µm and 0.5 mm) on the spectral properties of calcite and found that only the samples albedo and absolute band depth varying with the particle size, while the number of spectral features, their form and position, and relative band intensities (ratio of a given absorption band to other bands in the same spectrum) remain unaffected. A study from Orlov (1966) showed that the reflectance of aggregates with a diameter of 0.25-10 mm changed only little, while the fraction below 0.25 mm showed a significant increase of reflectance. Figure 2.7 depicts reflectance spectra of different sandy soils which illustrate the above described behavior.

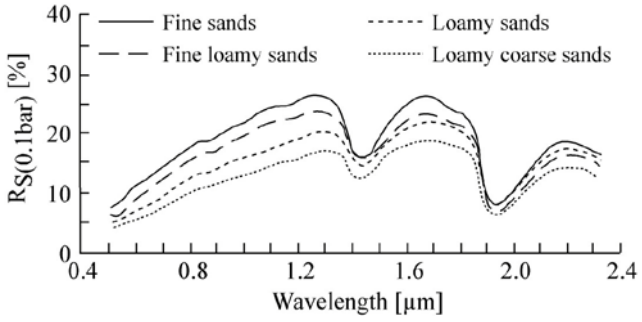

Figure 2.7: Reflectance spectra of soils with different predominate particle size (Baumgardner et al. 1985).

In natural environment, the spectral influence of the soil's particle size may be covered by the aggregation of the soil. So despite having a finer particle size distribution, clayey soils often appear darker than sandy soils because they tend to aggregate more and behave as larger, ''rougher'' surfaces. It is also know that the soil aggregate size is strongly related to the absolute iron oxide content (Stoner and Baumgardner 1981; Ben-Dor and Singer 1987). With increasing iron oxides content also the size of the soil aggregates increases because of the cementation effects of the free iron oxides.

The aggregate size of a soil surface may change over a short period of time due to tillage, soil erosion or physical crust formation. Physical crust also termed structural crust is a thin layer on the soil surface which can form within minutes during a rainfall event (Ben-Dor et al. 2003). The raindrop energy causes a destruction of soil aggregate and rearrangement of texture and clay minerals within the upper soil surface. This has a great effect on other soil physical properties, such as infiltration and runoff, and cause an increase of the soil erosion vulnerability (Ben-Dor et al. 2003; Malley et al. 2004). In a study on Israel soils Goldshleger et al. (2004) found the reflectance spectra changing dramatically in the NIR-SWIR when crust is formed. With increasing amount of rain, the albedo increases and clay spectral signatures are enhanced due to greater clay fraction in the crust. The formation of surface crusts is common on Mediterranean soils and has been described for carbonate, gypsum and salt-dominated soils in SE Spain (Margate and Shrestha 2001).

2.4.2 Vegetation coverage

In most parts of the world, soils are overgrown by vegetation. The reflectance spectra of vegetation characterize distinct absorption properties for green, photosynthetic active (PV) and dry non-photosynthetic (NPV) vegetation, respectively (Figure 2.8). In between the two pure types a continuous range of intermediate stages with joint spectral properties can be found.

The spectrum of green, photosynthetic active vegetation (PV) is dominated by strong absorptions of leaf pigments between 400 to 700 nm due to electron transition processes (Figure 2.8). The chlorophyll pigments a and b absorb incident light centered at 430 to 450 nm and 650 to 660 nm for the photosynthesis. The red edge characterizes the rapid increase of reflectance from the VIS to the NIR plateau, which is an important indicator of the vegetation vitality. From 700 to 2500 nm absorption of plant water content causes absorption maxima at 970, 1170, 1480, and 1940 nm. The plant water positions are slightly

shifted towards shorter wavelengths than for liquid water bands due to hydrogen bonding (Curran 1989; Elvidge 1990).

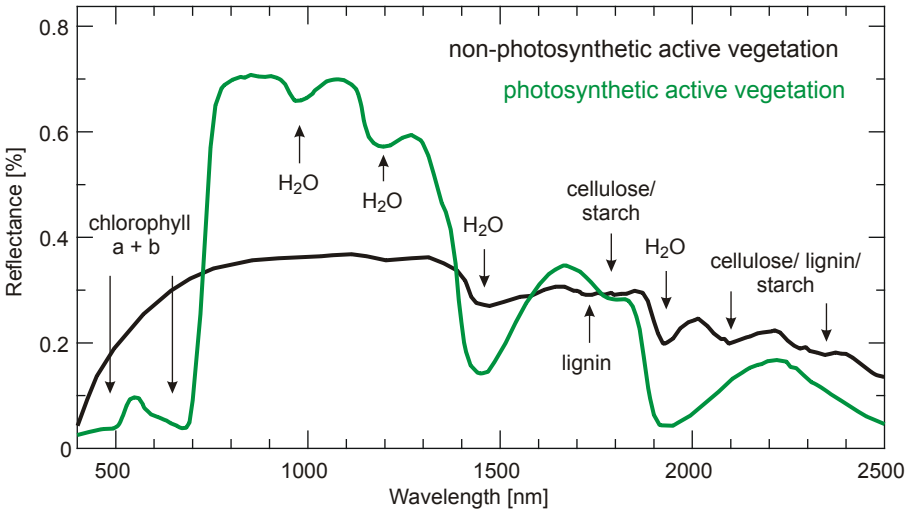

Figure 2.8: Reflectance spectra of photosynthetic and non-photosynthetic active vegetation (own measurements).

The spectrum of dry, non-photosynthetic active vegetation (NPV) lacks chlorophyll and intense water absorptions (Figure 2.8). Lignin, cellulose and starch spectral features dominate the spectrum beyond 1000 nm, which are not present in the most green vegetation spectra due to covering effect of strong water absorption. The characteristic spectral features are combination and overtone modes of fundamental C-H and OH^- stretching and deformation modes. At 1720 nm (C-H stretching overtone) a spectral features appears that is generated by lignin in interaction with other plant constituents (e.g. wax). Just next to it, a cellulose induced absorption band appears at 1780 nm (C-H stretching overtone and OH^- stretching). From 2050 to 2150 nm (OH^- and C-H deformation modes + OH^- stretching) a broad absorption region of lignin, cellulose and starch (if present) dominates the dry vegetation spectrum. Cellulose shows another strong absorption feature at 2340 nm (OH^- and C-H deformation modes + OH^- stretching) (Curran 1989; Elvidge 1990), that is also detected in soils with very high organic matter content or in lignite material (Krüger et al. 1998). Beside these features, high resolution, spectroscopic measurements of dried vegetation revealed about 42 minor absorption features, but most of them are usually not resolved by the spectral resolution and spectral sampling interval of the hyperspectral instruments (Curran 1989; Elvidge 1990).

Chapter 3: **Study area**

The study area is located in the Cabo de Gata-Níjar Natural Park in the Andalucían Province Almeria in Southeastern Spain at 36.5° North and 2.05° West (Figure 3.1). The 1987 created Natural Park covers 38000 ha of land with volcanic mountain range, dunes coastal formation, salt mines, cliffs and 12000 ha of marine coastline with marine prairies of fanerogamas. It is one of a few protected semi-desert and steppe regions in Europe. A high variety of endemic species of flora and fauna has adapted to the extreme climate conditions, which lead to the declaration of the park as World Reserve of the biosphere by the UNESCO in 1997. This restricted the land use to sustainable and non-irrigated agriculture in the valleys and grazing on the slopes.

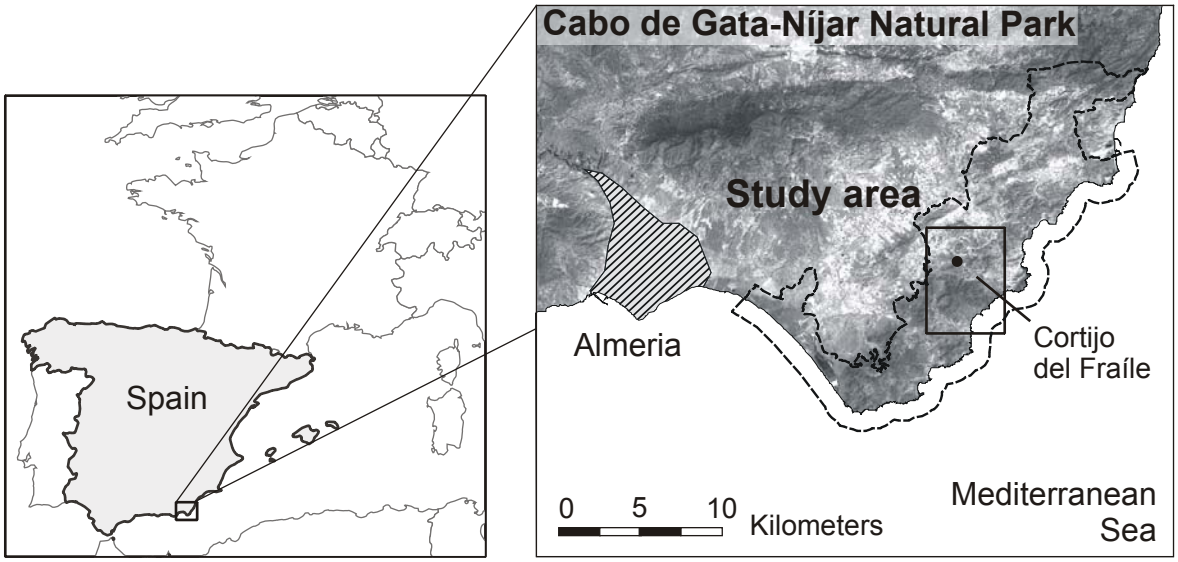

Figure 3.1: Location of study area.

3.1 Landscape evolution

The Cabo de Gata area is a Miocene volcanic province in the Betic Cordillera, the westernmost segment of the European Alpine orogenic belt. The 10 km wide and 40 km long Cabo de Gata volcanic chain is the most extensive volcanic area in the Betic Cordillera and separated from the main part by the NE-SW trending Carboneras strike-slip fault system (Weijermars 1991). The volcanic activity took place in two main phases between 14 Ma and 7.5 Ma mainly as near or sub-surface activity. Both phases are separated and followed by periods of marine sedimentation (Weijermars 1991; Martín et al. 2003).

The oldest volcanic rocks, found in the southern part of the park, were extruded from 14 and 10 Ma and constitute a typical calc-alkaline series from basaltic, amphibole and pyroxene andesites, dacites to rhyolites. The volcanic rocks occur as dome complexes (no.4 in Figure 3.2) with significant associated pyroclastic-flow deposits (ignimbrites in Figure 3.2) (Fernández-Soler 2001; Martín et al. 2003). Noteworthy in this context are the formation of hydrothermal gold-alunite deposits in the Rodalquilar area and numerous bentonite deposits in the greater area that have been commercially exploited until the mid of last century (Rytuba et al. 1990; Caballero et al. 1991). During early Tortonian, the igneous materials were locally overlain by bioclastic carbonates (no.9 in Figure 3.2) that deposited in coastal palaeoenvironments flanking the emergent topography of the volcanic strata (Fernández-Soler 2001; Martín et al. 2003). The second of volcanic activity took place between 8.7 and 7.5 Ma during late Tortonian and is mostly found in the northern part of the park. This volcanism was similar in composition and type of emplacement to the first phase. Dacites and andesites with common pyroclastic breccias and partly with high amounts of Fe-bearing minerals (e.g., hornblende, biotite) are the main volcanic lithologies (Fernández-Soler 2001).

In the Messinian followed numerous sedimentation phases with bioclastic calcarenites, silty marls, carbonates, sandstones and conglomerates, and completed the Neogene fill of the marine basins (Martín et al. 2003). The continuous tectonic uplift of the Cabo de Gata area along the Carboneras fault has caused that marine sediments in the northern part of the study area can sometimes be found at almost 300 m above sea level (Martín et al. 2003).

During the Quaternary, extensive glacis of carbonates and fine-grained materials, and alluvial and colluvial fans of volcanic breccias have been formed descending from the Cabo de Gata volcanic mountains (no.10 in Figure 3.2). These are especially pronounced

in the southern Cabo de Gata region with the maximum altitudes of the mountain chain El Fraile (493 m) and Cerro Peñones (488 m). The present-day coastline is steep and cuts directly through the volcanic strata and the alluvial fans. In the southern park, sedimentary materials (alluvial clays, silts and sands) are locally overlying the volcanic reliefs and produce mesa-like landforms, e.g. Cortijo del Fraile (Martín et al. 2003). The northernmost regions in the park are low areas surrounded by small volcanic hills, which are generally covered by the Carboneras sub-basin deposits. The rocks in this sub-basin dip gently towards the coast, and are deeply dissected by the modern ephemeral drainage network. The coastline in this area describes a long, narrow beach lying at the foot of small cliffs (Martín et al. 2003).

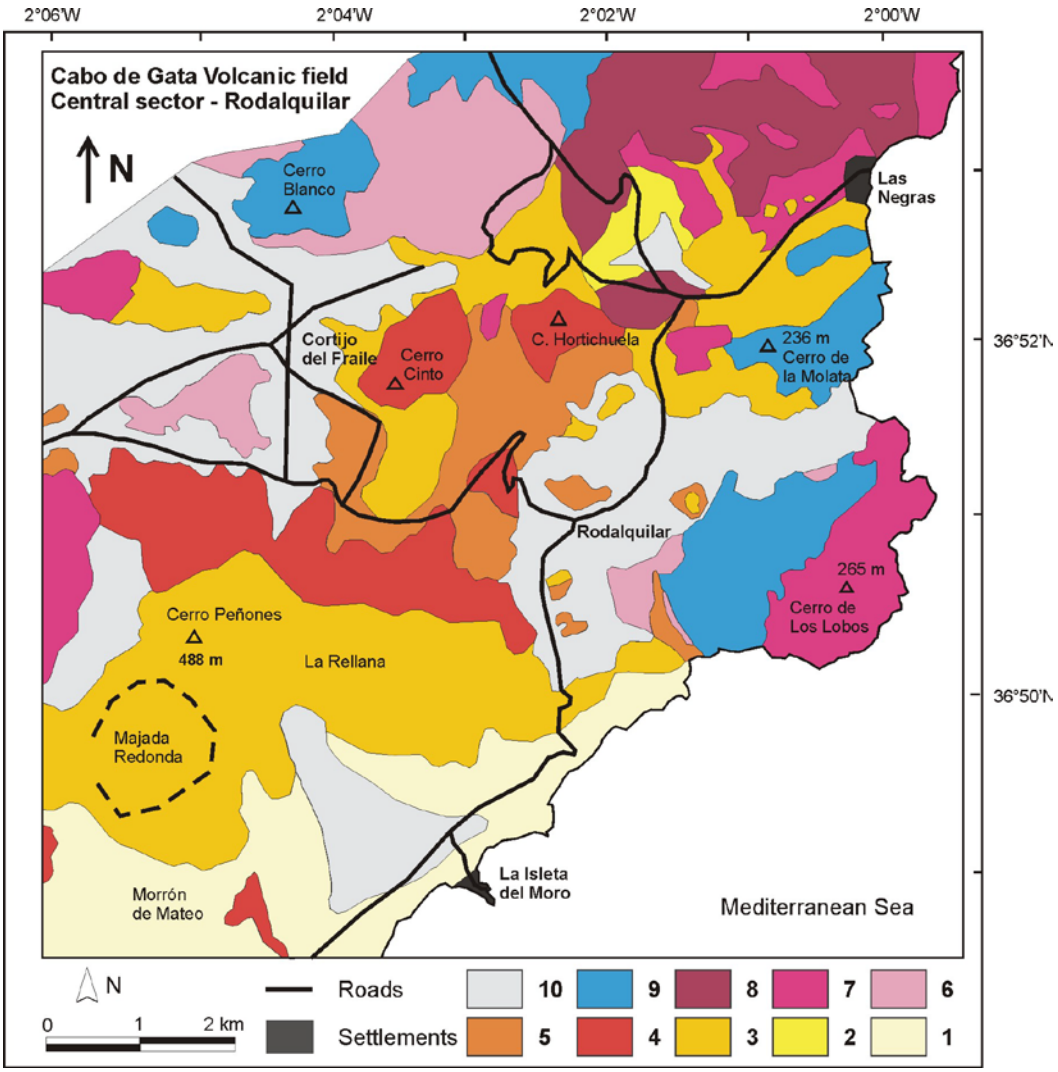

Figure 3.2: Geological map of Rodalquilar area (1. Pre-caldera rocks (Frailes zone); 2. Pre-caldera rhyolite ignimbrites (Hortichuelas); 3. Cinto ignimbrite; 4. Lava domes; 5. Lazaras ignimbrite; 6. Hornblende andesites; 7. Pyroxene andesites; 8. Amphibole dacites; 9. Calcarenites; 10. Quaternary deposits) (modified after Fernández-Soler (2001)).

3.2 Climate

The climate in the study area is Mediterranean semi-arid with long hot summers and mild winters. The mean annual temperature is about 18°C with narrow thermic oscillations as a consequence of sea influence. The maximum temperatures of the warmest month rarely exceed 36°C, while the minimum of the coldest month seldom drops below 5°C. The mean annual precipitation is less than 200 mm and irregularly distributed throughout the year, which makes the region one of the driest in Western Europe. In July and August, there is practically a total absence of rainfall, while during the October-March period it has frequently torrential character with sometimes more than 50 % of the total annual precipitation falling within a single day (Peinado et al. 1992; Paruelo et al. 2005). The general aridity of the area is intensified by high wind frequency and intensity. The potential evapotranspiration of over 900 mm per year causes a high water deficit, which is balanced by a high relative humidity of often more than 75 % and humid southwesterly blowing sea winds (Peinado et al. 1992). The climate diagram of the Almería station near the western border of the Natural Park is shown in Figure 3.3 for year 2005. Three days with low precipitation rate (between 0.4 and 1.2 mm) were registered in July and August during that year.

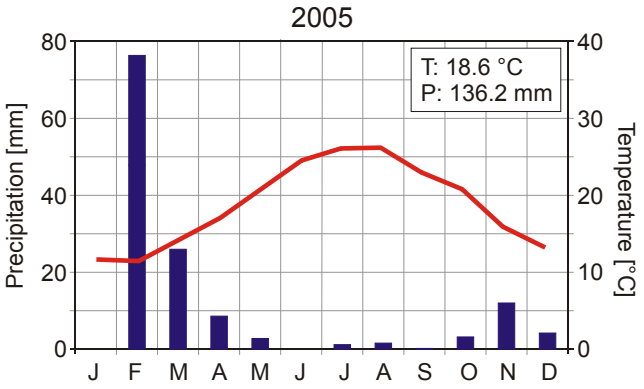

Figure 3.3: Climate diagram from Almería station for the year 2005 (Junta de Andalucía 2006).

3.3 Soils

The study area is characterized by high soil diversity with complex spatial pattern of soil properties, such as texture, iron oxides and carbonates that originate from the high variety of geological substrates, diversity of relief and alternating climatic regimes (Oyonarte 2004 pers. communication in: Bachmann (2007). The description of the soils is based on the area-wide soil mapping in 1:100.000 scale that was done in the frame of the 'LUCDEME'

project (Aguilar et al. 1989; Aguilar et al. 1990). The FAO World Reference Base of Soil Resources is used for soil type characterization (FAO 2005).

On the summits and the steep upper slopes of the Sierra de Cabo de Gata mountains, Regosols and Leptosols have developed as dominating soil types on the volcanic and carbonate bedrock (Figure 3.4, light-blue). On unconsolidated and often highly alterated parent materials, very weakly developed mineral soils occur as Calcaric and Eutric Regosols. Eutric Leptosols developed predominately at the steep slopes which often show an extremely high stone or gravel content due to the continuous material erosion. The eroded material accumulates as fine-grained sediments (sand, silt, clay) in the valleys and gentle lower slopes, where soil development is less disturbed. Here more developed Calcisols (depicted orange in Figure 3.4), Luvisols (red) and Cambisols (pink) are found.

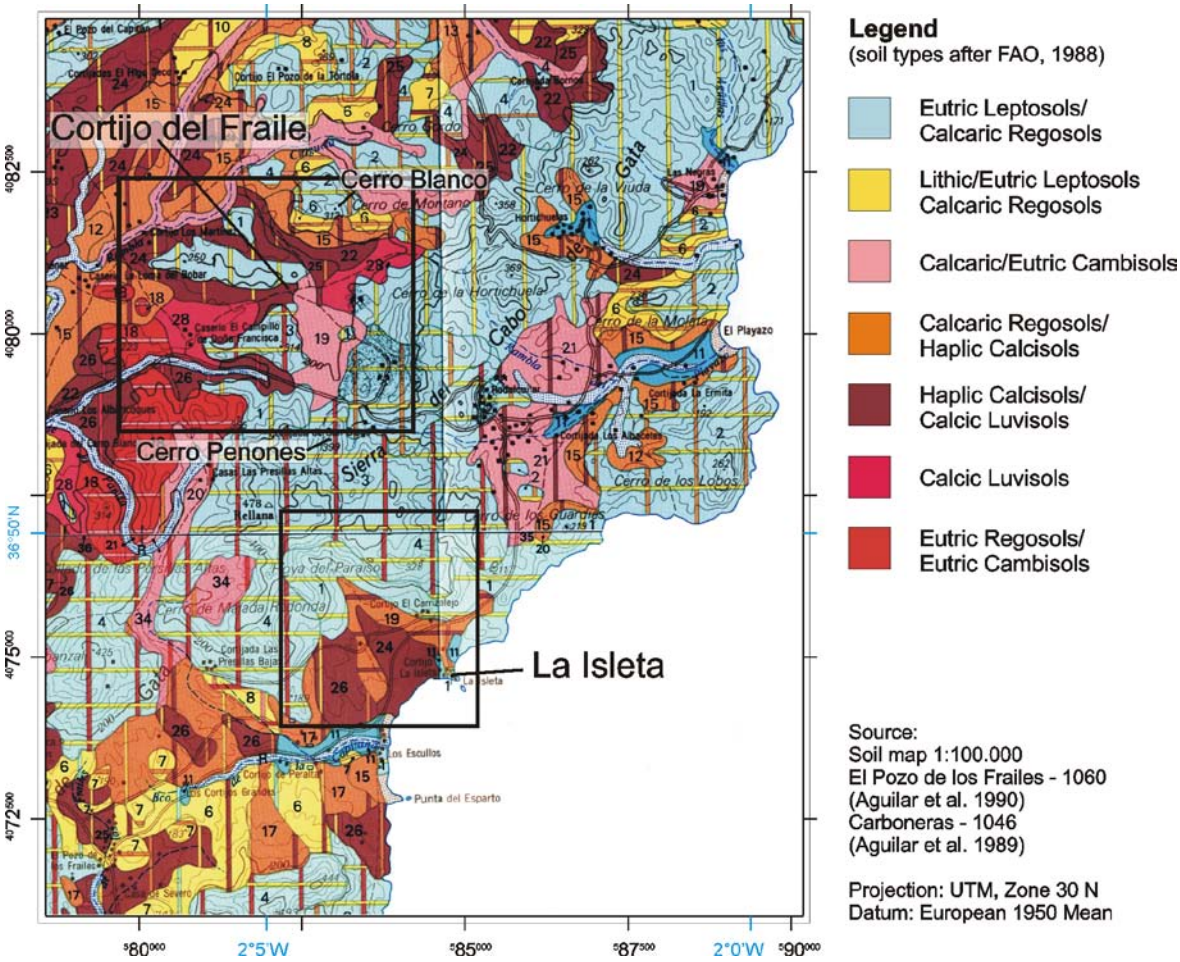

Figure 3.4: Soil type map of the study area (mosaic from Aguilar et al. (1989) and Aguilar et al. (1990)).

Calcisols are soils with a substantial secondary accumulation of lime that are common in highly calcareous parent materials and widespread in arid and semi-arid environments. Luvisols summarize more developed soils with higher clay content in the subsoil (Argic subsoil horizon) than in the topsoil as a result of pedogenic processes (e.g. clay migration). High-activity clays occur throughout the Argic horizon and certain depths show a high base saturation. Cambisols show at least an incipient subsurface soil formation, e.g. from mostly brownish discoloration and increasing clay percentage and/or carbonate removal (FAO 2005).

The soils on volcanic substrata are intensely reddish brown in color (2.5YR - 5YR Munsell hues), attributed to high hematite contents. The shallow soils on the limestones are light grayish yellow (10YR - 2.5Y Munsell hues), reflecting very little iron oxide contribution to the soil coloring. This indicates low soil development because the characteristic intense red soil colors gradually induced by rubification processes are not observed (Ben-Dor et al. 2006).

The soil development takes place under aridic soil moisture and thermic soil temperature regimes and is influenced by the stability of the parent material and the slope gradient. The base saturation is good for soils on carbonatic bedrock and some soils on volcanic bedrock in the southern part of the study area, where pedogenic carbonates have accumulated at plant roots. Here, Ca-bearing minerals such as plagioclase, hornblende and pyroxene representing the calc-alkaline character of the Cabo de Gata volcanism are the main Ca-source of the volcanic rocks (Cunningham et al. 1990; Caballero et al. 1991). Suitable conditions for an active microbial development and humus recycling of the soils in the study area were described by Aranda and Oyonarte (2005). This is also reflected in the low content of fresh organic material on the soil surface and upper soil layers. The observed lichens and biogenic soil crusts on the less-vegetated areas play an important role for the soil stability (Karnieli et al. 1996; Ben-Dor et al. 2003). In the following, the soils of two exemplary regions indicated in Figure 3.4 are characterized in more detail. The first region comprises Cortijo del Fraile and the adjacent valleys which are partly under cultivation. The second region covers the large alluvial fan near La Isleta.

Cortijo del Fraile is located at the transition between carbonatic and volcanic bedrock. The north-eastern part is dominated by the Cerro Blanco which is formed of biogenic calcarenites. On the summit and backslopes shallow carbonate-rich Lithic Leptosols have developed. At the footslope Eutric Leptosols formed on the fine-grained material that

deposited since the Pleistocene. The soils that developed on the adjoining alluvial plains are moderately developed Petric Calcisols. Further south they merge into Calcic Luvisols due to increased input of fine-grained materials from the volcanic mountains. A sharp transition from grayish yellow to reddish brown soil colors occurs at the lowest point of the valley because of the high iron oxide contents of the volcanic sediments (Figure 3.5). Comparable soil color change also occurs in the valley west of Cortijo del Fraile. But there the northern mountain range lacks the iron-rich mineralogy which is dominating in the southern volcanic mountains. The soils that developed on fine-grained sediments in this valley are grayish Haplic Calcisols with inclusions of Eutric Leptosols and Calcaric Regosols that merge into reddish Calcic Luvisols. In southwestern continuation of the valley Eutric Regosols and Cambisols have developed. The valley south of Cortijo del Fraile is surrounded by volcanic mountains with iron-rich mineralogy. Reddish Calcaric Cambisols have formed on alluvial and colluvial sediments. The northern slopes of Cerro Peñones define the southern boundary of this region. Shallow and weakly developed Eutric Regosols and Lithic Leptosols have formed on the red-violet biotitic dacites and andesites.

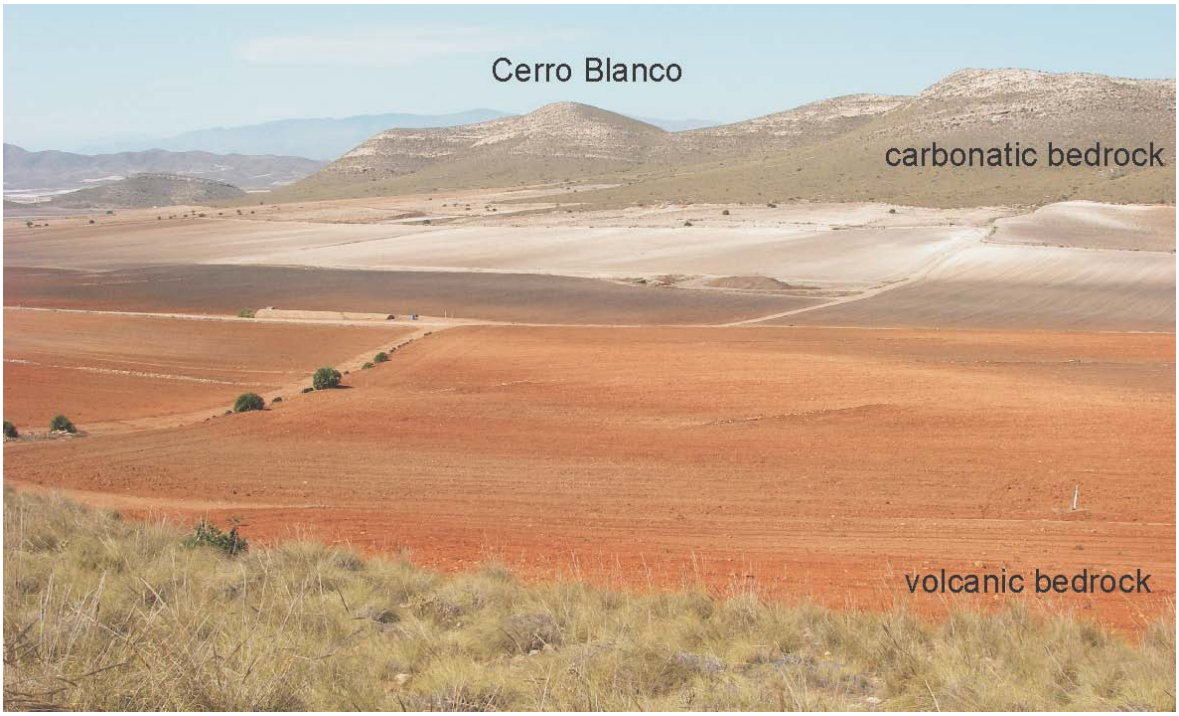

Figure 3.5: Transition from reddish volcanic to grayish-white carbonatic soils due to change of geological parent material (Oct. 2006, northwards view).

Near the village La Isleta and south of the Cerro Peñones lies the valley Hoya del Paraiso followed by the large Quaternary alluvial fan that extends to the coast. The upper slopes of the mountains are characterized by reddish-violet biotite-amphibole dacites and pyroxene andesites from an earlier eruption, which are the source material for the development of alluvial and colluvial glacis and fans. On the Pleistocene glacis fans in the upper valley, Eutric Regosols and Lithic Leptosols have formed. The soils of subsequent Quaternary alluvial fans are mapped as Eutric Leptosols and Petric/Haplic Calcisols. In a detailed study, Harvey et al. (1999) distinguished three age-related groups of fan sediments (Qf1, Qf3, Qf5) with different degree of soil development (Figure 3.6) which were generalized in the soil map as Haplic Calcisols and Calcic Luvisols. The Qf1 surfaces show the most mature soil profile development with red (2.5 - 5YR Munsell hues) and clay-translocated Bw horizon overlaying a BCk horizon (Figure 3.7) with high pedogenic carbonate content and massive indurated pedogenic calcretes (Calcic Luvisol). Soils on Qf3 surfaces are generally less mature in their development, showing a less red B horizon (5 - 7.5YR hues) and pedogenic carbonate content (Petric Calcisol). Pedogenic calcretes on the Qf3 surfaces are much weaker developed than on Qf1. The soils of Qf5 surfaces are only weakly developed with similar soil colors as the parent material (7.5YR hues) and little to no carbonate accumulation.

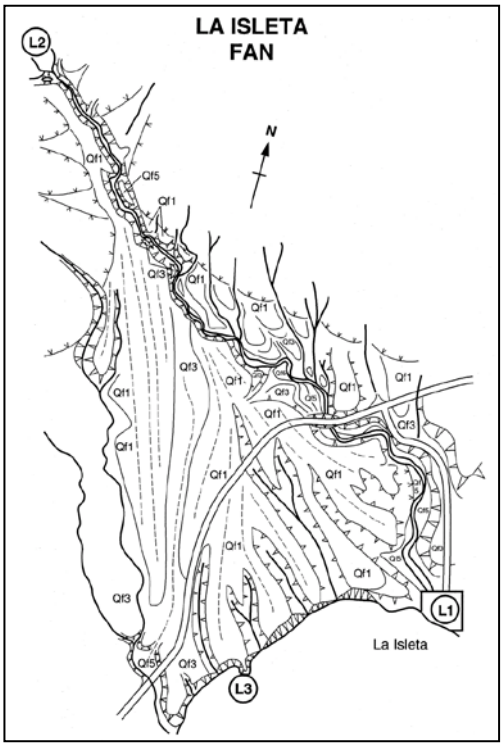

Figure 3.6: Quaternary alluvial fan near La Isleta (Harvey et al. 1999).

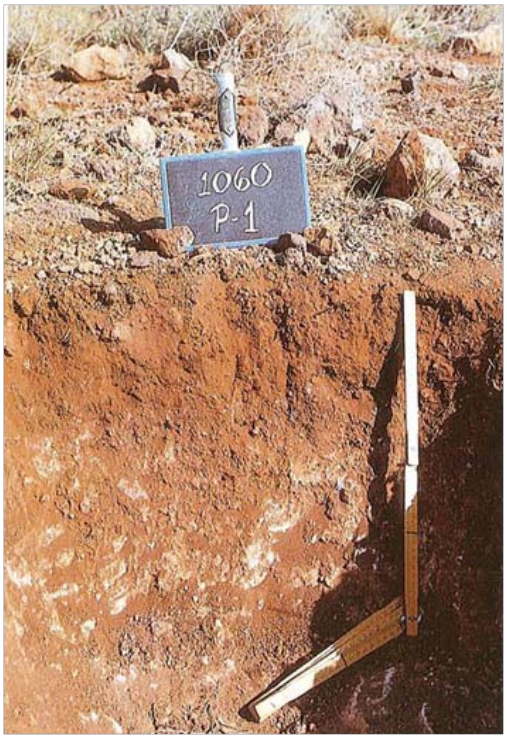

Figure 3.7: Profile of Calcic Luvisol at the Qf1 surface of the La Isleta alluvial fan (Aguilar et al. 1990).

3.4 Vegetation and land use

The Cabo de Gata area belongs to the murciano-almeriense botanical province, which is due to the thermomediterranean semi-arid character the most xeric and arid region of the Iberic Peninsula (Aranda and Oyonarte 2005). The dominant species of the steppe-like vegetation are tussock grass (*Stipa tenacissima*), small bushes (*Ziziphus lotus*, *Periploca laevigata*) and dwarf-palms (*Chamaerops humilis*), the only indigenous palm in Europe. Together with frequent areas of open soil or rubble, these vegetation patches form a small-scaled mosaic. Denser vegetation indicates areas with undisturbed soil formation or a more humid microclimate. Larger areas of bare soils indicate degradation processes, which originate mostly from intensive grazing or change of land use (Alados et al. 2004a). Woodland-type vegetation does not occur in the park because of the low precipitation rate and the dominance of Regosols. Aranda and Oyonarte (2005) distinguished three general types of Mediterranean semi-arid vegetation that can be found in Cabo de Gata:

I Developed matorral with a variety of evolved shrubs, small bushes and tussock grass:
  - I.1 Lentiscal (mainly *Chamaerops humilis*, *Rhamnus lycioides* and *Pistacia lentiscus*)
  - I.2 Cornical (mainly *Periploca angustifolia*, *Maytenus europaeus* and *Chamaerops humilis*)
  - I.3 Espartal (only *Stipa tenacissima*)

II Degraded matorral with small bushes, grass and herb-like plants:
  - II.1 Aulagar (mainly *Ulex parviflorus* and *Rosmarinus officinalis*)
  - II.2 Tomillar (*Thymus sp.* and *Helianthemun sp.*)
  - II.3 Albaidal (*Anthylis cytisoides*)

III Azufaifal, specific typology on consolidated sand dunes (soils with very low pedogenic development), mainly *Ziziphus lotus*, *Withania frutescens* and *Rhamnus lycioides.*

The Cornical vegetation (I.2) represents the climax-community developing on the slopes that are well exposed to the sea to receive humid sea winds. Inland, where the aridity and continental influence is higher, the Lentiscal vegetation type (I.1) with *Chamaerops* replaces the Cornical (Peinado et al. 1992). The Espartal (I.3) and degraded matorral (II) also characterize different stages of vegetation successional regression or recovery, respectively.

Stipa-dominated developed matorral and Espartal communities cover the middle and upper mountain slopes and plateaus in the Natural Park (Figure 3.8). They are often mixed with opuntia (*Opuntia ficus indica*) and dwarf-palms. Rock outcrops with lichen cover appear on the steep slopes. These regions are used for livestock grazing (mainly goats and sheep)

because steep terrain and the shallow and weak developed soils limit agricultural land use. The grazing-tolerant *Stipa* cover was found to be a good indicator for an increasing grazing pressure (Alados et al. 2003; Navarro et al. 2006). However, grazing activity does not exceed the estimated carrying capacity, so continuous vegetation regression cannot be observed (Alados et al. 2004a).

(a) Cornical formation: *Chamaerops humilis* on the east slope of valley Hoya del Paraiso

(b) Espartal formation: *Stipa tenacissima* on the north slope of Cerro Blanco

Figure 3.8: Overview of main plant species in the study area (July 2005).

The flat valleys and lower slopes with their well developed and profound soils have traditionally been used for crop cultivation. With the establishment of the Natural Park, the continuous intensification (e.g. irrigation) of agriculture was restricted within the park but dominates its surroundings. Today, dryland agriculture of cereals with low yields and olive trees as the main crops are found (Figure 3.9). An exception is the area around Cortijo del Fraile, where ecologically irrigated agriculture is allowed. Large formerly cultivated areas are currently abandoned and in different stages of vegetation succession, ranging from short grass, e.g. *Brachypodium retusum*, to Tomillar communities (Oyonarte et al. 2007). In some areas park authorities had started renaturation of abandoned cultivated areas with native plants, e.g. near the village La Isleta del Moro where most areas of the alluvial fan

are currently renaturated with *ziziphus* plantation (Figure 3.10). The transition between the abandoned cultivated area with Tomillar communities to Espartal and other matorral communities is in many places still clearly visible although *Stipa* and *Chamaerops* have begun to colonize these areas (see Figure 3.11). The matorral vegetation dominates the areas where steep gradients and weakly developed mineral soils with high stone or gravel content limited agricultural use.

Figure 3.9: Overview of agricultural region in Cortijo del Fraile, in the foreground Tomillar vegetation with immigrated *Chamaerops* (Oct. 2006, eastward view).

The land use of the Natural Park has undergone important changes since the late 1950s. A recent study on land cover changes in Cabo de Gata between 1957 and 1994 has identified two main processes (Alados et al. 2004b). The first process comprises the period of large-scale land abandonment since the 1960s which caused a reduction of croplands by 45 % until 1994 (Alados et al. 2003) and subsequent increase of areas with arid garrigues cover (Tomillar communities and short grass). The second phase is characterized by an evolution towards tussock grass steppes, Espartal, (+19 % from 1957 to 94) as a result of vegetation successional dynamics (from garrigue to steppe) and vegetation successional regression (from developed matorral to steppe) caused by human and grazing pressure (Alados et al. 2003; Alados et al. 2004b). The dense matorral showed only a small net increase, especially after the area was declared as Natural Park in 1987.

Figure 3.10: Renaturation of abandoned cultivated areas: *Ziziphus* plantation near the village La Isleta del Moro (June 2007, southwards view).

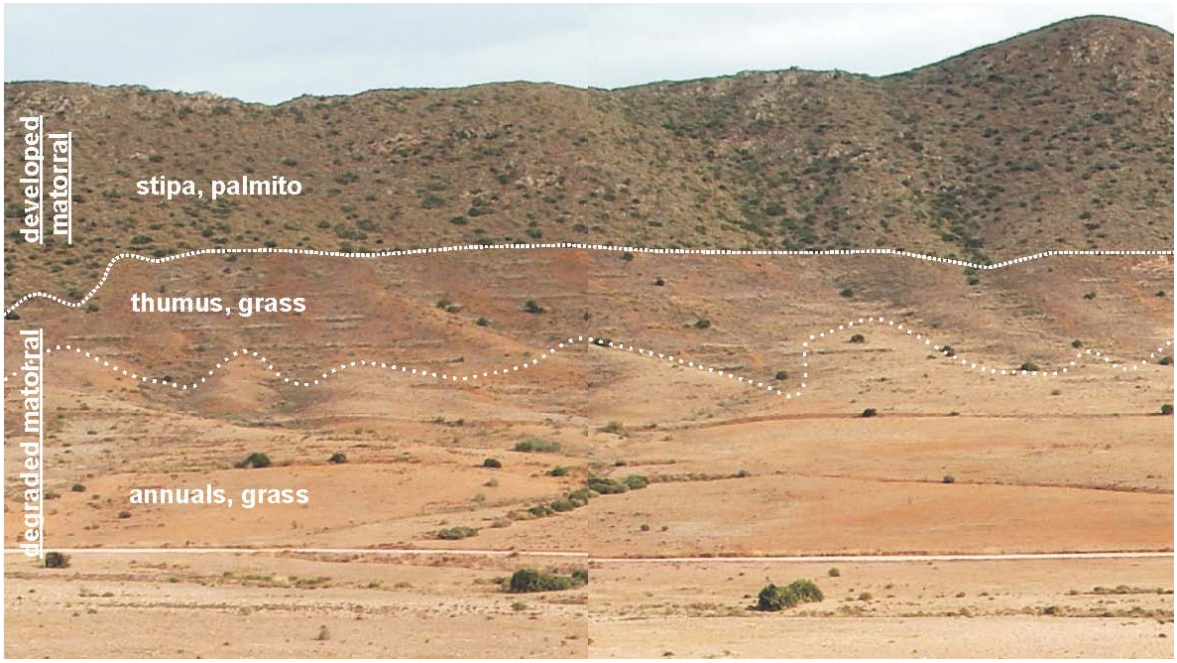

Figure 3.11: Typical series of vegetation types along a slope after abandonment of cultivation and beginning vegetation succession (Oct. 2006, southwards view).

Chapter 4: **Materials and methods**

4.1 Soil sampling and chemical analysis

Soil samples were taken from all main soil types in the study area with the aim to represent the entirety of pedogenic iron oxides concentrations on the soil surface. In total 50 soil samples were collected in an area of approximately 6200 ha. The soil sampling elevation ranges between 41 and 398 m, with an average elevation of 188 m. The majority of samples were taken around Cortijo del Fraile where pedogenic iron oxide content is highly variable due to the transition from different volcanic to carbonatic lithologies.

The soil samples originating from shallow Calcaric Regosols and Petric Calcisols over limestones contain only very little iron oxide indicated by light grayish yellow soil colors (10YR - 2.5Y Munsell hues). Most samples were taken of more developed soils over alluvial and colluvial sediments originating from the volcanic mountains, where iron-rich minerals of the bedrock, such as biotite and amphiboles are the main iron source. Intensive reddish brown to brown soil colors (2.5YR - 7.5YR Munsell hues) characterize these soils, which are Eutric/Calcaric Cambisols, Calcic Luvisols and Petric Calcisols that formed in the transition to the carbonate-dominated soil.

26 soil samples were collected from cultivated areas, 22 from areas with abandoned cultivation and two with matorral vegetation cover (Table 4.1). From the cultivated area 19 samples originate from iron oxide-rich soils on alluvial sediments with volcanic origin (andesites, dacites, pyroclastic breccias) and seven samples from iron oxide-poor soils on sediments originating from calcarenites and carbonates. From areas with abandoned crop cultivation, 15 samples were collected from volcanic and one from carbonatic substratum around Cortijo del Fraile. Additional six samples were taken from Eutric Regosols and Petric Calcisols over biotite dacites and volcanic-originating sediments near the villages Rodalquilar and La Isleta del Moro. On the upper slopes with matorral vegetation cover,

two samples were collected from Eutric Leptosols and Regosols, one sample over calcarenites and one over biotite-/pyroxene-rich andesites and dacites.

Table 4.1: Summary of soil samples classified by parent material and land use, respectively.

total of 50 soil samples collected	
parent material (soil type)	**land use (vegetation cover)**
• 40 samples from soils over volcanic sediments (Eutric/Calcaric Cambisols, Calcic Luvisols and Petric Calcisols) • 8 samples from soils over carbonatic sediments (Calcaric Regosols and Petric Calcisols) • 2 samples, one each from soils of volcanic and carbonatic bedrock (Eutric Leptosols and Regosols)	• 26 samples from cultivated sites (no permanent vegetation cover) • 22 samples from abandoned cultivated sites (partly vegetation cover) • 2 samples from sites with developed matorral (dense vegetation cover)

All soil samples were taken from the upper soil surface (0-2 cm) because only those materials affect the reflectance signal when recorded with a field spectrometer or airborne hyperspectral sensor and can subsequently be used for analyzing the spatial Fe_d distribution (Ben-Dor 2002). Each sample was composed of four to six sub-samples which were taken in an area of 1 x 1 m. The individual sampling points were surveyed with a handheld GPS and characterized in detail regarding their landform and topography, parent material, vegetation cover and land use.

Soil chemical analysis

Soil chemical properties and particle size distribution were determined by the University of Almeria, Spain (Department of Soil Science). The pH value and total element composition were analyzed by the geochemical laboratories of GFZ Potsdam, Germany.

The soil analysis in Almeria followed the standards outlined by the American Society of Agronomy and Soil Science Society of America (Page et al. 1982; Klute 1986). Before laboratory analysis, the soil samples were air dried and passed through a 2 mm sieve. The particle size distribution was determined by wet sieving the sand fraction and using the pipette method for silt and clay fractions after the removal of organic matter with H_2O_2 and dispersion with Na-hexametaphosphate. The chemical analysis was performed on the soil's 2-mm sieved fine earth fraction. The soil organic carbon content (SOC) was determined using the Tyurin method by wet combustion with a mixture of $K_2Cr_2O_7$ and H_2SO_4 and titrating the residual dichromate with ferrous sulfate. The $CaCO_3$ equivalent was

determined by exposure to acid in a closed system to form CO_2, (pressure calcimeter method).

The free iron oxides (Fe_d) were extracted with citrate-dithionite using the Holmgren method (Holmgren 1967) and determined by atomic absorption spectroscopy. The dithionite-citrate reagent extracts iron from most of the pedogenic/secondary iron oxides or referred to as the free iron oxides, whereas others extraction procedures are more selective for certain materials (e.g. oxalate reagent for ferrihydrite). A good effectiveness (>80 %) of the citrate-dithionite reagent to estimate ferrihydrite, goethite, hematite, lepidocrocite and maghemite was found by Parfitt and Childs (1988). But some crystalline iron oxides may only be partly dissolved with one single dithionite treatment requiring several treatments to extract the complete amount (Parfitt and Childs 1988).

For 13 representative soil samples, the pH values were measured in 0.01 mol $CaCl_2$ suspension using a pH glass electrode. The predominant clay mineral cations (Al^{3+}, Mg^{2+} and $Fe^{2+/3+}$) of the soils were spectrally analyzed by measuring the clay absorption positions before and after heating the samples to 600° for 8 hours as suggested by Ben-Dor and Banin (1990). This treatment enhances specific absorption features by removing the strong overlapping effect of free and absorbed water and starts a partial dehydroxylation of the crystals. Using X-ray fluorescence (XRF), the total element composition was analyzed of the 13 soil and additional eight surface rock samples.

Additionally, a representative portion of each soil sample was homogenized by milling the sample for 2 minutes for the subsequent laboratory spectral analysis (Figure 4.1).

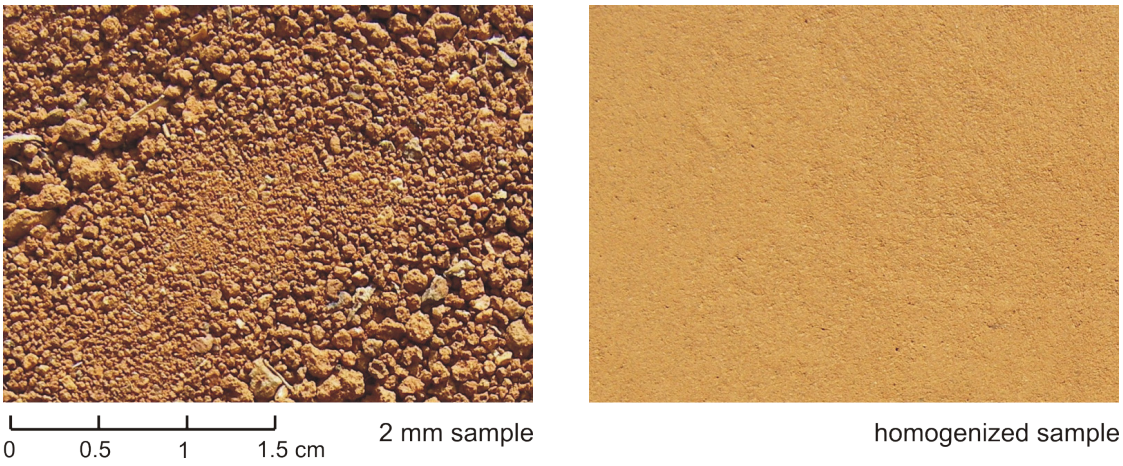

Figure 4.1: Pictures of one sample before (2-mm sieved fraction) and after homogenization.

4.2 Spectrometric data

4.2.1 Laboratory data

The spectral reflectance measurements in the laboratory allow studying specific influences on the reflectance through systematic change of individual parameters under controlled conditions. The varying soil properties (chemical and textural) and vegetation cover largely govern the soil reflectance properties in the natural environment. Two laboratory reflectance measurement series were performed investigating the impacts of both parameters independent of each other.

Spectral reflectance measurements were taken with an Analytical Spectral Devices (ASD) Field Spec® Pro FR Spectroradiometer (ASDI 2002). The ASD spectrometer covers the spectral range from 350 to 2500 nm in 2151 spectral bands with a sampling interval of 1.4 to 2 nm (Table 4.2) and interpolated 1 nm bandwidth. The incident light is collected by a glass fibre optic cable and randomly distributed to the three integrated spectrometers. The bare fibre has a 25° field of view (FOV) that can be reduced by different fore optic lenses (e.g. 1°, 8°). Absolute reflectance spectra are obtained by taking reflectance measurements relative to a Spectralon® surface.

Table 4.2: Characteristics of ASD Field Spectrometer (ASDI 2002).

	VIS/NIR	**SWIR I**	**SWIR II**
Wavelength range	350-1000 nm	1000-1750 nm	1750-2500 nm
Detector	Si - detector	InGaAs - detector	InGaAs - detector
Sampling interval	1.4 nm	2 nm	2 nm
Noise Equivalent Δ Radiance	$1.4*10^{-9}$ W/cm^2/nm/sr at 700 nm	$2.4*10^{-9}$ W/cm^2/nm/sr at 1400 nm	$8.8*10^{-9}$ W/cm^2/nm/sr at 2100 nm
Spectral resolution	3 nm at 700 nm	10 nm at 1500 nm	10 nm at 2100 nm

During first measuring series, the relationship between the soil chemical and textural properties and their influence on reflectance properties was examined. Three different grain sizes of each sample (the original, the 2-mm sieved and homogenized fraction) were measured under identical setup. The measurements were performed in a dark room. Illumination source was a 2000 W Tungsten lamp located approximately 1.5 m above the sample with a 30° incidence angle. The nadir-looking sensor with 25° FOV was mounted 5 cm above the sample yielding an approximate circular measuring area of 2.2 cm diameter. Fifty consequent measurements were averaged for a single reflectance spectrum

of a surface. Three separated reflectance spectra were measured for each sample and subsequently averaged to obtain a mean reflectance spectrum.

The second measuring series aimed to determine the critical vegetation cover for quantifying soil chemical parameters. Reflectance measurements were taken of one representative soil with varying leaf cover and vitality states. The experimental setup for the measurements (Figure 4.2) used the same illumination conditions as the first experiment (height approx. 1.5 m above the sample, 30° incidence angle). The nadir-looking sensor with 25° FOV was mounted 12 cm above the sample surface yielding a measuring area of 5.2 cm diameter.

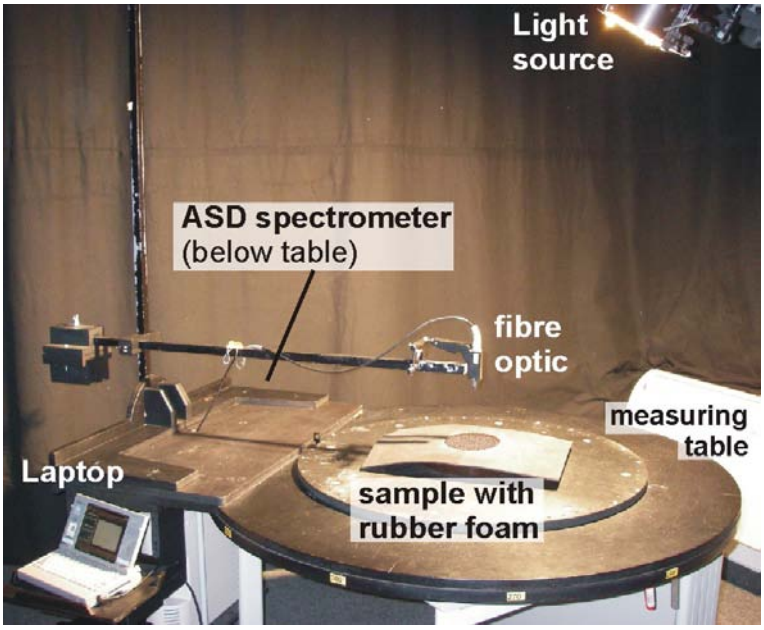

Figure 4.2: Setup for spectral measurement in the laboratory.

The selected soil represents the typical iron oxide-rich soils from Cabo de Gata samples. The soil was placed into petri-dishes, surfaces was cleaned from vegetation residues and slightly compressed to obtain a flat surface. Consecutively, photosynthetic active (PV) green grass leaves (grown standard grass mixture), non-photosynthetic active (NPV) dry grass leaves (short grass collected in the study area) and a mixture of both (MIX) were placed on the soil surface and spectral measurements were taken (Figure 4.3). The leaves laid flat on the soil surface so shadow effects were minimized. Prior to each reflectance measurement, the leaf cover was increased by adding more leaves onto the soil surface. The percentage leaf cover on the soil surface was estimated from pictures taken before the

measurement by masking the leaves and then calculating the percent fraction of leaves on the total surface area. For the MIX leaf cover experiment the fractions of green and dry vegetation were determined separately.

Between 14 and 20 steps of adding leaves were necessary until the spectral influence of the leaves dominated the soil signature. Multiple spectral measurements were taken from soil surface and each leaf cover step to assure that the reflectance spectra represent the estimated leaf cover. Two spectral measurements were taken in the middle of the sample and additional eight around the middle while rotating the sample clockwise. The spectra were averaged to obtain a single spectrum for each surface. A black rubber foam sheet was fitted around the bowl to inhibit reflectance from the surrounding material, because it returns a featureless spectrum with less than 7 % reflectance in the VIS-SWIR wavelength range.

(a) PV: green grass (b) NPV: dry grass (c) MIX: mixture of PV and NPV

Figure 4.3: Pictures of iron-dominated soil surface with about dry, green and mixed grass leaf coverage.

The spectral pre-processing comprised four general steps. First the measured reflectance spectra were corrected for the absorption characteristics of the used Spectralon panel and transferred into an ENVI spectral libraries format. Then a visual inspection of all spectra was performed to identify erroneous measurements and verify the experiment protocol. The third step comprised the correction of possible detector jumps at the transition of the three integrated ASD detectors. Therefore the second detector was used as master while the first and third detector data were adjusted to this level. Finally multiple spectral measurements of one sample were averaged to obtain a single reflectance spectrum.

4.2.2 Hyperspectral image data

Airborne HyMap images of Cabo de Gata were acquired on June 15, 2005 during the DLR HyEurope2005 campaign. HyMap, the Hyperspectral Mapper, is an airborne whiskbroom imaging spectrometer covering the spectral range between 440 and 2500 nm with an average bandwidth of ~16 nm in 128 spectral bands. The instantaneous field of view is 2.5 mrad along and 2.0 mrad across track, and the total field of view is 61.3 degrees, resulting in 512 image pixels per scanline. The wavelength-dependent sensor's signal-to-noise ratio (SNR), given by Cocks et al. (1998), for an object with 50 % reflectance and 5 m instantaneous FOV is 1200:1 for the VIS/NIR and 900:1 (from 1400 to 1900 nm) respectively 600:1 (from 1900 to 2400 nm) for the SWIR. The Cabo de Gata HyMap image data consisted of five individual flightlines (Hy-1 to Hy-5), which can be combined to a large mosaic (Table 4.3). Flightlines Hy-3 and Hy-4 cover the wide area of the soil sampling campaign and were examined in the frame of this study. The flightlines were acquired in north-south direction at noon between 11:30 and 12:30 UTC. The average flight altitude of 2645 m above sea level (asl) resulted in a 5 m x 5 m nadir pixel size.

The raw HyMap data were system corrected to at-sensor-radiance based on calibration coefficients obtained during laboratory calibration by HyVista. The subsequent geometric and atmospheric correction of the data sets were performed at the DLR using the program routines ORTHO (Schläpfer and Richter 2002) and ATCOR4 (Richter and Schläpfer 2002). In the first step the geometric correction was performed to enable the use of the digital elevation model (DEM) for the atmospheric correction which was done in the second step.

Table 4.3: Summary of HyMap data acquisition (asl = above sea level).

Flightline	**Hy-1**	**Hy-2**	**Hy-3**	**Hy-4**	**Hy-5**
Acquisition date	15.06.2005	15.06.2005	15.06.2005	15.06.2005	15.06.2005
Acquisition time (UTC)	11:30	12:02	11:41	12:21	11:53
Heading	360°	180°	180°	360°	360°
No. of scan lines	3525	3849	3703	2950	2967
Flight altitude (asl)	2645 m	2645 m	2645 m	2645 m	2645 m
Spatial resolution	5 x 5 m	5 x 5 m	5 x 5 m	5 x 5 m	5 x 5 m

The imagery was geocoded using the parametric approach implemented in ORTHO (Schläpfer and Richter 2002). The geocoding was done automatically by determining the

viewing geometry for each pixel based on sensor-specific parameters, flight parameters such as sensor position and attitude (i.e. roll, pitch, yaw), and additional terrain information from the DEM. The used DEM has a 10 x 10 m resolution and was generated from air photo aerial survey by Junta de Andalucía (2005). The UTM coordinate system, zone 30 North with datum "European 1950 mean" was chosen as final geographic system. The typical accuracy obtained from the procedure is ±2 pixels.

The geometric accuracy of the Cabo de Gata data sets was evaluated relative to each other (image vs. image) and absolute against field GPS measurements (Figure 4.4). The field campaign included GPS measurement of nine road intersections which were randomly located within the area of the flight lines. The measurements were done in the middle of the intersection using a hand-held GPS with an approximate accuracy of 4 m. The relative geometric error in the overlapping area of both flightlines was determined to be at maximum 4 pixels (20 m) in x- and y-direction. The average error of the two flightlines in the overlapping region is ±10 m. Systematic errors were not observed. The geocoding of the individual data sets resulted in a pixel to sub-pixel accuracy based on the field GPS measurements. The average error of x-coordinate is ~8.2 m and of y-coordinate ~3.6 m. The average deviation to digitalized maps in the scale of 1:50.000 is also below 20 meters. Comparing the spatial resolution of the HyMap data to the by factor 2 coarser DEM resolution, this result represents the expected accuracy.

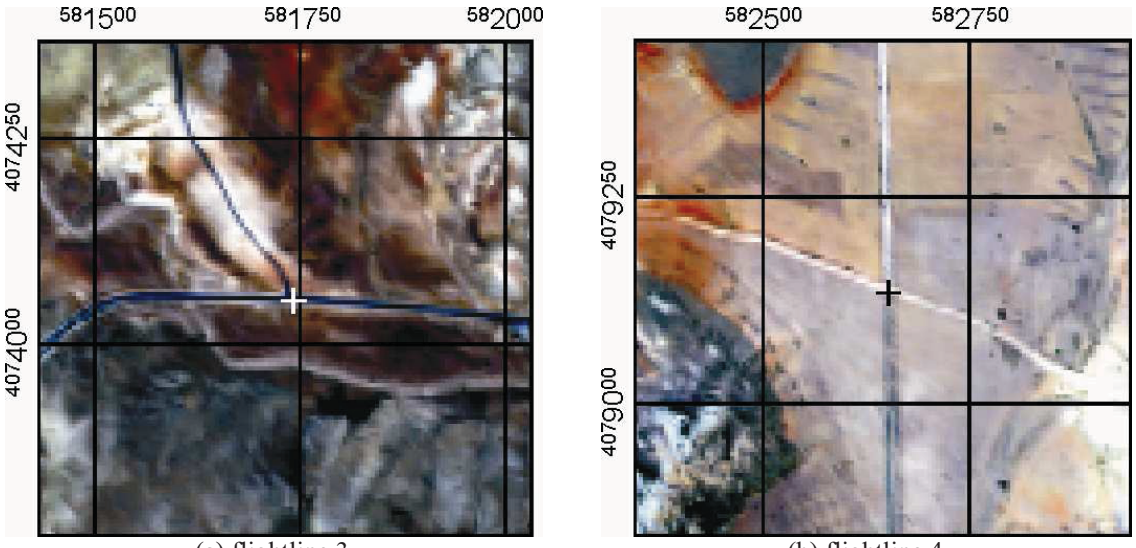

(a) flightline 3 (b) flightline 4

Figure 4.4: Evaluation of geometric correction by field GPS measurements. HyMap spatial resolution 5 x 5 m, grid size: 250 m.

The atmospheric correction was performed with ATCOR4 software (Richter and Schläpfer 2002), which is part of the processing chain at DLR (Habermeyer et al. 2005). This physically based approach, using the MODTRAN radiative transfer code, calculates the nadir-normalized ground reflectance from the at-sensor radiance. This requires correction of atmospheric influences (absorption and scattering processes) under consideration of flight and solar geometry (scan and azimuth angles, path length through the atmosphere) as well as the correction for adjacency scattering effects of the neighborhood. Furthermore topographic correction for different terrain illumination is applied using the DEM with 10 x 10 m resolution. Absorption and scattering properties of the particles and the wavelength dependence of the optical properties are characterized by the aerosol type. The 'rural' aerosol type was chosen for both data sets because of the winds mainly continental origin including dust entry that dominates the direct proximity to the sea. A constant aerosol optical depth (visibility) of 40 km was used for both data sets. The water vapor column was estimated automatically on a pixel by pixel basis from the data using the 940 nm and 1130 nm water vapor bands.

The optimal correction for absorption features of the atmospheric gases (e.g. water vapor, oxygen) requires an accurate spectral calibration of the data in the particular wavelength regions. Otherwise spectral artifacts in terms of dips and spikes may appear in the final reflectance spectrum indicating over- and under-correction due to shifted band center positions (Richter et al. 2008). During the ATCOR processing, the spectral calibration is optimized on the basis of the 760-nm oxygen absorption and water absorption regions centered at 815, 940, 1130, 1380 and 1850 nm each time including between 3 to 7 HyMap bands.

To ensure the quality of the atmospheric correction, the resulting ground reflectance values were validated against reference targets measured in the field (Figure 4.5). Further the relative accuracy of the atmospheric correction was evaluated by comparison of homogenous areas in the overlapping region of the flight lines. No field calibration measurements were available for the 2005 HyMap overflight. The accuracy evaluation was therefore performed with calibration measurements taken for the same purpose during a previous HyMap campaign in May 2004.

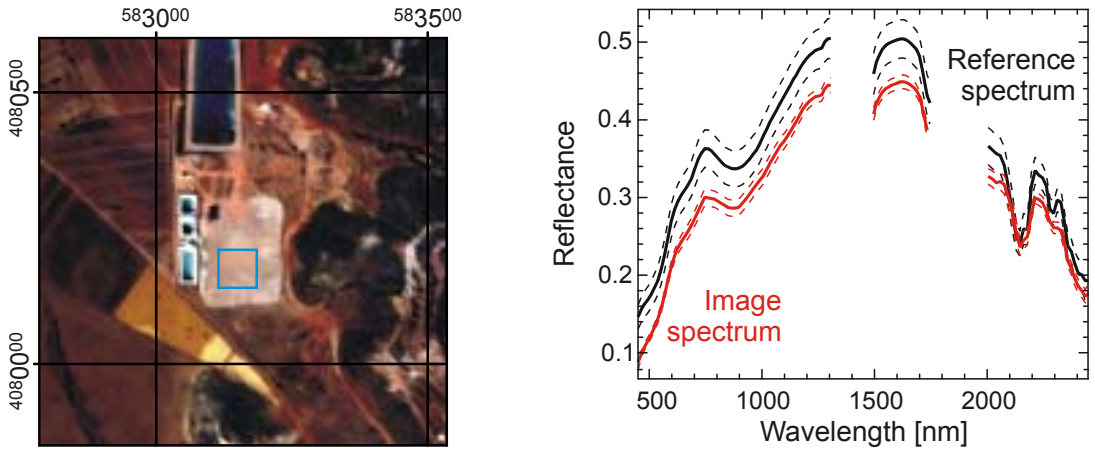

(a) Reference area on gravel pile. Edge length of measuring square: 70 m

(b) Comparison reference (field) spectrum - image spectrum. The dotted lines mark the standard deviation.

Figure 4.5: Evaluation of radiometric calibration. The reference spectrum refers to the ASD field measurements taken in 2004 on the gravel pile.

Figure 4.5b depicts the average field spectrum of a large, flat and homogeneous gravel pile in Cortijo del Fraile from 2004, which was found to be almost spectrally invariant during the years (Bachmann 2007). The corresponding 2005 HyMap image spectrum reflects a very similar spectral shape but lower overall albedo then the reference spectrum. The comparison of the HyMap image spectra with other potentially invariable reference targets (spectral field measurements of two beach sediments) confirms a general trend of slightly lower image albedo. The large time difference between the calibration measurements and HyMap data acquisition might be one explanation. For the 2004 field measurements strong winds were described increasing the amount of dust in the air (unpublished campaign documentation by M. Bachmann 2004). Dust particles affected especially the VIS/NIR part of the spectrum. Accordingly larger deviations between field and image spectrum were found in this wavelength region than the SWIR. The VIS/NIR absorption bands were only minor affected (less than 1 % loss of absorption intensity in the image compared to field data). However the atmospheric correction corresponded to the expected quality because the lower albedo affected the entire image and the relative comparison between both flightlines exhibited only minor variations. A extensive description of the geometric and radiometric processing results and evaluation of the used HyMap images is given in Bachmann (2007).

4.3 Spectral absorption feature analysis

4.3.1 Spectral feature extraction

The continuum removal of hull-normalization is the first step of the spectral absorption feature analysis used to isolate particular absorption band for the analysis. The reflectance spectrum is composed of two components, the continuum and the individual absorption features (Figure 4.6). The continuum represents the background absorption characterizing the general shape of the spectrum and e.g. the wing of a larger absorption feature, onto which other absorption feature are superimposed (Clark and Roush 1984; Clark 1999). Significant slopes in the spectra can cause an apparent shift in the reflectance minimum. The continuum should be removed in order to obtain the true absorption band centers and band depths. It further removes albedo differences between the spectra and allows the comparing of spectral absorption bands between spectra from a common baseline (Clark and Roush 1984).

An enveloping hull function, H, is fitted over each spectrum, Sp, forming an absorption free continuum (Figure 4.6a). The spectrum is then divided by this continuum function. Through the definition of the continuum, a consistent definition of the band depth, *d*, is provided:

$$d = 1 - \frac{r_{Sp}}{r_H} \qquad 4\text{-}1$$

where r_{Sp} is the reflectance at the band center and r_H is the reflectance of the continuum at the same wavelength (Clark and Roush 1984).

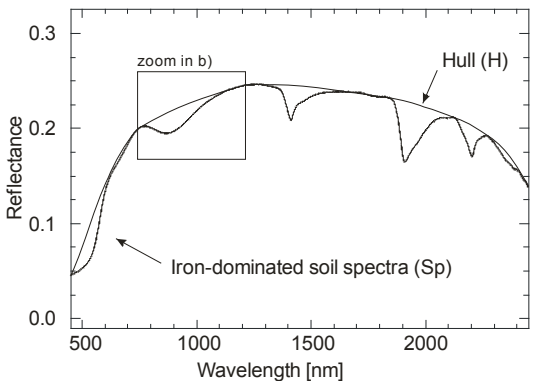

(a) Definition of hull function (H) for an iron-dominated spectrum (Sp)

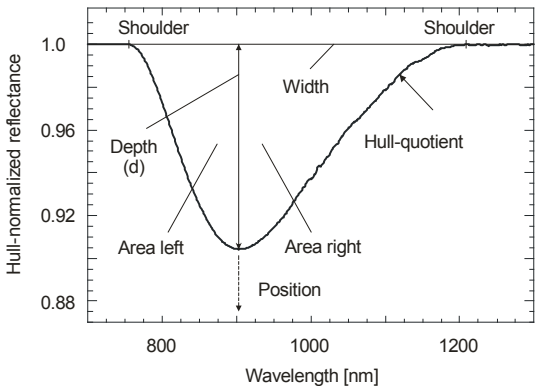

(b) Characterization of spectral feature absorption parameters in the hull-normalized spectrum

Figure 4.6: Scheme of hull-normalization (continuum removal).

Besides absorption depth, other spectral features characterizing the absorption band were extracted from the continuum-removed spectrum (Figure 4.6b); wavelength position, absorption width, area, and left and right spectral areas as measured for the absorption bands asymmetry (van der Meer 1995). First, the shoulders of the absorption band were determined, which have normalized reflectance of 1. This was done automatically for each single spectrum because the width of the absorption band may vary with the quantity of the absorbing material. Subsequently the absorption band center was determined and consequentially all other features were derived.

The soil samples reflectance spectra measured in the laboratory were hull-normalized between 430 and 2400 nm excluding the wavelengths which contained increased impact of sensor noise. The spectral features (e.g. depth, width, area) of the VIS ($^6A_{1g} \rightarrow {}^4A_{1g}, {}^4E$) and the NIR ($^6A_{1g} \rightarrow {}^4T_{1g}$) iron absorption bands were extracted automatically from the hull-normalized reflectance spectra within the wavelength ranges summarized in Table 4.4. Both absorption bands are further referred to as Fe-VIS and Fe-NIR. The wide wavelength ranges of the feature extraction were chosen to ensure covering the whole absorption band because both width and depth of an absorption band can be related to the quantity of the absorbing material.

Table 4.4: Absorption maximum position and wavelength ranges of soil and vegetation spectral features for automatic extraction procedure.

Absorption band	Absorption maximum	Wavelength (start)	Wavelength (end)
Fe-VIS ($^6A_{1g} \rightarrow {}^4A_{1g}, {}^4E$)	480-550 nm	430 nm	620 nm
Fe-NIR ($^6A_{1g} \rightarrow {}^4T_{1g}$)	880-930 nm	750 nm	1200 nm
clay (cation-OH)	~2200 nm	2120 nm	2280 nm
carbonate (C-O)	~2335 nm	2280 nm	2400 nm
chlorophyll (chl a+b)	~500 nm	430 nm	600 nm
chlorophyll (chl a+b)	~660 nm	530 nm	760 nm
plant water	~970 nm	900 nm	1080 nm
cellulose	~2100 nm	2010 nm	2220 nm

4.3.2 Modeling and validation

The correlation between Fe_d and the normalized reflectance spectra was described using Pearson's product-moment correlation coefficient (R). In order to adapt Pearson's model, input data were tested for a normal distribution using the Kolmogorov-Smirnov test (Sachs 2002). Both linear and non-linear functions were used to model the relationship between

the Fe_d content and the spectral absorption features. The non-linear function was characterized by a power function:

$$Y = a * X^b. \quad 4\text{-}2$$

where *Y* is the Fe_d content (response variable), *X* the spectral feature used for prediction (predictor variable) and *a* and *b* are model parameters. Fe_d contents exceeding the models calibration range may exhibit intensity saturation of the absorption band, limiting the applicability of the models. To allow the application of linear regression models, the power function (4-2) was transformed into a natural logarithmic (n-log) data space (Bronstein et al. 2000):

$$\ln Y = b * \ln X + \ln a. \quad 4\text{-}3$$

The transformed input data (response and predictor variables) were tested for normal distribution. The predicted Fe_d values were re-transformed into linear space and compared with the measurements.

Model significance (residuals mean equals zero) was tested using a t-test. The normal distribution of the residuals was tested and auto-correlation was ruled out by the Durbin-Watson-test to ensure the accurate usage of linear regression models (Backhaus et al. 1990; Bahrenberg et al. 1999a, b).

As validation method for the models results, the cross-validation using the 'leave-one-out' method was chosen (Martens and Næs 1989). Therefore the model was calibrated *N* times for *N*-1 samples in the data set, each time predicting the excluded sample of the data set. In the end all samples were predicted by an independent empirical-statistical model and were then used to assess the prediction accuracy. To evaluate the model performance, the following statistical parameters were calculated (Backhaus et al. 1990; Bahrenberg et al. 1999a). The index v was added (R^2_v, $RMSE_v$, rel. $RMSE_v$, RPD_v) for cross-validated results:

Pearson's correlation coefficient: $R = \frac{\sum_{i=1}^{n}(x_i-\bar{x})\cdot(y_i-\bar{y})}{\sum_{i=1}^{n}(x_i-\bar{x})\cdot\sum_{i=1}^{n}(y_i-\bar{y})}$

Coefficient of determination: R^2

Standard error of prediction: $RMSE = \sqrt{\frac{\sum_{i=1}^{n}(y_i-x_i)^2}{n}}$

Relative root mean-squared error: $\text{rel. RMSE} = \frac{\text{RMSE}}{\bar{y}}$

Residual prediction deviation: $\text{RPD} = \frac{s(x)}{\text{RMSE}}$

with x_i as Fe_d content predicted from the spectral feature, y_i as true Fe_d content obtained from the chemical analysis, $\bar{x}$ and $\bar{y}$ as arithmetic mean of x and y, and n as number of all samples. The standard deviation (S.D.) s(x) was determined as follows:

$$s(x) = \sqrt{\frac{\sum(x-\bar{x})^2}{(n-1)}}\,. \qquad 4\text{-}4$$

With increasing interest, the RPD value is used in the soil sciences as a meaningful unitless statistics for instant evaluation of the analytical efficiency of calibrations (Dunn et al. 2002; Malley et al. 2004; Cohen et al. 2007). Dunn et al. (2002) suggested three suitable categories for evaluating the performance of soil analysis with NIR reflectance spectroscopy: RPD > 2.0 (excellent), RPD 1.6 to 2.0 (acceptable), RPD < 1.6 (poor). Very similar RPD limits were identified by Chang et al. (2001) and Cohen et al. (2007) for soil spectroscopic investigations with the upper RPD boundary at 2.0 and the lower at 1.4 and 1.5, respectively. In contrast, Malley et al. (2004) categorized the RPD values in four groups ranging between 0 and > 4 as a guideline for evaluation calibrations for various environmental samples including soils, sediments, compost, etc.

Chapter 5: Laboratory spectral determination of pedogenic iron oxide content

The variety of parent materials and climatic conditions has led to a high soil diversity in the study area. Small scale variations in physiogeographic factors such as relief, microclimate and vegetation cover have generated a complex spatial pattern of soil types. The associated heterogeneity of soil physicochemical properties (e.g. texture, soil organic carbon, iron oxide and carbonates) is reflected in the spectral behavior of the soil surfaces.

The weathering of the parent material by transformation (e.g. dissolution, oxidation) or translocation of primary minerals provides the source material for soil development. Minerals released during weathering are either removed from the system by leaching water or react in the system to form a variety of crystalline and amorphous products (Birkeland 1999). The weathering products of rocks are governed by their original mineralogical composition. The main minerals of the volcanic rocks andesite and dacite in the study area are plagioclase, quartz, pyroxene and to lesser extent biotite and amphibole (hornblende). While quartz is a resistant mineral in most environments, the weathering of other silicate minerals (plagioclase, hornblende…) leads mostly to the formation of clay minerals (e.g. kaolinite, montmorillonite, smectite). The weathering proceeds faster with higher biotite content of the source rocks (Birkeland 1999). The released iron is mainly precipitated in the form of iron (III) oxides under aerobic conditions either at the site of weathering or after translocation. The translocation of ferric iron requires an acidic environment with $pH < 4.3$ (Nordstorm and Alpers 1999), thus no removal of iron by soil water is expected in neutral and alkaline soils. Hence the formation and accumulation of iron oxides is an indication for the continuous weathering and soil development (Birkeland 1999).

The main process of carbonate rock weathering is the dissolution and subsequent removal of carbonates, whereas insoluble elements and minerals, such as iron, mica and clay minerals remain and accumulate as soil developing components. Thus, mature soils on

carbonatic bedrock show very different chemical composition often associated with lower carbonate content than the parent material. Weakly developed soils on the other hand show a similar chemical composition as their parent rocks with high amounts of carbonate. With the continuous soil development, increasing reddening of the soils (rubification) can be noticed which reflects the continuous accumulation of iron oxides (Birkeland 1999; Scheffer and Schachtschabel 2002).

Besides mineral soil components, organic carbon (SOC) is found in varying amounts in the soil. SOC is an important parameter for the pedogenesis and stability of the soil surface and an indicator for the soil quality and condition. The proportion of SOC depends strongly on the climatic conditions. In semi-arid regions, water is the limiting factor for the vegetation development, which provides the base for the formation of SOC. Small scale variability in SOC content occur due to variable vegetation cover, whereas the type of plants have a direct influence on the quality of the organic carbon and thus on the stability of the soil surface (Aranda and Oyonarte 2005).

5.1 Statistical description of soil samples

Preceding the description of the relationships between soil chemical properties and reflectance spectra, the results from the laboratory soil chemical and texture analysis are shortly outlined. The statistical description of the soil samples aims at the examination of potential grouping in terms of chemical or textural properties and their suitability for subsequent modeling.

5.1.1 Rock and soil XRF analysis

The soil development is directly linked to the weathering processes of the parent material. For analyzing and evaluating the soil physicochemical properties, it is necessary to examine whether the soil forming material derived directly from the underlying parent material or was transported from other sources. For this purpose the chemical composition of eight rock and 13 soil samples was investigated with XRF (Figure 5.1). The soil and rock samples were collected on top of volcanic (biotite-amphibolic dacites) and carbonatic (calcarenites) bedrocks during several field campaigns. No unweathered rocks were accessible in the sample area; thus all collected surface rocks exhibit variable degrees of surface oxidization.

The volcanic rocks of the area were mainly andesites and dacites. According to the different mineral composition of the rocks, the Fe_2O_3 content varied between 1.9 and 8.9 g kg^{-1}. The CaO and CO_2 concentrations were in general very low except for one rock sample. It was collected from a soil surface which contained also pedogenic carbonates. These might have covered the rock partly and caused the increased CaO and CO_2 concentrations. In general, the volcanic region comprised a large variety of different rocks, which could not be represented sufficiently by the collected samples (see Figure 3.2). Hence additional XRF results of Cabo de Gata volcanic rocks from the literature (see Cunningham et al. 1990; Caballero et al. 1991) were examined for a more comprehensive geochemical characterization of the geological conditions (Table 5.1). Both Fe_2O_3 and CO_2 content of the collected volcanic rock samples agreed with published values. However the literature CaO values were significantly higher ranging between 5 to 10 % (Cunningham et al. 1990; Caballero et al. 1991). This could possibly be explained by the removal of Ca from the weathered outcrop rocks compared to the fresher nature of the samples investigated in the literature.

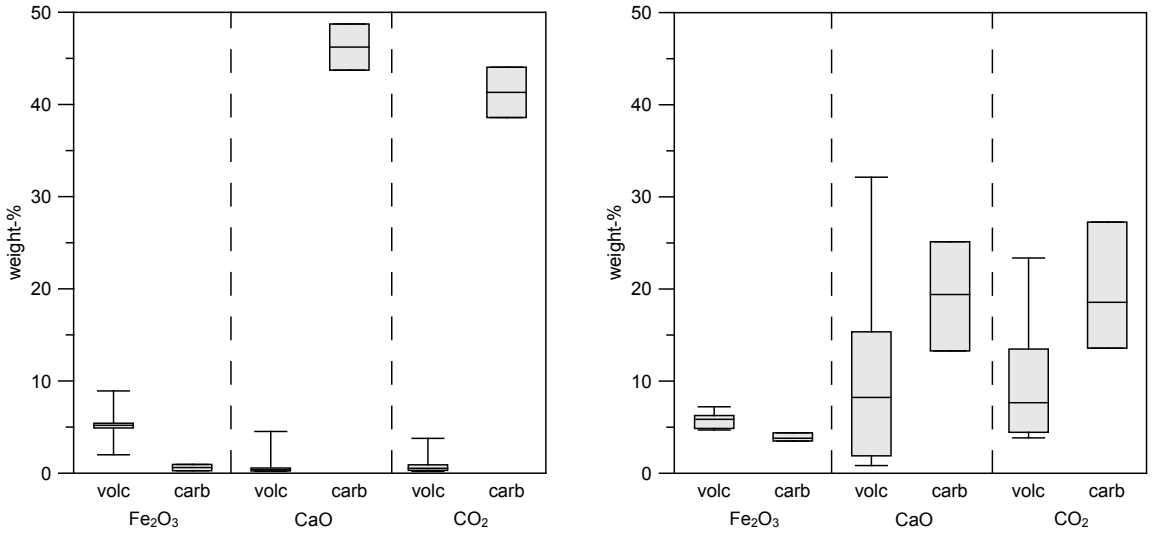

(a) **rock samples**: volcanic (N=6) and carbonatic type (N=2)

(b) **soil samples**: volcanic (N=9) and carbonatic type (N=4)

Figure 5.1: XRF results for volcanic and carbonatic rock and soil samples (total iron as Fe_2O_3).

The volcanic soils comprised a similar range of Fe_2O_3 or total iron oxide (Fe_t) content as the volcanic rocks (see Figure 5.1). The increased minimum Fe_t content and slightly increased mean value could be attributed to accumulation of iron oxides during pedogenesis. The volcanic soil samples showed highly variable CaO and CO_2 contents which exceeded the parent material significantly. In total seven of nine soil samples were

characterized by similar high quantities of both CaO and CO_2 indicating the presence of pedogenic carbonates. These were formed when released Ca-ions from parent material reacted with CO_2 of the soil air (Machette 1985). The accumulation of pedogenic carbonates was observed especially in dry regions, where the available water was not sufficient to dissolve and remove all newly formed carbonates. Two samples showed a composition that differed clearly from the other material. Their sampling location did not give a straightforward explanation for this. It is noteworthy that their very high carbonate content was accompanied by low silicate content and vice versa.

Table 5.1: XRF analysis of typical volcanic materials in the study area (Cunningham et al. 1990; Caballero et al. 1991).

	own data	Caballero et al. 1991			Cunningham et al. 1990			
Content weight-%	**mean**	**amphibolic andesite**	**amphibolic dacite**	**pyroxenic andesite**	**pyroxene andesite**	**dacite (black, glassy)**	**dacite**	**dacite**
Fe_2O_3*	5.27	5.15	4.34	6.7	9.73	5.44	5.1	4.7
CaO	1.04	6.55	7.08	8.28	10.1	5.06	5.45	5.58
CO_2	1.04	2.2	1.76	-	0.04	0.02	0.02	0.02

*total iron as Fe_2O_3

The other dominant rock types were carbonatic rocks which underlay approximately 65 % of the entire study area. The two examined carbonatic rock samples contained only small amounts of MgO (2 and 2.8 %) indicating a clear domination of Ca-carbonates over dolomite. Iron occurred in minor quantities as impurities in the rocks. The carbonatic soils contained about half the CaO and CO_2 and three to four times more Fe_t than their parent rocks. The relatively high Fe_t content in the carbonate soil implied the accumulation of iron oxides in the process of soil rubification. In contrast, the still relatively high carbonate content was often an indication for less developed soils. However, the aridic soil moisture regime in the study area (Aranda and Oyonarte 2005) suggested only little or no leaching processes and carbonate accumulation in the soil profile.

In the transition zone of carbonatic and volcanic rocks, the soils exhibited chemical characteristics of both parent materials. The influence of the bedrock was especially prominent in less developed soils, which covered most of the mountainous regions in the study area. The better developed soils also reflected the parent material because leaching processes were limited due to reduced water availability. Therefore the subsequent analysis of soil physicochemical properties and spectral reflectance characteristics had to take into account the encountered the geology.

5.1.2 Soil quantitative chemical analysis

The results of the laboratory chemical analysis of all soil samples are summarized in Table 5.2. The SOC content of 4.4 to 15.8 g kg^{-1} was relatively low except for two samples. These exceeded 20 g kg^{-1}. They were collected in a mountainous area under matorral vegetation where higher amounts of available plant residues enabled higher rates of SOC formation and accumulation. The $CaCO_3$ contents varied highly among the samples due to the variable geological conditions. Two-thirds of the samples contained less than 100 g kg^{-1} $CaCO_3$, the remaining up to 580 g kg^{-1}. The Fe_d content ranged between 3.5 and 33.7 g kg^{-1} and was normally distributed unlike the other parameters. The determined p-value for Fe_d of 0.2 (see Table 5.2) was larger than level of significance ($\alpha = 0.05$), thus normality assumption was feasible (Bahrenberg et al. 1999a). This was also confirmed by the skewness which was significantly lower than 1 indicating a normal, symmetric distribution. This was an essential requirement for application of Pearson's correlation coefficient and linear regression modeling. For both SOC and $CaCO_3$ data sets the Kolmogorov-Smirnov test returned p-values < 0.05 which led to the rejection of the normality hypothesis. The positive skewness values indicated a right skewed, asymmetric distribution of both data sets.

Table 5.2: Descriptive statistics of chemical analysis results for all 50 soil samples and test of normality.

	Min	Max	Mean	Median	S.D.	Skewness	Kolmogorov-Smirnov test (*)		
							statistic	df	significance (p)
Fe_d [g kg^{-1}]	3.5	33.7	19.2	20.3	8.4	-0.218	0.100	50	0.200
SOC [g kg^{-1}]	4.4	27.9	10.1	9.3	3.9	2.498	0.208	50	0.000
$CaCO_3$ [g kg^{-1}]	3	580	99.8	47.5	131.7	2.046	0.231	50	0.000

* Lilliefors Significance Correction.

The Fe_d content comprises the proportion of free iron oxides in the soil, which is generally lower than Fe_t (see methods chapter 4.1). The ratio Fe_d/Fe_t is used as a measure to evaluate the degree of weathering of primary iron-bearing minerals (Mirabella and Carnicelli 1992; Birkeland 1999) and to estimate relative soil age (Arduino et al. 1986). For six soil samples both Fe_d and Fe_t were determined. According to Birkeland (1999) a factor of 1.43 was needed to converted between elemental iron and iron oxides (Fe_2O_3). The average Fe_d/Fe_t ratio was 0.58 for four volcanic soils, which were classified as Luvisols and Calcisols. The two remaining carbonatic samples classified as Calcaric Regosols yielded a Fe_d/Fe_t ratio of

only 0.18 indicating a significantly lower degree of weathering than the volcanic soils which agreed with their soil type classification.

When evaluating the soil samples chemistry with respect to their geological background significant differences were found (Figure 5.2). Soil samples collected from carbonatic substrata were characterized by a low Fe_d (7 g kg^{-1} on average) and high $CaCO_3$ content (340 g kg^{-1} on average). The opposite applied for the samples from volcanic substrata where high amounts of free iron oxides (20 g kg^{-1} on average) were characteristic. Their lower $CaCO_3$ content ranged between 3 and 97 g kg^{-1} and could partly be attributed to the presence of pedogenic carbonates. Twelve samples were collected from soil that developed in the transition zone between volcanic and carbonatic rocks. These samples were characterized by significantly higher $CaCO_3$ concentrations than the majority of volcanic samples. However, in contrast to the carbonatic soils, their Fe_d content was comparable to the volcanic samples.

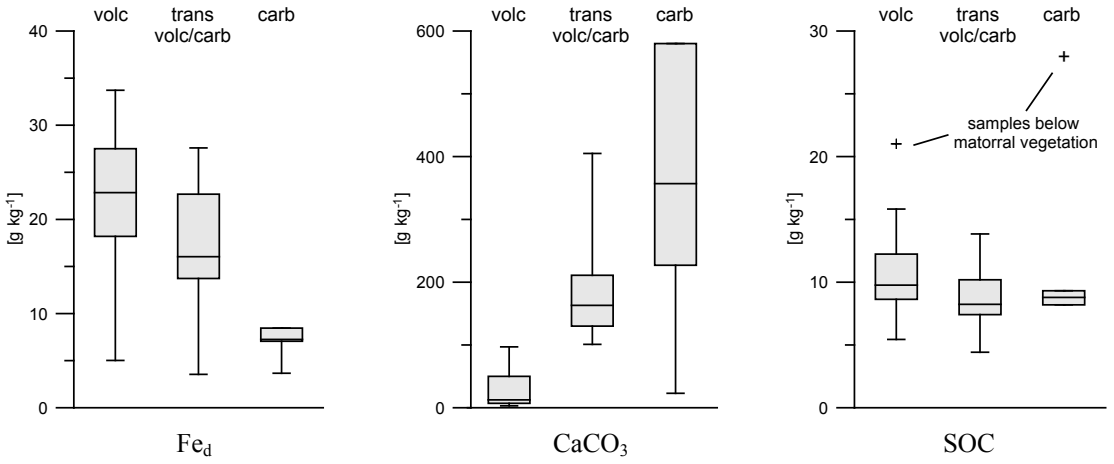

Figure 5.2: Soil chemical composition of 33 volcanic (volc), 5 carbonatic (carb) and 12 soil samples from the transition between volcanic and carbonatic bedrock (trans volc/carb).

5.1.3 Texture analysis

The grain size analysis of the 50 soil samples showed a heterogeneous distribution, ranging from sandy loam to clay loam and clay (FAO 2005). Clay and sand content were highly variable (Figure 5.3). This was of special importance to the spectral reflectivity of pedogenic iron oxide, because iron occurred mainly as coatings on the grain structure of sandy soils and was not randomly distributed as in finer-grained soils. With increasing grain size and constant total volume, the grain surface area decreases. Thus coarse-grained

soils exhibit a considerable smaller surface area than finer-grained soils. Consequently in coarse-grained soils, iron occupies a larger portion of the reflecting surface than in finer-grained soil with equal concentration. Soils with high sand fractions can show fairly intensive iron absorption features at comparatively low iron concentrations (Jarmer 2005).

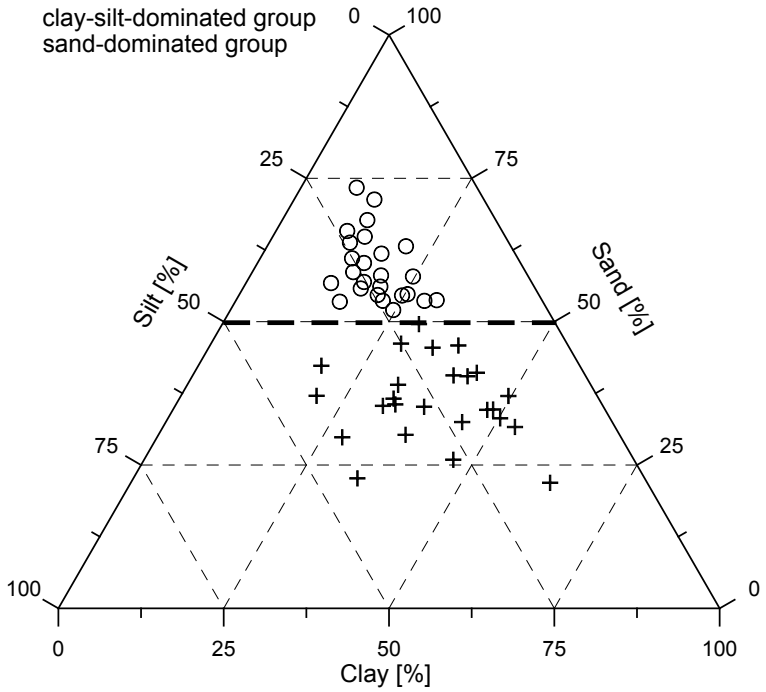

Figure 5.3: Particle size distribution and indicated soil texture groups of all samples. Thick dashed line represents 50% sand content.

Due to the high contents of either sand or clay in the samples, two soil texture groups were defined. The samples were divided into a clay-silt-dominated group and a sand-dominated group using 50 % sand content as limiting criterion. Table 5.3 summarized the texture variability of the sand, silt and clay fraction for each group. The clay-silt-dominated group was clearly more heterogeneous (S.D. ranges between 7 and 10.5) than the sand-dominated one (S.D. between 4 and 6).

Table 5.3: Soil texture variability in the sand-dominated and clay-silt-dominated groups.

	Sand-dominated group (N=25)				**Clay-silt-dominated group (N=25)**			
	Min	**Max**	**Mean**	**S.D.**	**Min**	**Max**	**Mean**	**S.D.**
Sand [%]	52.03	73.37	59.35	5.83	21.90	49.58	36.18	7.03
Silt [%]	15.91	30.70	22.23	4.07	13.43	43.44	25.32	9.47
Clay [%]	8.42	30.33	18.42	5.80	18.61	63.41	38.51	10.45

5.2 Spectral influence of soil physicochemical properties on surface reflectance

5.2.1 Pedogenic iron oxides

The ferric ion causes three main absorption bands in VIS and NIR wavelength range due to charge transfer processes and crystal field transitions (see chapter 2). Hematite and goethite are the predominating iron oxides/hydroxides in soils which exhibit distinguishable ferric absorption positions due to different crystal structures. Table 5.4 summarizes literature data for goethite and hematite absorption maxima. The differences between the results of these studies are caused by the usage of different spectrometer systems and impurities of the analyzed samples among others.

Table 5.4: Literature values of ferric ion absorption maxima in the VIS/NIR (Hm = hematite, Gt = goethite).

	$^6A_{1g} \rightarrow {}^4A_{1g}, {}^4E$ **Fe-VIS**	$^6A_{1g} \rightarrow {}^4T_{2g}$	$^6A_{1g} \rightarrow {}^4T_{1g}$ **Fe-NIR**
Hunt et al. (1971)	~0.4 µm	~0.7 µm	~0.87 µm
Hunt and Ashley (1979)	~0.45 µm	0.55-0.65 µm ~0.65 µm (Gt)	0.75-0.95 µm ~0.85 µm (Hm) ~0.94 µm (Gt)
Morris et al. (1985)	~0.55 µm (Hm) ~0.45 µm (Gt)	0.632-0.641 µm (Hm) 0.645-0.652 µm (Gt)	0.846-0.870 µm (Hm) 0.896-0.932 µm (Gt)
Grove et al. (1992)	0.535 µm (Hm) 0.503 µm (Gt)	0.665 µm (Gt)	0.868 µm (Hm) 0.9320 µm (Gt)
Jarmer (2005)		0.669 µm (Hm) 0.668 µm (Gt)	0.884 µm (Hm) 0.930 µm (Gt)

The reflectance spectra of the 50 investigated soil samples were dominated by two iron absorption bands induced by electronic transition processes from $^6A_{1g}$ to $^4A_{1g}$ (referred to as Fe-VIS) and from $^6A_{1g}$ to $^4T_{1g}$ (referred to as Fe-NIR). The iron absorption band caused by transition from $^6A_{1g}$ to $^4T_{2g}$ with absorption maximum near 640 nm was only very weakly developed and partly appeared as a shoulder. Apparently the fitted convex-hull did not abut on the neighboring bands of the absorption feature, so it appeared only as very low dip in the normalized spectrum. Other studies (Hunt et al. 1971; Morris et al. 1985; Ben-Dor et al. 2002) described this absorption band as most apparent for goethite, which, however, occurred mostly in mixtures with other iron oxides in the soil. Therefore, the subsequent analysis of the homogenized samples reflectance spectra was based only on the Fe-VIS and Fe-NIR absorption bands.

The Fe-VIS absorption in the reflectance spectrum represented only the right wing of a larger absorption region. By using a defined starting wavelength for the convex hull-

normalization (which was located at 430 nm in this study), an analyzable Fe-VIS absorption band with determinable maximum absorption position was derived. Depending on the wavelength at which convex hull fitting starts, the wavelength position of the Fe-VIS absorption band is subject to shift. For all 50 soil samples, the average Fe-VIS wavelength position was determined at 518 nm (Table 5.5). The entire Fe-NIR absorption band was covered by the spectra with an average wavelength position of the absorption maximum at 891 nm. For five soil samples, the detected Fe-NIR absorption positions ranged between 1004 and 1150 nm. The Fe_d content of these samples was very low 3.5 to 8.5 g kg^{-1} and did not induce a distinct Fe-NIR absorption. The determined wavelength positions were attributed to spectrometers background noise which overlaid potential iron absorption.

Table 5.5: Laboratory wavelength position of iron absorption maxima in the VIS/NIR range.

	Transition	N	Min	Max	Mean	S.D.
Fe-VIS	**($^6A_{1g}$ to $^4A_{1g}$)**	50	491 nm	523 nm	517.7 nm	7.5 nm
Fe-NIR	**($^6A_{1g}$ to $^4T_{1g}$)**	45	877 nm	933 nm	890.6 nm	10.7 nm

Both the mean Fe-VIS and Fe-NIR absorption maxima were determined in between the described wavelength positions of goethite and hematite absorption. This indicated a mixture of both iron oxides being present in the soils. Ben-Dor et al. (2006) investigated the spectral behavior of a synthetic goethite-hematite mixture on quartz basis and showed that the iron absorption position for equal amounts of hematite and goethite was located between the original absorption of the pure mineral absorption.

The intensity and character of the iron absorption bands were strongly influenced by the concentration of reflective iron. Figure 5.4 depicts four reflectance and corresponding hull-normalized spectra with increasing Fe_d and similar low SOC and $CaCO_3$ contents. The comparison of Fe_d content and the extracted Fe-VIS and Fe-NIR absorption features yielded similar results. An increase of the absorption depths with increasing Fe_d concentration was observed for both absorption bands. Due to the hull-normalization also some samples with low Fe_d concentrations exhibited well developed Fe-VIS absorption bands, but no Fe-NIR absorption feature. In contrast high Fe_d contents were better resolved in the Fe-NIR absorption band.

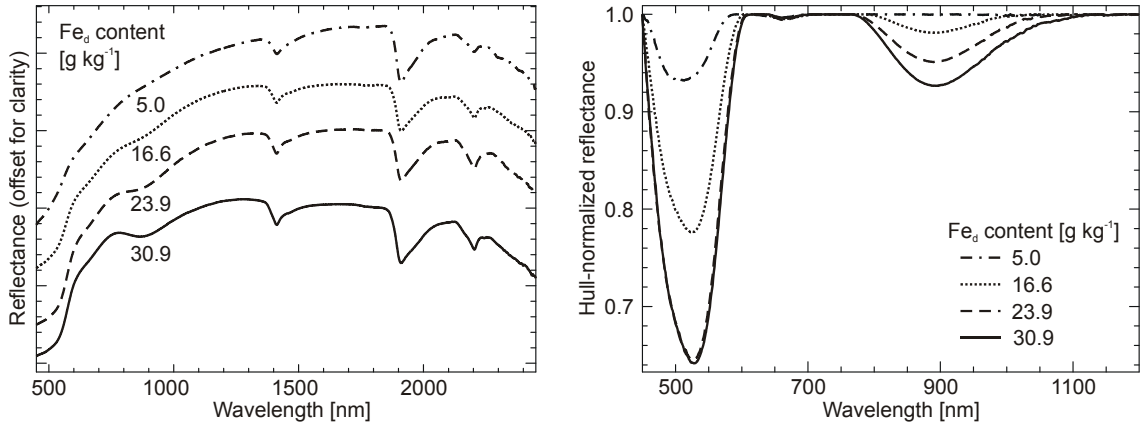

(a) reflectance spectra (b) hull-normalized spectra

Figure 5.4: Influence of different Fe_d contents on iron absorption bands. The reflectance spectra were taken from the homogenized samples with comparable SOC (8.3-13.4 %) and $CaCO_3$ (45-63 %) content.

Strong dependencies were found between the Fe_d content and the normalized absorption depth and area of both the Fe-VIS and the Fe-NIR absorption bands (Figure 5.5). For both absorption bands the relationships were better described by a non-linear power function than a linear fit. This led to significant improvements of the R^2 values of 0.1 on average which represented a 10 % increase of the explained total variation. The non-linear relationship between the Fe_d concentration and the iron absorption intensities can be attributed to multiple reflection of light at the same grain surface (Geerken 1991). A similar non-linear relationship was documented for the carbonate (inorganic carbon) content and the normalized absorption area and depth of its absorption feature near 2345 nm by Jarmer et al. (2009). However for iron, unlike in this study, other researchers reported saturation in the sensitivity of various spectral indices with increasing iron oxide content (Torrent et al. 1983; Ben-Dor et al. 2006). Nevertheless, Fe_d contents exceeding the analyzed range may exhibit intensity saturation of the absorption band.

The non-linear trends for the Fe-VIS and Fe-NIR features were mainly triggered by the soil samples containing less than 15 g kg^{-1} Fe_d that were predominately located below the linear fit. However for higher Fe_d concentrations, both linear and non-linear functions appeared to describe the relationship equally well. The non-linear trend of the Fe-NIR features was considerably more pronounced than of the Fe-VIS. As the additional main driver for the determined non-linear relationship of the Fe-NIR absorption, six samples (encircled in Figure 5.5b and d) were identified which exhibited higher normalized spectral area and depth values than the rest of the samples. In fact, excluding these samples would assimilate the R^2 of the linear (R^2=0.793 for area and 0.800 for depth) and non-linear (R^2=0.798 for

area and 0.831 for depth) trend lines. However, the chemical composition of the samples reflected the variation of all samples with Fe_d ranging from 18.6 to 33.7 g kg^{-1}, SOC from 4.4 to 10 g kg^{-1} and $CaCO_3$ from 28 to 314 g kg^{-1}. Four samples were collected from low to well developed soil surfaces (including Regosols, Luvisols, Cambisols and Calcisols) over volcanic bedrock and partly with calcarenites intercalated, which again covered the entire range of the encountered soil types. The other two samples originated from soils whose surfaces were potentially eroded but they had no particular impact on the correlation. Based on the available data, no explanation was found for the special behavior of these samples. Thus it was assumed that they represented the variability of the soils in the study area and were therefore kept in the data set for subsequent analysis.

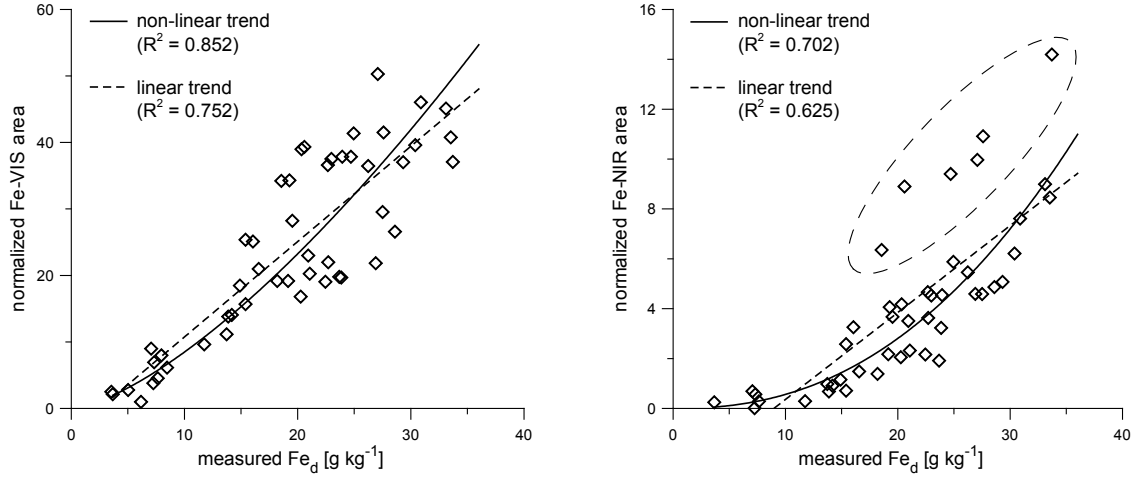

(a) Fe-VIS area

(b) Fe-NIR area

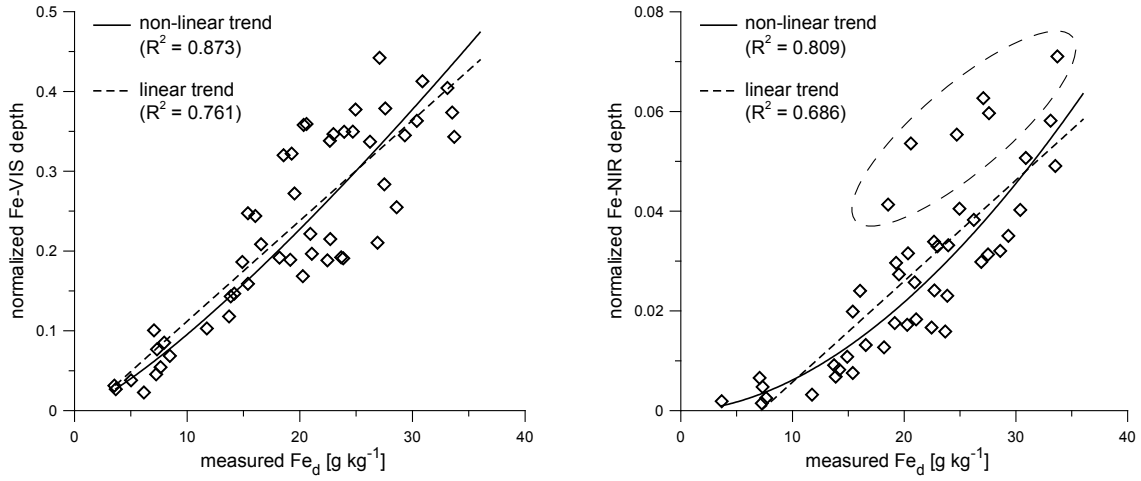

(c) Fe-VIS depth

(d) Fe-NIR depth

Figure 5.5: Relationship between Fe_d content and hull-normalized Fe-VIS and Fe-NIR absorption features.

The relationships between Fe_d content and the hull-normalized left and right area spectral features of the iron absorption bands were comparable to the area spectral features. The Fe-VIS absorption band was of almost symmetric shape thus very similar trend lines were obtained for left and right area features. The Fe-NIR absorption band showed an asymmetric shape with the right absorption area being on average one-third larger than the left (see Figure 5.4). No significant correlation was found between the Fe_d content and the Fe-NIR asymmetry. Jarmer (2005) suspected that asymmetry might be related to changes in the hematite/goethite ratio. Due to the lack of mineralogical analysis for iron oxides no further investigations could be performed.

The Fe_d content and the calculated normalized absorption width showed a non-linear relationship for the Fe-VIS and an improved linear one for the Fe-NIR absorption band (Figure 5.6). The width of the Fe-VIS absorption band ranged between 160 and 190 nm except for four samples which were main drivers for the non-linear trend. Very low Fe_d concentrations (< 10 g kg^{-1}) and weak absorption intensity caused the narrower absorption width as well as the selected starting wavelength of the hull-normalization. The width of the Fe-NIR absorption band increased from 17 to 432 nm with increasing Fe_d content. Due to other absorption features (e.g. OH^- and molecular water absorption) at longer wavelength, a stagnation of the width increase with further increase of iron concentration was likely to occur. The variations of the Fe-NIR absorption width values for the samples with low Fe_d content had to be attributed to sensor background noise, which biased the determination of absorption band shoulders from the hull-normalized spectra.

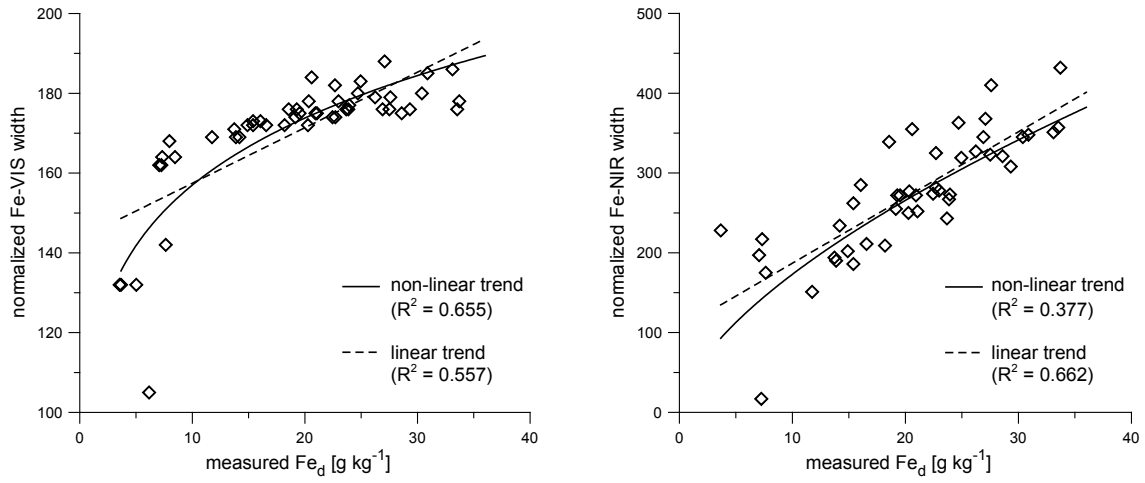

(a) Fe-VIS width (b) Fe-NIR width

Figure 5.6: Relationship between Fe_d content and area and width of Fe-VIS and Fe-NIR absorption band.

5.2.2 Soil organic carbon (SOC)

The SOC had a considerable impact on the reflectance spectra of two soil samples. Both samples (one carbonatic and one volcanic) contained significantly more SOC than the rest of the samples. The high SOC content of 21 g kg^{-1} and 27.9 g kg^{-1} caused a flattening of the VIS/NIR reflectance and decrease of reflectance intensity (Figure 5.7). The iron absorption features were reduced significantly compared to other samples with similar $CaCO_3$ and Fe_d but lower SOC content. Baumgardner et al. (1985) and Ben-Dor (2002) described SOC spectral influence becoming less effective when its concentration dropped below 20 g kg^{-1}. The remaining 48 samples in the data set contained less than 15.2 g kg^{-1} thus a spectral impact of SOC was minimal.

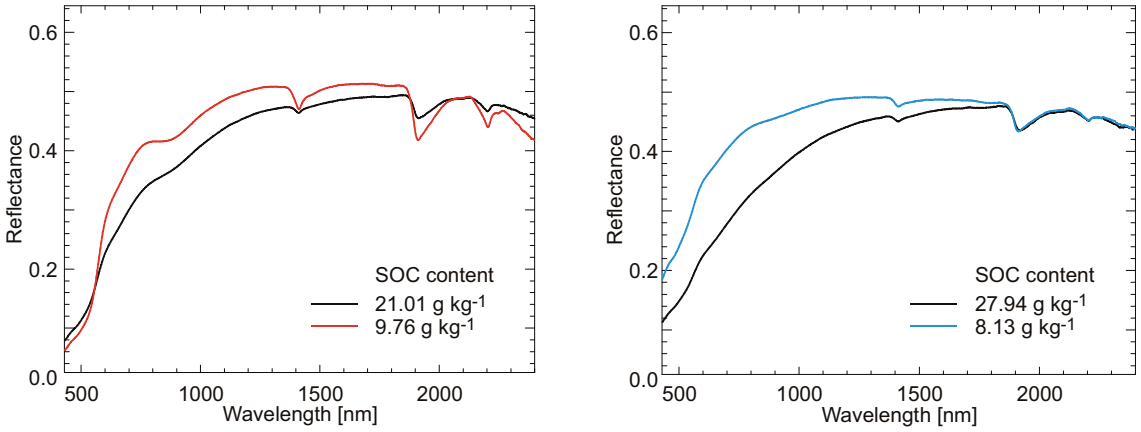

(a) volcanic soils
(Fe_d: 23.7 and 24.9 g kg^{-1}, $CaCO_3 \geq 40$ g kg^{-1})

(b) carbonatic soils
($CaCO_3$: 357 and 227 g kg^{-1}, $Fe_d \geq 8.5$ g kg^{-1})

Figure 5.7: Spectral influence of high SOC concentration on soil reflectance.

5.2.3 Clay mineralogy

Clay minerals have the ability to substitute different cations (e.g. Al^{3+}, Mg^{2+} and $Fe^{2+/3+}$). Beside free iron oxides, Fe-bearing clay minerals can also contribute to the iron absorption bands intensity in the VIS/NIR. However, these iron ions are not dissolved by the dithionite-citrate reagent (Parfitt and Childs 1988), so larger quantities of Fe-bearing clay minerals would affect the subsequent Fe_d modeling. In order to assure that no additional Fe-ions in clay minerals are absorbing, the reflectance spectra of four representative samples - heated to 600° for 8 h as described by Ben-Dor and Banin (1990) - were compared with the original non-heated state (Figure 5.8). Through the heating process, the strong overlapping absorption of water and hydroxyl groups was removed. This led to a

significant reduction of their absorption bands and overall albedo increase in the NIR to SWIR wavelength region. The accompanied enhancement of the clay lattice hydroxyls absorption features revealed a shift of the cation-OH absorption wavelength position, which allowed deduction of the predominant clay cation. The clay-OH absorption band position of the non-heated samples was detected at 2203 nm and of the heated at 2181 nm (Figure 5.8b), which was a strong indication that Al^{3+} was the main substituted cation in the clay minerals. This was also supported by the XRF results of volcanic soils that returned significantly higher Al_2O_3 concentration of 12.5 to 16.0 % compared to Fe_2O_3 (5.2-8.9 %) and MgO (0.5-2.8 %). The symmetric character of the absorption band and the missing of the kaolinite characteristic double absorption feature indicated that Al-bearing smectites such as montmorillonites were prevailing. Additional iron absorption of Fe-bearing clay minerals was ruled out.

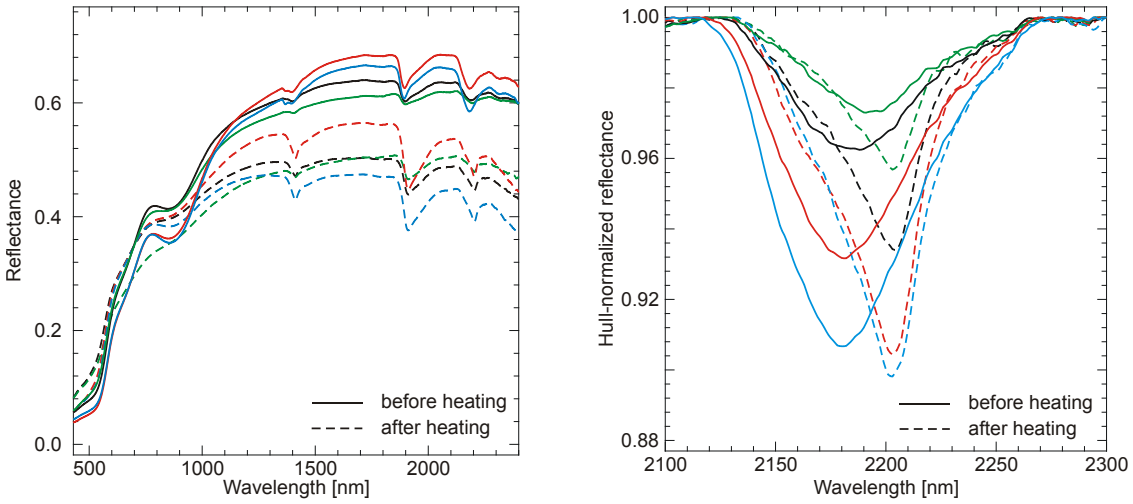

(a) reflectance spectra

(b) hull-normalized cation-OH absorption region

Figure 5.8: Comparison of reflectance and hull-normalized spectra of non-heated and heated soil samples.

5.2.4 Soil texture

The soil texture describes the relative proportion of different grain sizes of mineral particles in a soil, that are classified by the soil's dominating sand, silt, and clay grain size fractions (Birkeland 1999). Grain size differences were reported to influence the shape of spectra (Hunt and Salisbury 1970; Baumgardner et al. 1985; Gaffey 1986; van der Meer 1995), however, these studies investigated predominantly pure minerals whose different grain sizes were obtained by sieving and milling (1 mm to 10 µm). The spectral influence

of grain size (soil texture) on soil reflectance was more difficult to describe, because the aggregation of soil particles is also linked to soil texture effects. In particular, fine-grained samples (clay-dominated) were often highly aggregated and hence showed similar or even more pronounced spectral behavior than coarse-grained soils (sand-dominated). The effects of aggregation were minimized through homogenization of the samples.

The spectra of two soils (homogenized and 2-mm sieved), one sand-dominated and one clay-dominated, with comparable chemical compositions (Fe_d: 23 g kg^{-1}, $CaCO_3$: 7 and 37 g kg^{-1}, SOC: 12 and 15 g kg^{-1}), that were typical of the data set (see Table 5.2) are depicted in Figure 5.9. When comparing the sample reflectance spectra after different processing states (2-mm sieved and homogenized) it appeared that the overall brightness decreased while the absorption depth increased with increasing grain size. This was coherent with the findings of other studies e.g. Hunt and Salisbury (1970), Baumgardner et al. (1985), Gaffey (1986) and van der Meer (1995), who described the same spectral behavior when investigating the influence of different grain sizes on carbonate mineral spectra.

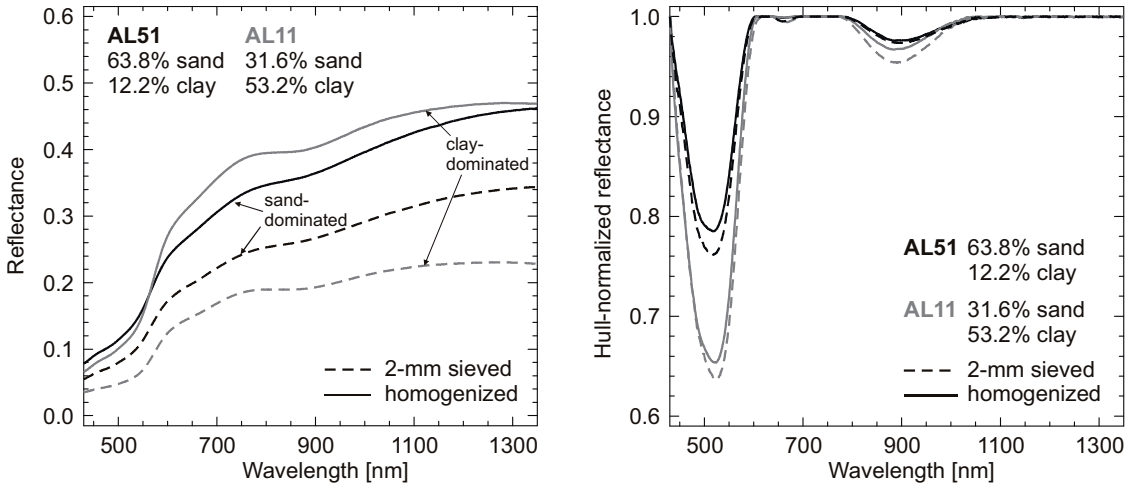

(a) reflectance spectra

(b) hull-normalized spectra

Figure 5.9: VIS/NIR reflectance and hull-normalized spectra of two soil samples (AL51: sand-dominated group, AL11: clay-silt-dominated group) with two different processed grain sizes fractions (2-mm sieved and homogenized).

Spectral comparison of both homogenized samples showed that the clay-dominated sample was brighter than the sand-dominated for wavelengths above 550 nm. For wavelengths below 550 nm the behavior reversed, the albedo of the sand-dominated was higher than the

clay-dominated sample. This effect was attributed to the transopaque nature of ferric ion as described by Hunt et al. (1971). The comparison of both reflectance spectra of the 2-mm sieved samples showed that the sand-dominated one reflected more energy over the whole VIS/NIR than the clay-dominated. This was caused by the aggregation of soil particles in the clay-dominated which resulted in higher surface roughness with more microscopic shadow (Ben-Dor et al. 1999).

The Fe-VIS and Fe-NIR absorption features were more pronounced for the normalized spectra of the homogenized clay-dominated sample than for the sand-dominated one (Figure 5.9b), which contradicted previous observations from literature. This suggested that more iron was optically active in the clay sample even though the citrate-dithionite determined Fe_d content of both samples was identical. In general, the citrate-dithionite treatment dissolves the most common iron oxides, goethite and hematite, very well (Parfitt and Childs 1988). However, Parfitt and Childs (1988) found that large iron oxide crystals (goethite and hematite) may only be partly dissolved in citrate-dithionite and require additional treatments. Only one citrate-dithionite treatment was performed to dissolve the iron in the soil samples used in this study. Thus, the Fe_d content may have been underestimated; the iron absorption bands of those samples would appear much deeper than expected. However, systematic Fe_d underestimation of most fine-grained soil samples was ruled out.

The different spectral response of coarse- and fine-grained samples with the same Fe_d content demonstrated heterogeneity and variability of the soil materials. The optical sensitivity of the iron oxides was described to be not only a function of quantity but also to depend on how iron is bound and distributed in the soil. In addition, multiple light reflection between the individual grains may occur on the sample surfaces (Geerken 1991). Sand grains coated with iron oxides may reflect light with a different intensity than soil aggregates bound by free iron oxide crystals or organic-iron complexes. Hence, separate investigation of the soil texture groups (clay-silt-dominated and sand-dominated samples) seemed appropriate and necessary.

5.3 Modeling pedogenic iron oxide content

5.3.1 Relationships between Fe_d content and spectral iron features

The Fe_d modeling was based on the strong correlations between Fe_d content and the Fe-VIS and Fe-NIR spectral absorption features. Table 5.6 summarizes the coefficients of

determination (R^2) of the Fe_d relationships with selected spectral features for the two soil texture groups and for all samples. Since previous spectral analyses had shown that the correlation of Fe_d content and some spectral features was generally best described by a non-linear function, the coefficients were determined for modeling in linear and natural logarithmic (n-log) data space (see chapter 4.3).

Table 5.6: Coefficient of determination (R^2) for Fe_d content and selected hull-normalized spectral features calculated in linear and n-log transformed data space.

	all samples		**clay-silt-dominated**		**sand-dominated**	
	linear	**n-log**	**linear**	**n-log**	**linear**	**n-log**
Fe-VIS absorption band ~520 nm	**N=50**		**N=24**		**N=26**	
absorption depth	0.761	**0.873**	0.837	0.934	0.878	**0.905**
absorption width	0.557	0.655	0.660	0.863	0.472	0.543
absorption area	0.753	0.852	0.832	0.935	0.870	0.861
absorption area left	0.740	0.846	0.819	0.914	0.870	0.854
absorption area right	0.764	0.847	0.840	**0.938**	0.863	0.853
Fe-NIR absorption band ~890 nm	**N=45**		**N=23**		**N=22**	
absorption depth	0.686	**0.809**	0.674	**0.876**	0.754	**0.900**
absorption width	0.662	0.377	0.607	0.517	0.774	0.514
absorption area	0.625	0.702	0.616	0.846	0.648	0.788
absorption area left	0.640	0.643	0.642	0.851	0.664	0.719
absorption area right	0.610	0.723	0.594	0.839	0.634	0.813

For the entirety of the samples, best correlations were obtained in n-log data space between Fe_d content and the hull-normalized Fe-VIS absorption depth (R^2=0.873) and the Fe-VIS area features (R^2=0.846 to 0.852). A good correlation was also found between Fe_d content and the hull-normalized Fe-NIR absorption depth (R^2=0.809). The lower R^2 for the Fe-NIR depth was attributed to the significant lower absorption intensity of the Fe-NIR absorption band in comparison to the Fe-VIS absorption. The about 12 times deeper Fe-VIS absorption band had a significantly better SNR and much higher variation of the absorption depth values which led to the better correlation. The correlations based on Fe-VIS and Fe-NIR absorption features in linear data space were of moderate (Fe-NIR) to good (Fe-VIS) quality. Also the relationship modeled with the other n-log transformed Fe-NIR features yielded only moderate correlations, except for absorption width.

In general significantly better R^2 were determined for the texture-dependent soil samples groups in n-log data space. The best model for the texture-dependent clay-silt-dominated group of soil samples was developed from the n-log Fe-VIS right absorption area

(R^2=0.938). The distinct improvements of the R^2 for texture-dependent groups were attributed to a more homogenous grain size distribution within the groups. High to very high correlations (R^2= 0.863 to 0.938) were obtained for the other Fe-VIS spectral features of the clay-silt-dominated group in n-log data space. The same held true for sand-dominated samples for both linear and n-log data space (R^2=0.853 to 0.905), except for absorption width. The best Fe-NIR models for both texture-dependent groups were developed on the basis of the n-log Fe-NIR absorption depth (R^2=0.876 and 0.900). Also the models developed based on Fe-NIR absorption area features (total area, left and right area) for clay-silt-dominated samples yielded very good correlations in n-log data space (R^2=0.839 to 0.851).

The prediction modeling was carried out including only one predictor variable (hull-normalized absorption depth). Tests including two or more predictor variables in the modeling from either Fe-VIS, Fe-NIR or redness indices as used by other authors e.g. Ben-Dor et al. (2006) for predicting the iron oxide content, did not improve the model performance significantly due to the spectral feature's interdependence and the direct relationship between color indices and VIS/NIR reflectance. Figure 5.10 depicts the relationships of Fe_d content and hull-normalized Fe-VIS and Fe-NIR absorption depths - the predictor variable used in the subsequent modeling. In both plots the absorption depth of the coarser sand-dominated samples was in general lower than of the clay-silt-dominated ones which matched the findings from chapter 5.2.

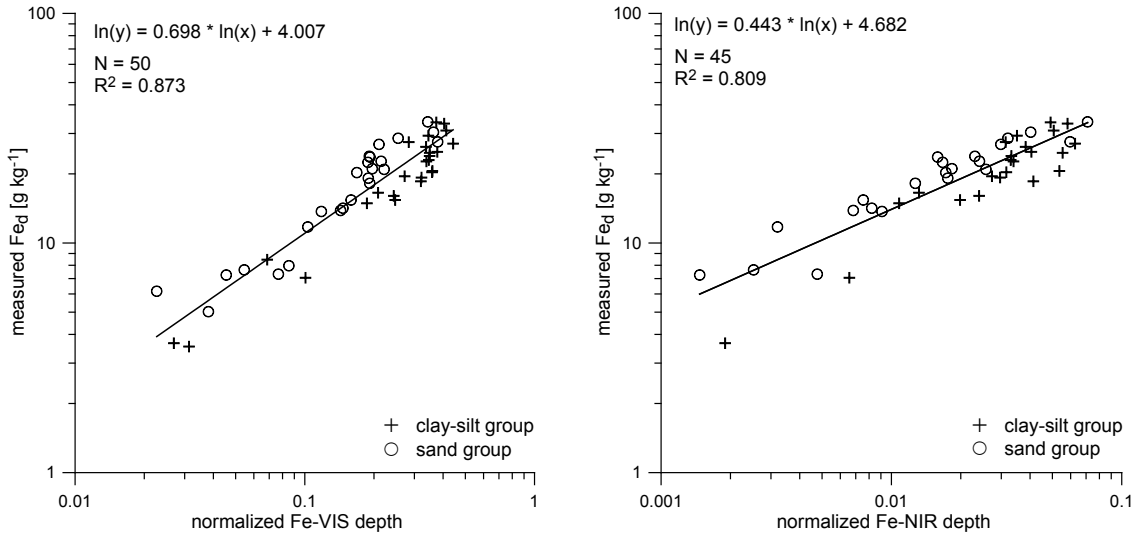

(a) Fe-VIS (b) Fe-NIR

Figure 5.10: Relationships between Fe_d and hull-normalized Fe-VIS and Fe-NIR depth in logarithmic data space.

5.3.2 Texture-dependent models

The best estimates from the Fe-NIR absorption were obtained in the cross-validated dataset for the sand-dominated texture group (R^2_v=0.875, $RMSE_v$=2.72, rel. $RMSE_v$=13.91 %, RPD_v=2.89) based on the hull-normalized absorption depth in n-log data space:

$$\ln (Fe_d\ [g\ kg^{-1}]) = 0.431 * \ln (\text{Fe-NIR depth}) + 4.737. \quad 5\text{-}1$$

The RPD_v of 2.89 indicated an excellent analytical efficiency of calibrations according to the scale of Dunn et al. (2002). Figure 5.11a shows the scatter plot of the cross-validated results. The regression line was close to the 1-to-1 line with best predictions possible between 10-30 g kg^{-1} Fe_d. The model tended to underestimate low Fe_d (model offset of 2 g kg^{-1}) and overestimated high Fe_d contents slightly. One sample with high Fe_d concentration (indicated in Figure 5.11a) was clearly overestimated and affected the deviation of the model from the 1-to-1 line. This sample came from an eroded soil surface (lower B-horizon), reflecting different soil conditions than the normal non-eroded soil surfaces. Excluding this sample from the modeling yielded a significant improvement of model performance (R^2_v=0.909, $RMSE_v$=2.20) and a regression line that was closer to 1-to-1 line. However, the sample could not be identified as a statistical outlier, so it was kept in the further analysis.

The estimates of Fe_d for the clay-silt-dominated group based on the normalized Fe-NIR absorption depth in n-log data space were of good quality (R^2_v=0.695; $RMSE_v$=4.13, rel. $RMSE_v$=19.04 %, RPD_v=1.72). The associated model was obtained as follows:

$$\ln (Fe_d\ [g\ kg^{-1}]) = 0.\ 581 * \ln (\text{Fe-NIR depth}) + 5.070. \quad 5\text{-}2$$

The scatter plot of the clay-silt model is depicted in Figure 5.11b. The regression line between measured and predicted Fe_d was only a little worse than the sand model, also leading to slight underestimation and overestimation of low and high Fe_d contents, respectively. The estimation of medium Fe_d quantities between 15-30 g kg^{-1} yielded more scattered results around the 1-to-1 line. This was attributed to the higher texture variability within the group, which consisted of a mixture of mainly clay and a few silt-dominated samples compared to the sand-dominated fraction of the other group (Table 5.3). This clearly reduced the performance of the model (R^2_v=0.695, $RMSE_v$=4.13) and caused the significant increase to 19.04 % of rel. $RMSE_v$.

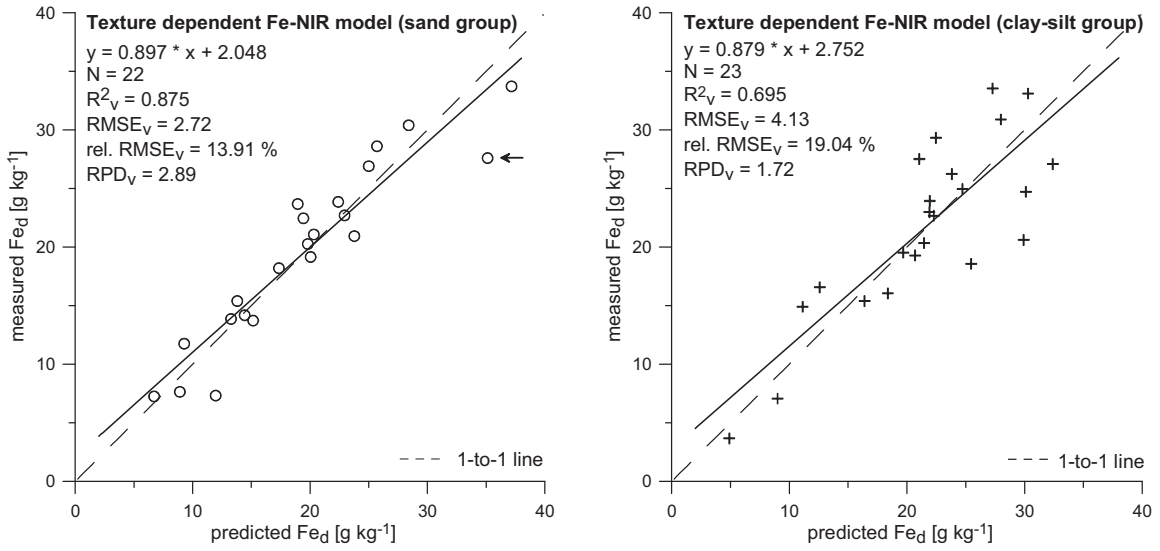

(a) Sand-dominated soil texture group (b) clay-silt-dominated soil texture group

Figure 5.11: Cross-validated results of texture dependent Fe_d prediction models based on Fe-NIR absorption depth. (Model's residuals (n-log transformed Fe_d concentrations) were normally distributed and not auto-correlated. The residuals mean is not significantly different from zero.)

When comparing both models it was found that stable and comparable models can be obtained on the basis of the same input variable (n-log transformed, hull-normalized Fe-NIR absorption depth). The soil texture appeared to have a certain influence on the prediction accuracy. The suitability of the models was tested by experimental application of each texture-dependent model to the other texture group, which obtained constant Fe_d over- and underestimation for the clay-silt- and sand-dominated samples, respectively.

The best estimates from the Fe-VIS absorption were obtained in the cross-validated dataset for the sand-dominated texture group (R^2_v=0.878, $RMSE_v$=2.86, rel. $RMSE_v$=15.89 %, RPD_v=2.69) using the hull-normalized absorption depth in n-log data space:

$$\ln (Fe_d\ [g\ kg^{-1}]) = 0.\ 739 * \ln (\text{Fe-VIS depth}) + 4.208. \qquad 5\text{-}3$$

Although initially a higher correlation was determined for the hull-normalized Fe-VIS spectral right area feature, the absorption depth was chosen as predictor variable for the modeling to allow the direct comparison to the Fe-NIR model. The performance of this model was almost identical with the corresponding prediction model developed from Fe-NIR depth. The slightly poorer $RMSE_v$ of 2.86 and rel. $RMSE_v$ of 15.89 % reflected the higher scatter of the Fe-VIS results in comparison to the Fe-NIR model for sand samples.

The Fe-VIS depth model for the clay-silt-dominated samples, however, yielded significantly better estimates than the corresponding Fe-NIR depth model (R^2_v=0.813; $RMSE_v$=3.59, rel. $RMSE_v$=17.57 %, RPD_v=2.02):

$$\ln (Fe_d\ [g\ kg^{-1}]) = 0.771 * \ln (\text{Fe-VIS depth}) + 3.994. \quad 5\text{-}4$$

The scatter plot of the cross-validated results for both Fe-VIS absorption depth models are shown in Figure 5.12. The regression lines of both plots were almost identical to the 1-to-1 line and, in contrast to the Fe-NIR models, did not show the trend of under- or overestimation of certain Fe_d concentration ranges. The RPD of 2.69 and 2.02 indicated an excellent analytical efficiency of calibrations according to the scale of Dunn et al. (2002).

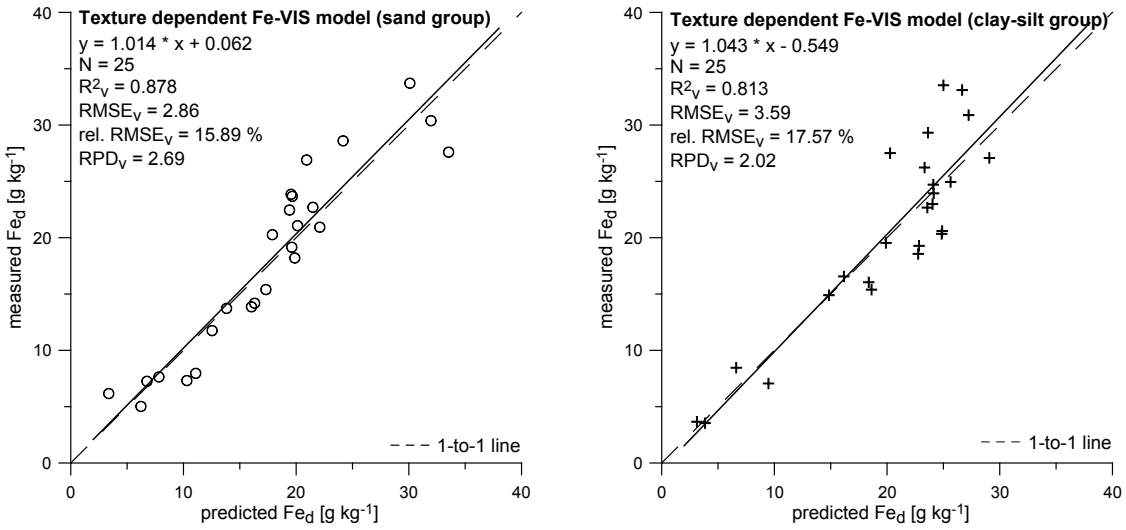

(a) sand-dominated soil texture group (b) clay-silt-dominated soil texture group

Figure 5.12: Cross-validated results of texture dependent Fe_d prediction models based on Fe-VIS absorption depth. (Model's residuals (n-log transformed Fe_d concentrations) were normal distributed and not auto-correlated. The residuals mean is not significantly different from zero.)

Both Fe_d prediction models developed for the sand-dominated samples showed a better performance than the models for clay-silt-dominated samples. Further the models based on n-log transformed Fe-NIR absorption depth showed large performance differences between the sand-dominated and clay-silt-dominated soil texture group which were attributed to the high texture variability. Both Fe-VIS models had very similar performance. The texture variability of the clay-silt-dominated samples appeared to have a stronger spectral impact on the Fe-NIR than the Fe-VIS absorption band and subsequently on the Fe_d prediction

accuracy. This could be attributed to the fact that the hull-normalized Fe-NIR absorption was on average 12 times less intensive than the corresponding Fe-VIS absorption. Variations in the soil samples hematite/goethite ratio might be a potential cause of higher texture variability of the fine-grained soil which could not be investigated further due to the lack of analytic data.

5.3.3 Texture-independent models

To enable the Fe_d prediction of samples with unknown texture, a texture-independent model was developed. This avoids costly and time-consuming laboratory grain size analysis as prerequisite to choose the appropriate texture-dependent model and subsequently facilitates the application to hyperspectral image data. The development of the texture-independent Fe_d prediction models was based on the same input parameter (Fe-VIS absorption depth and n-log transformed Fe-NIR absorption depth) as the respective texture-dependent models. Good estimates were obtained for the n-log transformed Fe-NIR model (R^2_v=0.755, $RMSE_v$=3.74, rel. $RMSE_v$=18.11 %, RPD_v=1.93) which was comparable to the according clay-silt Fe-NIR model:

$$\ln (Fe_d\ [g\ kg^{-1}]) = 0.443 * \ln (\text{Fe-NIR depth}) + 4.682. \quad 5\text{-}5$$

Despite of the very good performance of both texture-dependent models based on Fe-VIS absorption depth, the texture-independent model yielded clearly lower estimates (R^2_v=0.772, $RMSE_v$=3.98, rel. $RMSE_v$=20.74 %, RPD_v=1.94):

$$\ln (Fe_d\ [g\ kg^{-1}]) = 0.698 * \ln (\text{Fe-VIS depth}) + 4.007. \quad 5\text{-}6$$

In comparison to the texture-independent Fe-NIR model, the R^2_v of the Fe-VIS model was slightly better, while $RMSE_v$ and rel. $RMSE_v$ were clearly worse indicating a higher variance of the models results. Figure 5.13 shows the scatter plots of both texture-independent models with different symbols for sand-dominated and clay-silt-dominated samples. As the spectroscopic analysis showed, there was a general trend of lower absorption depth for sand samples compared to clay-silt samples with the same Fe_d content. This trend also showed up in scatter plots, in which the sand-dominated samples were mostly underestimated by both texture-independent models independent of their Fe_d content. The Fe_d concentrations of clay-silt-dominated samples were overestimated by both

texture-independent models when below 25 g kg^{-1} and underestimated when above 25 g kg^{-1}.

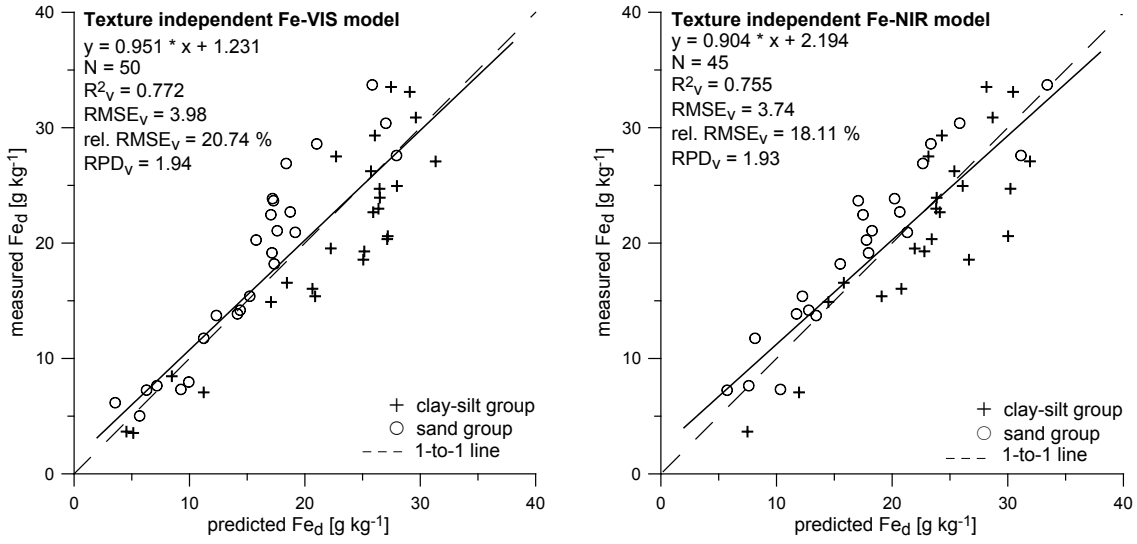

(a) Fe-VIS absorption depth (linear space) (b) Fe-NIR absorption depth (n-log space)

Figure 5.13: Cross-validated results of texture independent Fe_d prediction models. (Model's residuals were normal distributed and not auto-correlated. The residuals mean is not significantly different from zero.)

The estimates of low Fe_d contents were limited by the detectability of the iron absorption bands. Especially, weakly developed Fe-NIR absorption bands were affected by the instrument's background noise. For this reason, five samples with Fe_d below 10 g kg^{-1} were excluded prior to modeling, whereas five other samples with Fe_d below 10 g kg^{-1} exhibited a clear Fe-NIR absorption band and were used for modeling subsequently. With higher Fe_d contents, the absorption bands intensified and allowed more stable estimations. Still, the Fe-NIR model explained about 76 % of the data total variation independent of texture. The texture-independent Fe-VIS model, in contrast, explained 78 % of variation in the data. The relatively high RPD_v of 1.93 and 1.94 for both models indicated a good efficiency of the used Fe-VIS and Fe-NIR absorption depth parameters for the calibration. Hence, both texture-independent models were suitable for the Fe_d prediction from samples with unknown soil texture and were considered for the subsequent hyperspectral image analysis.

5.4 Vegetation influence on Fe_d modeling

Vegetation, i.e. plants and their residues, is one of the main parameter affecting directly the recording of soil reflectance signals. Before laboratory-developed Fe_d prediction models

were applied to image data, the influence of partial vegetation cover on the model performance was investigated. From the spectrometric perspective there are two main physiological stages of vegetation which both show very unique spectral characteristics (see chapter 2.3), green photosynthetic active vegetation (PV) and dry/senescent non-photosynthetic active vegetation (NPV). At stages in between pure PV and NPV occurrence, absorption characteristics from either one or both main stages are present. Depending on the relative cover of plants on the soil surface, the soil and vegetation-related absorption features interfere with each other, e.g. both Fe-VIS and chlorophyll bands have their absorption maximum in the blue wavelength region (~520 nm and ~500 nm, respectively). The spectral interactions between vegetation and soil were subject of numerous studies which mostly examined the impact of the soil background on vegetation reflectance, plant canopy (Huete et al. 1985; Huete 1987), and vegetation indices (Nagler et al. 2000; Nagler et al. 2003; Serbin et al. 2008). The opposite case of investigating the vegetation influence on the mapping and prediction of soil properties had rarely been examined (Murphy and Wadge 1994; Richter et al. 2006).

5.4.1 Leaf cover experiment

For better understanding on how and to which extent vegetation affects the iron absorption features, the reflectance of an iron-rich soil of the study area was measured with increasing leaf cover (leaf cover) of PV, NPV and a mixture of both (MIX) under controlled laboratory conditions. The specific soil sample was selected because its chemical composition (Fe_d=27.6 g kg^{-1}, SOC=7.6 g kg^{-1} and $CaCO_3$=125 g kg^{-1}) was representative for all samples. The MIX leaf cover consisted of one-third PV and two-thirds NPV leaves on average. After the spectra pre-processing, the spectral features of Fe-VIS, Fe-NIR, chlorophyll (~500 nm), plant water (~970 nm) and cellulose-lignin (~2100 nm) absorption bands were extracted automatically according to the wavelength range given in Table 4.4.

The VIS/NIR reflectance spectra for the three leaf cover measuring series are depicted in Figure 5.14. The albedo in the VIS wavelength region of the soil-PV spectra decreased with increasing PV leaf cover due to intensification of chlorophyll absorption. NPV leaf cover caused an increase of the soil's VIS reflectance due to the lack of absorbing features in this wavelength region. The series with MIX leaf cover showed only a slight increase of the albedo in the VIS region due to partial chlorophyll absorption. In all three series, an albedo increase of the NIR reflectance with increasing leaf cover was observed as e.g. described by Huete et al. (1985). Plant water absorption bands at 970 nm and 1170 nm

were clearly developed in the PV measurements for higher leaf cover. A weak plant water absorption band also appeared at 1170 nm in the spectra of high NPV leaf cover and the MIX leaf cover series.

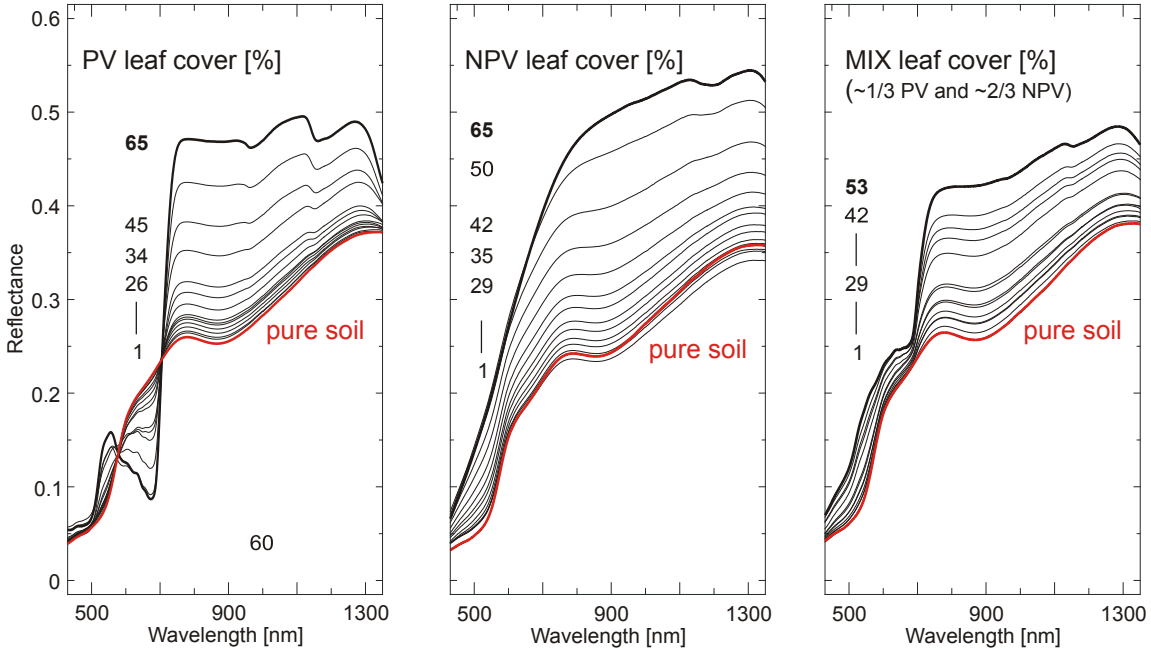

(a) PV leaf cover (b) NPV leaf cover (c) MIX (PV&NPV) leaf cover

Figure 5.14: VIS/NIR reflectance spectra of leaf cover experiments with increasing dry (NPV), green (PV) and mixed (MIX) leaf cover.

In the reflectance spectra of the PV and MIX leaf cover experiments, the Fe-NIR absorption was noticeable as a concave shape of the characteristic vegetation NIR plateau at higher leaf cover (Figure 5.14). Most likely, this was caused by transmission of soil reflectance through the leaves that was recorded in additional to the directly reflected fractional soil signal. The usage of one horizontal leaf layer on the soil surface in the experimental setup supported the transmittance and thus intensified the proportion of soil reflectance in the measured spectra. Variable transmittance properties of plant components as well as multiple reflectance and scattering processes between the leaves and soil surface layer made it difficult to estimate and remove the transmittance fraction from the spectra. The attempt with single transmittance layer calculations could not be performed successfully. Although transmittance effects could not be corrected, it was here assumed that the experiment results were representative for the influence of variable leaf cover on soil reflectance.

5.4.2 Impact on Fe-VIS absorption

In general, iron absorption bands decreased with increasing leaf cover while chlorophyll and plant water absorption increased. Figure 5.15a-c depicts the relationships between leaf cover and hull-normalized Fe-VIS absorption depth (◇) and wavelength position (×) for each leaf cover experiment. In between 0 and ~10 % PV leaf cover the Fe-VIS absorption depth decreased slightly. When exceeding 10 % PV leaf cover, chlorophyll absorption (~430 - 450 nm) overlapped the Fe-VIS absorption band (~480 - 530 nm) and caused an intensification of absorption in this wavelength region. This was accompanied by the Fe-VIS absorption maximum shifting from 520 nm towards shorter wavelengths near 490 nm (see Figure 5.15a). By then iron and chlorophyll were forming a joint absorption region which did not allow determining the individual contribution of the iron-induced absorption. Already at 25 % PV leaf cover, both chlorophyll absorption features were clearly detectable and the green peak was developed (Figure 5.16a). At this point the Fe-VIS absorption was totally masked by the chlorophyll response.

A different spectral behavior was found for NPV leaf cover on the soil due to the lack of absorbing leaf pigments. With increasing NPV leaf cover, a flattening of the reflectance spectra in the VIS region and a corresponding reduction of the Fe-VIS absorption band (Figure 5.15b) was observed. The Fe-VIS absorption maximum position was stable until ~45 % NPV leaf cover was reached. With further increasing leaf cover, the wavelength position shifted towards 500 nm and absorption depth reached a minimum.

The MIX leaf cover experiment showed characteristics of both PV and NPV cover. Dominating chlorophyll absorptions as seen in the pure PV leaf cover experiment were not present in the VIS reflectance spectrum because of the simultaneous occurrence of NPV-induced reflectance increase for higher MIX leaf cover in this wavelength region. Compared to the PV leaf cover experiment, no intensification of the absorption in the VIS region was observed. The Fe-VIS absorption depth decrease was less strong in the PV than in the NPV leaf cover experiment due to low portion of accompanying chlorophyll absorption. When MIX leaf cover reaches 35 - 40 %, the red edge feature became visible in the reflectance spectra due to chlorophyll absorption (Figure 5.14c). This also caused the extracted Fe-VIS absorption wavelength position to shift below 500 nm (Figure 5.15c). The continuous shift of the wavelength position towards shorter wavelengths made it particularly difficult to accurately estimate the iron-induced absorption fraction and consequently predict the Fe_d content for low MIX leaf cover.

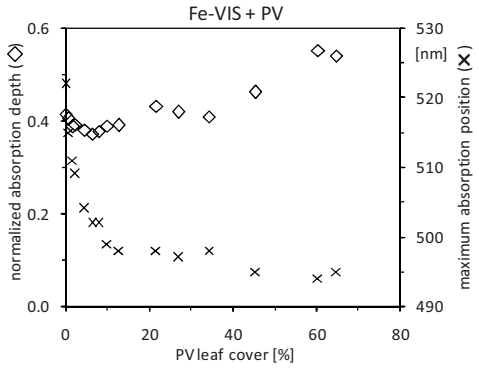

(a) Fe-VIS vs. PV

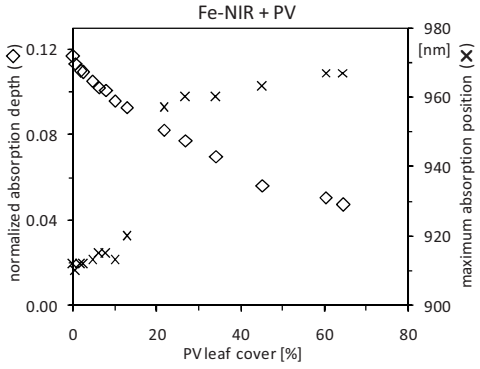

(d) Fe-NIR vs. PV

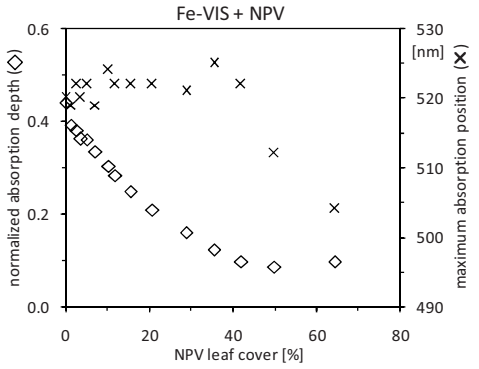

(b) Fe-VIS vs. NPV

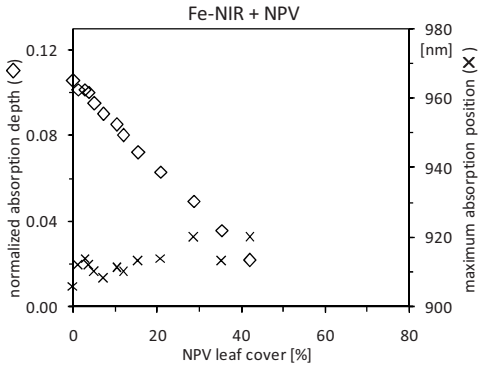

(e) Fe-NIR vs. NPV

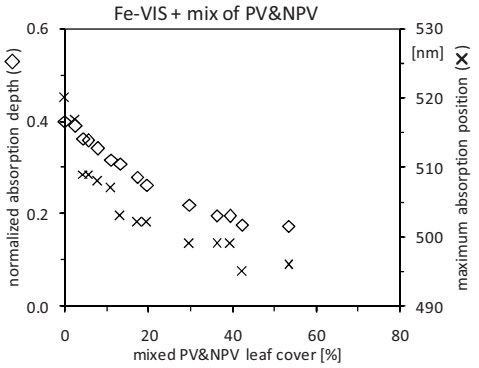

(c) Fe-VIS vs. MIX

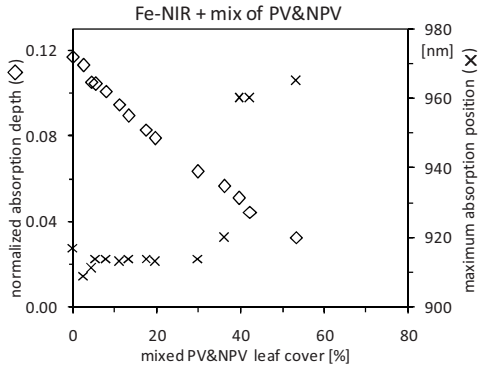

(f) Fe-NIR vs. MIX

Figure 5.15: Relationships between normalized Fe-VIS and Fe-NIR absorption depths and wavelength position and leaf cover (PV, NPV, MIX). The normalized absorptions depth is illustrated by diamonds (left y-axis) and the positions of maximum absorption shown by crosses (right y-axis).

5.4.3 Impact on Fe-NIR absorption

The relationships between leaf cover and normalized Fe-NIR absorption depth (◇) and wavelength position (×) for each leaf cover experiment are depicted in Figure 5.15d-f. In

general, the Fe-NIR absorption decreased with increasing leaf cover independent of the plants physiological stage. With increasing PV leaf cover, the plant water absorptions at 970 nm and 1170 nm overlapped with the Fe-NIR band. The wavelength position of the Fe-NIR absorption maximum shifted abruptly from 910 nm to the 960 nm plant water position when PV leaf cover exceeded 20 %. From there on plant water absorption dominated increasingly the Fe-NIR absorption region for wavelengths larger than 920 nm (Figure 5.16b). The Fe-NIR absorption region between 760 and 920 nm appeared to be unaffected by the plant water absorption showing only a continuous decrease of absorption intensity. For PV leaf cover above 15 %, the 1170 nm plant water absorption dominated the right shoulder of the Fe-NIR absorption (Figure 5.16b).

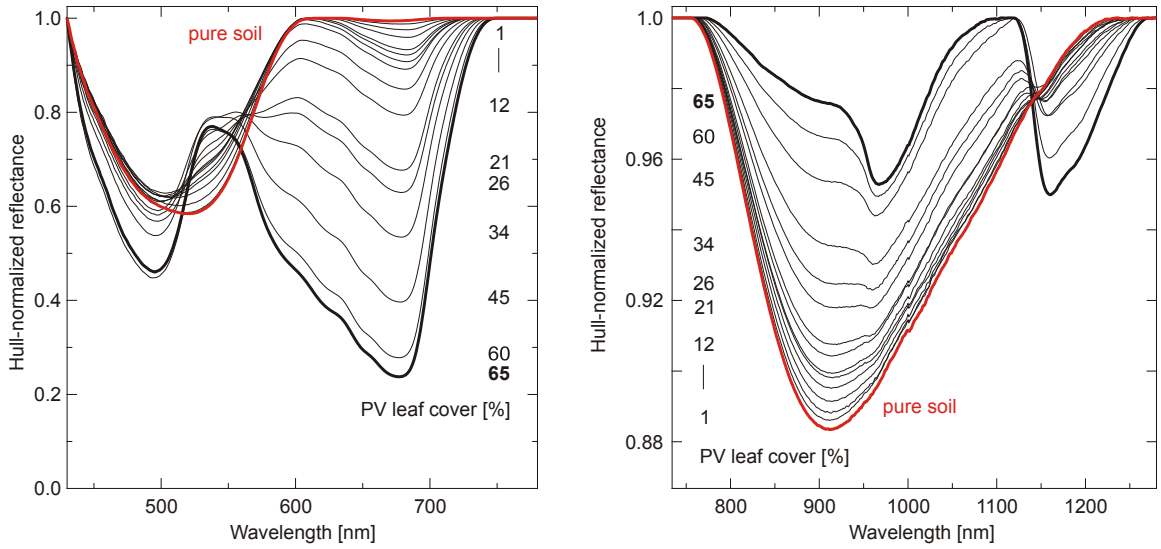

(a) Fe-VIS absorption region

(b) Fe-NIR absorption region

Figure 5.16: Spectral impact of increasing PV cover on hull-normalized iron absorption bands.

The Fe-NIR absorption depth decreased also continuously during the NPV leaf cover experiment (Figure 5.15e). Due to the absence of 970 nm plant water absorption (see Figure 5.14b), no shift of the absorption wavelength position occurred. A noticeable absorption band of the remaining bound plant water developed at 1170 nm when NPV leaf cover exceeded 40 % which however had no impact on the Fe-NIR absorption. The Fe-NIR wavelength position showed a higher variation above 30 % leaf cover that was attributed to very low Fe-NIR absorption intensity approaching the level of sensor background noise.

At 40 % MIX leaf cover, the wavelength position of Fe-NIR absorption maximum shifted to 960 nm indicating the presence of plant water as in the PV leaf cover experiment (Figure 5.15f). The Fe-NIR absorption band depth decreased continuously in the mixed leaf cover experiment as expected from the PV and NPV measurements. The 1170 nm plant water absorption appeared at the right shoulder of Fe-NIR absorption when reaching 30 % MIX leaf cover (see Figure 5.14c) but did not dominate.

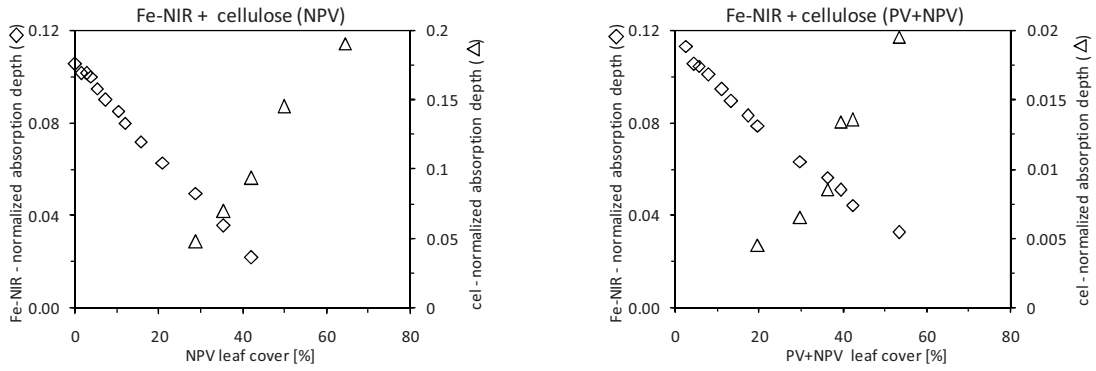

(a) NPV leaf cover (b) MIX leaf cover

Figure 5.17: Relationships between leaf cover (x-axis) and normalized Fe-NIR absorption depth (illustrated by diamonds – left y-axis) and cellulose absorption depth (illustrated by triangle – right y-axis).

For both experiments containing NPV leaf material, the cellulose absorption was initially determined for leaf cover of ~20 % which further intensified as with increasing leaf cover (Figure 5.17). The cellulose absorption depth for the MIX leaf cover experiment was about 10 times lower than for the NPV leaf material. However, it appeared at the same leaf cover stage as the PV induced 970-nm plant water absorption began dominating the Fe-NIR and caused the automatically detected wavelength position to shift from Fe-NIR to plant water maximum absorption. Hence, the shift from the Fe-NIR to 970-nm plant water absorption wavelength position appeared to be a good direct indicator of the PV impact on the soil reflectance. The onset of the cellulose-lignin absorption at 2100 nm was a suitable indirect indicator for the impact of NPV. Both indicators marked a significant vegetation influence on the soil spectral feature detectability when exceeding 20 % leaf cover.

5.4.4 Impact on Fe_d prediction accuracy

The normalized Fe-VIS and Fe-NIR absorption depths were directly related to the Fe_d content in the previous chapter. Based on the above described experiment, the continuous iron absorption depths decrease with increasing leaf cover were expected to cause an underestimation of the Fe_d concentration and thus an increasing uncertainty in Fe_d prediction. Both the Fe-VIS and the Fe-NIR texture-independent model were applied to the experiments spectral measurements to evaluate the vegetation-related Fe_d prediction uncertainty dependent on the leaf coverage. For the pure soil surface without leaf cover a Fe_d prediction uncertainty of zero was assumed in Figure 5.18. With increasing leaf cover, the prediction uncertainty was given as the relative Fe_d underestimation by the model.

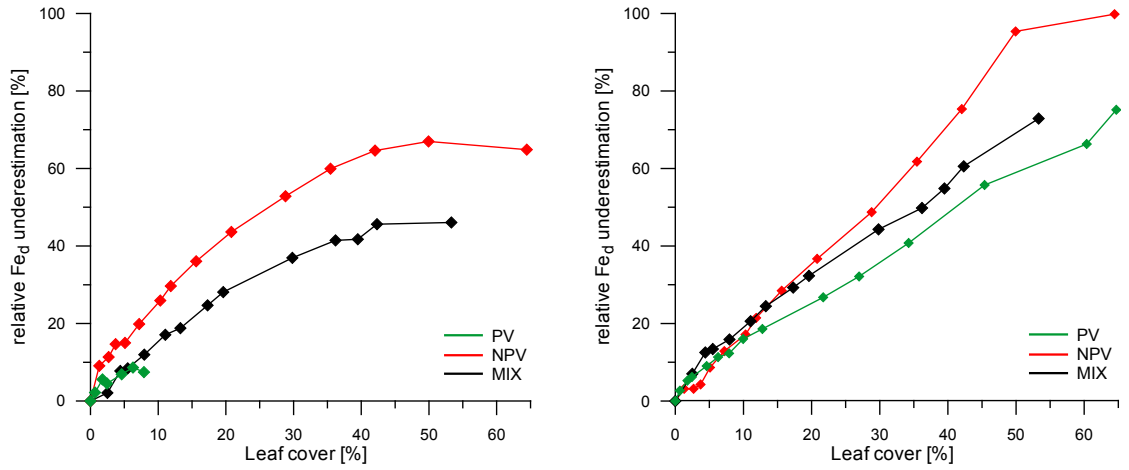

(a) Fe-VIS absorption based model

(b) Fe-NIR absorption based model

Figure 5.18: Potential underestimation of Fe_d concentration for partial leaf cover on soil surface (Fe-VIS and Fe-NIR texture-independent models). The soil samples contained 27.6 g kg^{-1} Fe_d.

For the experiments with PV leaf cover, the Fe_d concentration was only predicted from Fe-VIS absorption depth until the shifted wavelength position reached the 500 nm wavelength position. This was done to ensure a minimal overlapping influence of chlorophyll absorption. It allowed Fe_d prediction until 8 % PV leaf cover and until 20 % MIX leaf cover. For the NPV leaf cover, the Fe_d content could be determined throughout the experiment but with increasing uncertainty. For 10 % NPV leaf cover, Fe_d content was underestimated by about 20 % (~6 g kg^{-1}) which was significantly higher than the models RMSE (~4 g kg^{-1}). The Fe_d underestimation was expected to increase to about 40 % or 10 g kg^{-1} when NPV leaf cover reached 20 %. At 40 % NPV leaf cover, a stagnation of the prediction uncertainty increase rate was observed.

For the Fe-NIR absorption region, the Fe_d content was predicted based on the normalized Fe-NIR absorption depth of the 912 nm waveband. This usage of single wavebands absorption depth appeared more appropriate than the automatically extracted absorption depths because for about 20 % PV and 40 % MIX leaf cover plant water-induced absorption depths were determined instead of Fe-NIR which was indicated by the shift of detectable maximum absorption position from 910 to 970 nm. The Fe-NIR absorption range between 760 and 920 nm, however, seemed not to be affected by plant water absorption directly (Figure 5.16b). In the optimal case, the position of the Fe-NIR absorption maximum would be chosen for the Fe_d modeling, here determined at 912 nm wavelength.

When employing the Fe-NIR model, the Fe_d content was continuously underestimated with increasing leaf cover just as for the Fe-VIS model. For 10 % leaf cover (independent if PV, NPV or MIX), a Fe_d underestimation by 17 % or 3 to 4 g kg^{-1} was found which equaled the models RMSE. Additional 2 to 3 g kg^{-1} Fe_d content equal to ~30 % was underestimated when reaching 20 % leaf cover. Fe_d predictions from soil surface with PV and MIX leaf cover yielded significantly lower Fe_d underestimations at higher leaf coverage, most probably because of transmittance effects. The Fe_d content was predicted with satisfactorily until about 20 % leaf cover, when plant water absorption overlapped the Fe-NIR absorption. The Fe_d content was determined with much lower accuracy for higher leaf cover.

The Fe-NIR model allowed reliable Fe_d predictions also for higher leaf covers and all three vitality states. The detectability of the Fe-VIS absorption band from partly vegetated soil surfaces depended largely on the fraction of photosynthetically active vegetation. Due to dominating chlorophyll absorption, the determination of Fe-induced absorption was difficult for higher leaf cover. In contrary, the Fe-NIR absorption band was partly unaffected by overlapping plant water absorption. When using the normalized absorption depth of a single wavelength from the unaffected left Fe-NIR absorption shoulder, a differentiation of the Fe-induced and plant water-induced absorption fraction was still possible even for higher leaf cover. In order to keep the vegetation influence on Fe_d prediction accuracy as low as possible, the subsequent mapping of Fe_d spatial distribution from hyperspectral image data was based on the Fe-NIR absorption band.

Chapter 6: **Mapping pedogenic iron oxide from hyperspectral image data**

The models presented in chapter 5.3 to predict the pedogenic iron oxide content were developed on the basis of spectral reflectance measurements taken under ideal laboratory conditions. The transferability of these regression models to image data is limited for several reasons such as the characteristics of the sensors, atmospheric influences, and different scales of measurements (homogenization and mixing of various surface materials). Vegetation coverage and soil texture are the main natural surface parameter affecting the pedogenic iron oxide quantification from image data. Their impact was evaluated in independent laboratory studies (see previous chapter). Due to these limitations only a few studies succeeded in the direct application of laboratory models to remote sensing image data (e.g. Palacios-Orueta et al. 1999; Hill and Schütt 2000; Jarmer 2005). In most cases the laboratory models were recalibrated to be applied to the image data (e.g. Ben-Dor et al. 2006). Prediction modeling was also performed directly on the image without previous laboratory spectral investigations (e.g. Selige et al. 2006).

6.1 Spectral absorption features extraction

Soil and vegetation-related spectral absorption features were extracted from the HyMap image data using the same way and parameters as described for the laboratory spectra (see chapter 4.3). First, the hull-normalization was calculated for the image to allow the accurate determination of absorption position and depth. Due to the two strong atmospheric water absorption regions near 1450 and 1900 nm, hull-normalization was performed separately for VIS/NIR region between 436 to 1300 nm and for SWIR region between 2000 to 2400 nm. The SWIR wavelength region between 1500 and 1750 nm was not considered because it contained no diagnostic soil and vegetation absorptions of interest. The parameters for the automatic spectral absorption feature extraction are

summarized in Table 4.4. The soil absorption features comprised the Fe-NIR and C-O carbonate absorption (~2340 nm) bands. The C-O absorption was mapped in the study area as additional pedogenic parameter and indicator for geological background since it was known that a main geological boundary between iron-rich and carbonate-rich surface rocks/soils dominated the landscapes in the northern study area (see Figure 3.2). Fe-VIS absorption features were not extracted because they cannot be differentiated from overlapping chlorophyll absorption (see chapter 5.4). Vegetation absorption features (chlorophyll at ~660 nm and cellulose at ~2100 nm) were extracted for evaluating the accuracy of Fe_d prediction according to the findings of chapter 5.4.

The spectral feature extraction from the image was performed pixel-wise and output a map for each spectral feature containing the extracted values. The value 0 was assigned to pixel with no extractable absorption. The spectral feature maps were evaluated using the maps for absorption position and width in order to verify whether the entire absorption band or noise-induced features were extracted. The Fe-NIR absorption band was determined for 37 % of the pixels with the maximum absorption position ranging between 861 to 943 nm and absorption width between 141 and 488 nm. The absorption widths fitted well with the range determined of the laboratory spectra, whereas the absorption position interval exceeded the laboratory wavelength range (877 to 933 nm). However all pixels exhibited Fe-NIR absorption maxima within the wavelength ranges that were reported for the common iron oxides hematite and goethite (compare to Table 5.4). Consequently, all were used for the subsequent analysis.

According to the carbonate-rich soil laboratory spectra, the typical width for the carbonate C-O absorption was found between 90 and 120 nm. Pixel spectra with narrower C-O absorption bands were excluded as they showed only very low absorption intensity and significant noise fraction. The maximum absorption position was determined in the 2326 or 2342 nm HyMap band. The chlorophyll absorption band centered ~660 nm was selected to characterize the green vital vegetation in the image because the overlaying influence on iron absorption in this range was significantly lower than in the blue wavelength regions, where both Fe-VIS and chlorophyll have intensive absorption bands. Initially, the determined absorption position ranged between 633 and 710 nm and the width between 92 and 228 nm. After evaluating the results, only those pixels with absorption position between 650 and 680 nm and width larger than 150 nm were classified as chlorophyll absorption. The dry and senescent vegetation was mapped on the basis of 2100 nm cellulose-lignin absorption band. The wavelength position for maximum

absorption based on laboratory experiments was detected between 2047 and 2119 nm. The shift of center absorption wavelength towards shorter wavelength was observed generally in the HyMap image data. The determined absorption width ranged between 55 and 252 nm, however, only those pixels with width larger than 170 nm were assigned to cellulose absorption band.

The spatial distribution and intensity of the determined absorption depths is shown in Figure 6.1. Most pixels with detectable Fe-NIR absorption were located in the center of the image, where volcanic parent material was present (Figure 6.1a). Very intense Fe-NIR absorptions were determined for the mining region east of Cortijo del Fraile where rock outcrops and mining waste rock piles covered large areas. Further iron absorption was detected on the alluvial fans south of Cerro Peñones. Fe-NIR absorption was determined both in the cultivated areas where no vegetation absorption features were present and in areas with abandoned cultivation with low dry vegetation cover (low cellulose absorption) (Figure 6.1a+d). In general, no iron absorption was detected in areas with high vegetation absorption.

The vegetation in the study area was mainly dry by the time of data acquisition (June 15 2005) and consisted of high fractions of dry leaves and woody components which is a typical protection of most plants against high sun elevation and hot and dry climate during the summer season. Hence the reflectance spectrum was dominated by cellulose and lignin absorption features. A few evergreen plants (e.g. *Chamaerops humilis*, *Opuntia*) developed strategies for protecting their leaves against the intensive sun radiation and low humidity. Due to the ongoing photosynthesis, these plants showed predominantly chlorophyll and plant water absorption features. Chlorophyll absorption was detectable mostly in the high elevated regions around Cerro Peñones in the center part of the study area, where matorral vegetation with evergreen plants such as dwarf-palms dominated (Figure 6.1c). Generally the chlorophyll absorption was accompanied by cellulose absorption because most plants consisted of dry and vital components in this area at this time of the year. The plants in the valleys and lower slopes were dried up by the time of HyMap data acquisition and hence showed only cellulose absorption (Figure 6.1d). Sporadically individual dwarf-palms and opuntia plantations growing in the valley caused detectable chlorophyll absorption. The Espartal vegetation (*Stipa tenacissima* dominated) dominating the northern and southern parts of the image was characterized in the dry season by a high fraction of dry and few green chlorophyll containing leaves.

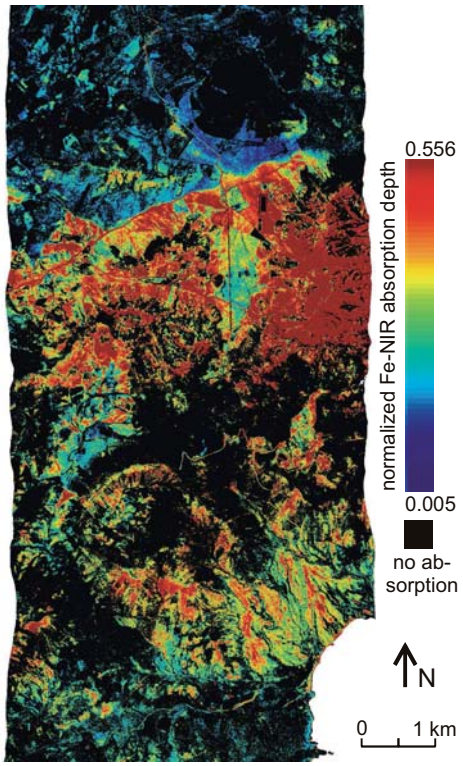

(a) hull-normalized Fe-NIR depth (~910 nm)

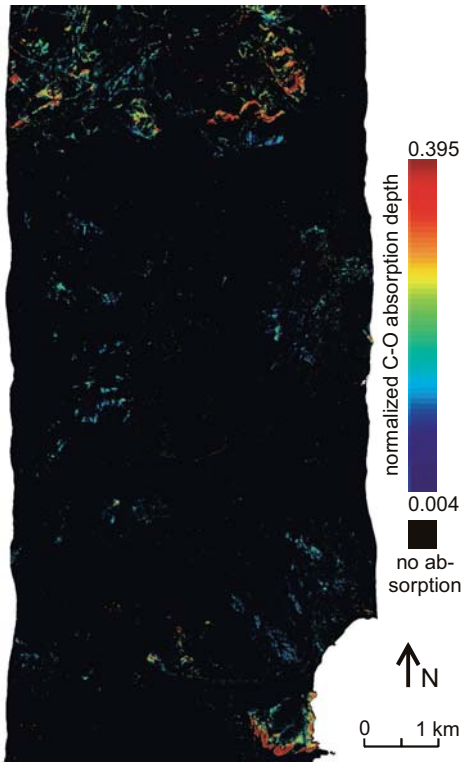

(b) hull-normalized C-O depth (~2340 nm)

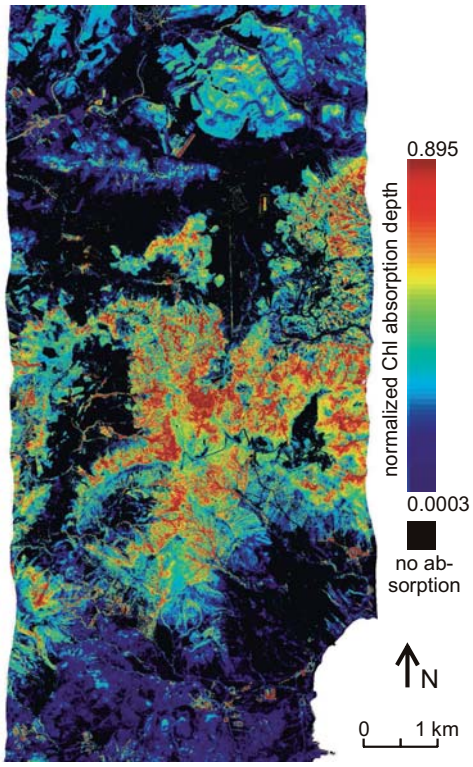

(c) hull-normalized chlorophyll depth (~660 nm)

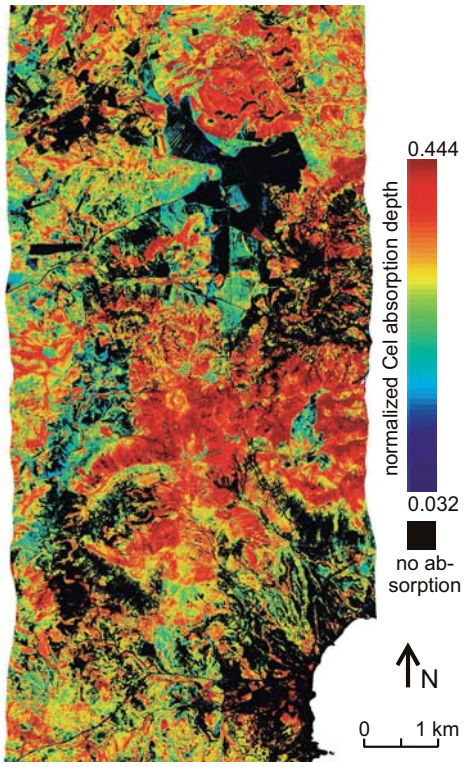

(d) hull-normalized cellulose depth (~2100 nm)

Figure 6.1: Maps of extracted soil and vegetation-related absorption features.

C-O absorption was only determined for small areas, mostly with very low vegetation cover (Figure 6.1b). There were pixel agglomerations in the northern part of the study area where carbonatic rocks were present and bordered the volcanic rocks. Further C-O absorption was determined for the outcrop of Quaternary cemented dunes along the seashore in the south-western corner of image (in red colors in Figure 6.1b). Occasionally C-O absorptions (in blue colors in Figure 6.1b) were detected on soil surface over volcanic rocks such as on the southern alluvial fans near the village La Isleta del Moro in the southeast image corner and in a small area west of the Cerro Peñones in the lower third of the image.

6.2 Transferring laboratory model to image data

6.2.1 Location and assignment of soil samples in the image

For the evaluation of the model performance, the soil sampling locations were determined in the geo-corrected image using the GPS coordinates. An accurate position determination was very difficult because the accuracy of the GPS measurements was ±5 m and the average error of geometric correction was 1-2 pixels (±5-10 m). Accordingly, the located sampling point could be shifted by 1-3 pixels in either direction. Further the sampling covered an area of 1 x 1 m compared to the pixel size 5 x 5 m. So each pixel represented the average of a larger surface area and small scale surface characteristics were homogenized. The use of 2 x 2 or 3 x 3 pixel average for each soil sample location resulted in even more homogenized reflectance spectra, in which also medium scale variations of the soil surface characteristics vanished. In comparable studies, the allocated image pixel of each sample location was determined using GPS data (Palacios-Orueta and Ustin 1998; Ben-Dor et al. 2006). In cases of large inaccuracies, a visually positioning of the plots using clearly recognizable objects in the image was performed (Bartholomeus et al. 2007). For the purpose of model validation, Jarmer et al. (2007) selected the pixel from a 3 x 3 pixel area centered around the GPS coordinate that was best matching the model results.

In this study each soil sample location was assigned to one image pixel based on the GPS coordinate. Due to the position inaccuracy of the GPS and geometric calibration, the chosen pixel might not be the exact one. A visual positioning of the sample locations, however, was not performed because of the total number of samples and insufficient number of links to clearly identifiable image objects. Nevertheless, due to the relative

homogeneity around the soil sampling areas at this spatial scale, the matching between HyMap pixel and field sampling location was considered to be adequate.

The performance of the laboratory model predicting Fe_d from the image data was evaluated from samples image spectra which showed Fe-NIR absorption features. The image spectra of six of the total 50 soil sample did not show Fe-NIR absorption due to intense vegetation cover or low Fe_d content. Based on field observation, the remaining 44 samples with detectable Fe-NIR absorption were distinguished into two groups. One group comprised 20 samples that were collected on permanently vegetated surfaces and the other group of 24 samples on cultivated fields. By the time of image data acquisition, six of the 24 soil samples from cultivated areas, were located on freshly harvested surfaces with strong cover of remaining crop residues. These samples were re-assigned to the group of vegetation influence samples. The remaining 18 samples were located on bare soil fields in the image data and were subsequently considered as pure soil surface samples. They spanned the whole Fe_d range between 3.7 and 33.5 g kg^{-1}. The Fe_d concentration of the 26 soil samples from vegetation affected image pixels ranged from 5.0 to 33.7 g kg^{-1}.

6.2.2 Soil texture influence

Soil texture affected the reflectance characteristics of the soil samples and the prediction of Fe_d content. The laboratory study on homogenized samples showed that coarser-grained soils produced more intensive iron absorption bands than finer-grained soils with the same Fe_d concentration. Accordingly, texture-dependent Fe_d modeling appeared to be adequate. However, the pixel-wise determination of the predominating soil texture from the image data was not possible. The comparison of the spatial distribution of coarse- and fine-grained soil samples in the study area revealed no relationships with respect to geological parent material, geomorphology or vegetation-related parameters. The spatial pattern of predominating soil textures appeared randomly, thus the Fe_d content was determined with a texture-independent regression model.

This was supported by the fact that the spectral differences between the samples with different soil textures were less distinctive in the image than they were found in the laboratory (Figure 6.2b). The normalized Fe-NIR absorption depths determined from the laboratory measured spectra could clearly be distinguished by the predominating soil texture (clay-silt- or sand-dominated) (Figure 6.2a). For the samples image spectra, the spectral differences between both soil texture groups were only small. While in the

laboratory study aggregation was removed by sample homogenization, it plays a significant role for natural unprocessed soil surfaces. Especially soils with high content of clay and silt particles can be highly aggregated. Thus aggregation overlays the true spectral influence of the texture and absorption bands may appear as intense as for coarse-grained soils with same quantity of absorbing material. Furthermore each image spectrum covers an area of 25 m² that consequently lead to a homogenization of spectral influence of small scale surface properties caused by soil texture differences.

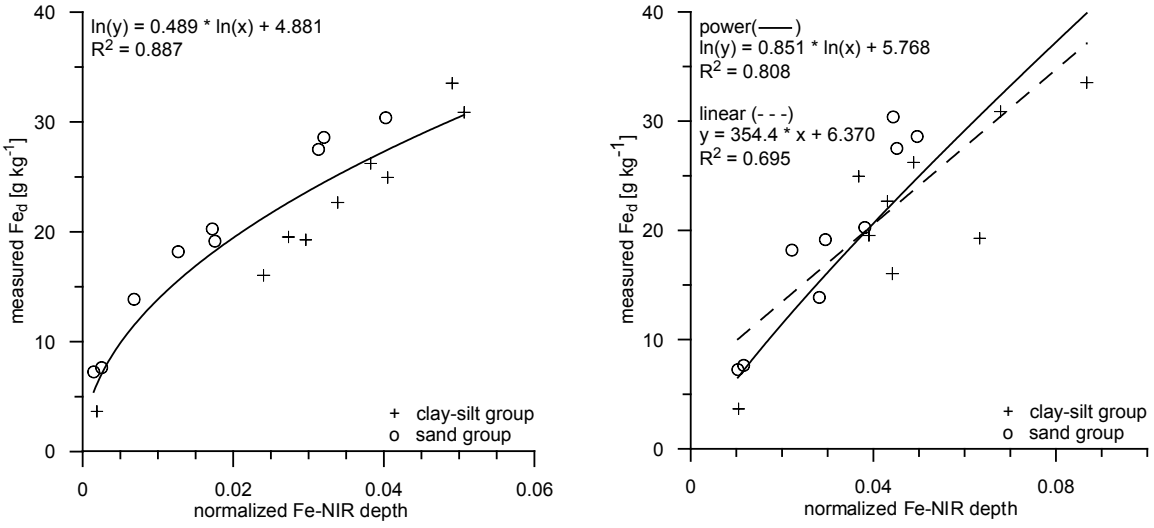

(a) from laboratory spectra (homogenized)

(b) from image spectra associated with sampling locations (pure soil surface samples)

Figure 6.2: Soil texture influence on normalized Fe-NIR absorption depth in laboratory and image spectra.

6.2.3 Comparison of laboratory and image soil spectra

The direct comparison of normalized Fe-NIR absorption depths of pure soil surface samples showed that Fe-NIR absorption was more intensive in the image than in the laboratory (Figure 6.3a). It further appeared that with increasing absorption depth the deviation between image and laboratory spectra increased. This caused an overestimation of Fe_d content (on average 8.7 g kg^{-1}) for the majority of samples when applying the texture-independent laboratory model based on Fe-NIR absorption depth (Figure 6.3b). Due to the modeling in natural logarithmic space, the overestimation of the samples with low and medium Fe_d concentrations was slightly higher.

There were several possible causes which could explain the stronger Fe-NIR absorption of soil samples in the image data and the deduced Fe_d overestimation. A systematic mislocation of the sampling positions was ruled out because of the general trend in all samples for more intensive absorption band and similar low variation of the absorption depth in both the image and laboratory spectra. An impact of potential secondary absorptions caused by other materials (water and hydroxyl-groups would be the most likely) in the NIR wavelength region was also ruled out for the following reasons. Soil inherent water and hydroxyl-groups occurred only as minor features in the NIR because the imagery was acquired in the study area during a dry period. The last rain fall event (2.4 mm) occurred two weeks before the campaign and the interim mean day temperature was 28 °C. According to a study by Haubrock et al. (2008) very high soil moisture contents were necessary to cause significant water absorption near 940 nm (also compare Figure 2.6). Plant water absorption bands (970 and 1170 nm) dominated the Fe-NIR absorption band when vegetation cover exceeded 25 % as discussed in chapter 5.4. This was indicated by a shift of the Fe-NIR absorption maximum towards longer wavelength. However, the examined soil samples originated from image area (bare cultivated fields) without vegetation cover and accordingly neither shifted Fe-NIR absorption maximum nor other vegetation-related absorption features were detected.

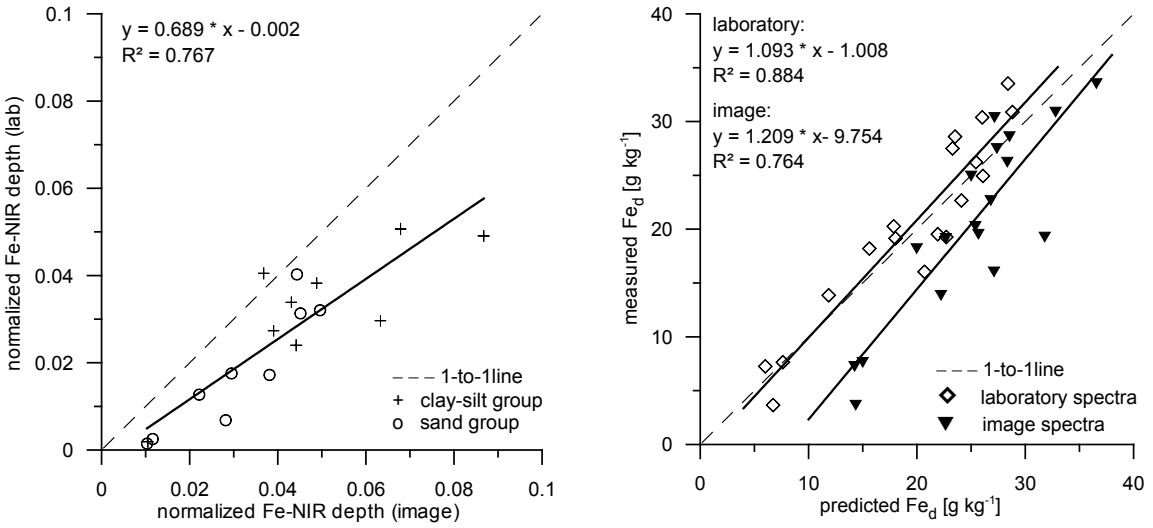

(a) Fe-NIR absorption depth

(b) model performance

Figure 6.3: Comparison of samples laboratory and image Fe-NIR absorption, and laboratory model performance.

The impact of soil texture differences was excluded because the examined soil samples of the clay-silt and sand-dominated texture group showed no significant difference in the depth of the Fe-NIR absorption bands. However, the aggregation of the soil samples in natural environment could be the reason for the differences between laboratory and image spectra. The comparison of sieved and homogenized laboratory sample spectra (chapter 5.2) showed that the 2-mm sieved sample had deeper absorption features which were attributed to particle aggregation. A similar conclusion seemed appropriate for the more intensive absorption features of the image spectra compared to the homogenized laboratory measurements. Figure 6.4 depicts for selected soil samples the normalized Fe-NIR absorption band of their image and laboratory spectra (both homogenized and 2-mm sieved). As the figures illustrate, the deviation of Fe-NIR absorption feature depth between image and laboratory spectra was significantly larger for the homogenized than for the 2-mm sieved spectra.

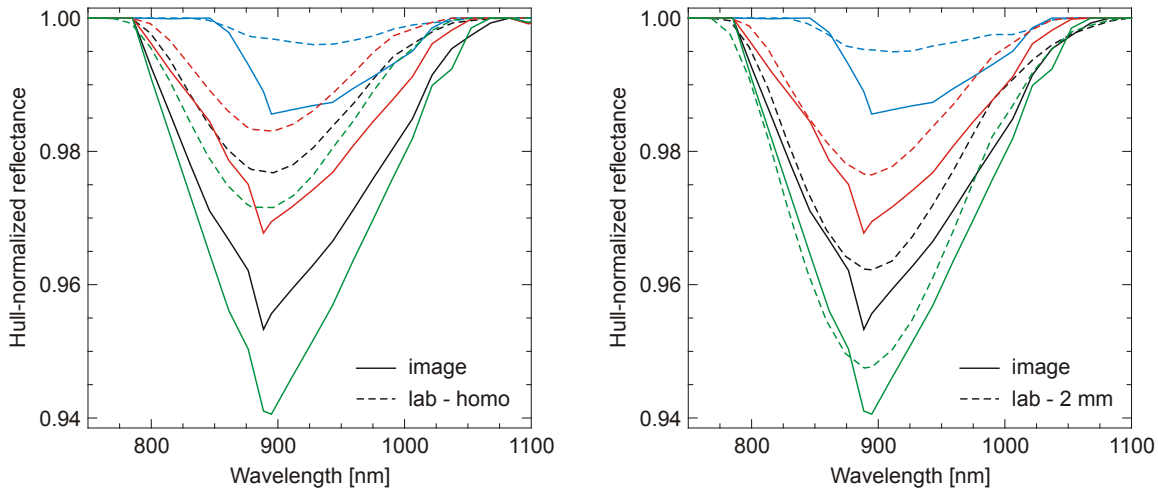

(a) image vs. lab (homogenized) spectra

(b) image vs. lab (2-mm sieved) spectra

Figure 6.4: Hull-normalized Fe-NIR absorption feature: comparison of image and laboratory (homogenized and 2-mm sieved) spectra for selected samples.

Some parts of the spectral difference between laboratory and image data could also be attributed to the data calibration. Besides soil and plant water absorption, the wavelength region between 900 and 960 nm in the image data was affected by atmospheric water vapor absorption which showed an absorption maximum at 940 nm. The impact of the atmospheric absorption was removed during the atmospheric correction. For this the water vapor content was estimated pixel-wise from the image data incorporating the additionally

occurring 970 nm plant water absorption in vegetated regions. Remaining artifacts were taken out by a filter implemented in ATCOR. In the NIR, the filter was applied to six continuous spectral bands from 911 to 990 nm. In the transition to the filtered wavelengths, artifacts appeared in the hull-normalized spectra mainly affecting the spectral bands at 888 and 894 nm. Here the absorption band was significantly deeper (Figure 6.4). This caused the automatic spectral feature extraction procedure to determine mainly these affected bands as Fe-NIR absorption maximum. Comparing image and laboratory spectra in Figure 6.4 showed that the spectral dip had strong effect especially on samples with low Fe_d content.

The right wing of the Fe-NIR absorption band featured high absorption values, too. However, this effect appeared to be less prominent with increasing absorption depth and Fe_d content. The left wing of Fe-NIR absorption band was less affected by spectral artifacts. By using the normalized depth of a single wavelength from the left wing of the Fe-NIR absorption band instead of the automatically extracted Fe-NIR absorption depth, the prediction of Fe_d content would be less susceptible to calibration artifacts. This would also minimize the overlapping spectral impact of denser vegetation as described in chapter 5.4. Based on these findings and the fact that the majority of the image pixels exhibited the calibration artifact at 888 to 894 nm in the hull-normalized spectrum, the Fe_d prediction modeling in the image was recalibrated using the normalized absorption depth of the 876 nm HyMap spectral band as predictor variable. This led to more stable and accurate results than using the automatically determined maximum absorption depth.

6.3 Determining pedogenic iron oxide content

As in the laboratory study a similar strong relationship was found between the hull-normalized Fe-NIR absorption depth at 876 nm in the image and measured Fe_d content in natural logarithmic data space (Figure 6.5). Three samples were identified that deviated from the general trend of the data and affected the correlation significantly. The two encircled samples below the trend line in Figure 6.5 were both located in homogeneous areas, where the surrounding 3 x 3 pixels areas showed similar absorption depths. No evidence of vegetation was found in the reflectance spectra, so both samples appeared to represent the natural variation of the data set. In general all soil samples from cultivated surfaces were collected far away from the field borders to prevent vegetation impacts. The marked sample above the trend line showed a too low absorption depth for analyzed high

Fe_d content. It originated from a heterogeneous area where the 3 x 3 pixels surrounding the sampling location differed significantly in their spectral properties. For example, the much higher Fe-NIR absorption depth of the neighboring pixel to the East fitted much better the model. However, not all samples could be located individually and corrected by their best matching neighboring pixel. Therefore, this sample was excluded from the calibration of the model. The correlation between measured Fe_d and Fe-NIR absorption depth at 876 nm improved from 0.805 to 0.854.

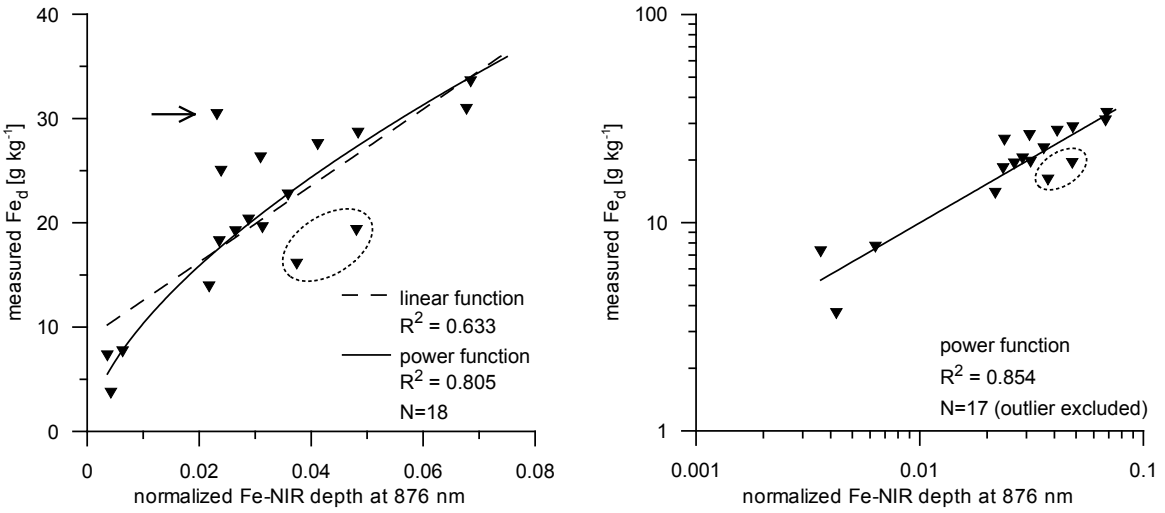

(a) linear data space (all pure soil samples) (b) logarithmic data space (outlier excluded)

Figure 6.5: Relationship between Fe_d content and normalized Fe-NIR depth of 876 nm spectral band in the image.

The laboratory developed texture-independent model for predicting Fe_d content was re-calibrated on the basis of the normalized 876 nm Fe-NIR absorption depth of 17 soil samples collected from pure soil surfaces (excluding the outlier marked with an arrow in Figure 6.5). Good estimates were obtained from the re-calibrated image Fe_d prediction model (R^2_v=0.803, $RMSE_v$=3.69, rel. $RMSE_v$=18.74%, RPD_v=2.19):

$$\ln (Fe_d) = 0.621 * \ln (\text{Fe-NIR depth at 876 nm}) + 5.161. \quad 6\text{-}1$$

Model residuals were normally distributed and not auto-correlated. The residuals mean was not significantly different from zero. The RPD_v of 2.19 for the image model was high and indicated excellent analytical efficiency of calibrations according to Dunn 2002. The regression line between measured and predicted Fe_d content in the scatter plot (Figure 6.6)

was very close to the 1-to-1 line, except for the of 1.556 at 0. The results were closely scattered around the 1-to-1 line. The samples with medium Fe_d content exhibited the highest variation.

The image model yielded comparably good results as the corresponding texture-independent laboratory model. The $RMSE_v$ of the image model (3.69 g kg^{-1}) was almost identical to the lab model (3.74 g kg^{-1}), while the rel. $RMSE_v$ of the image model slightly degraded from 18.11 % (lab) to 18.74 % (image). Conversely, the R^2_v had improved from 0.755 for the laboratory to 0.803 for the image model as well as the RPD_v (lab =1.93 and image = 2.19). Also slope and offset of the regression line of the image model were closer to the 1-to-1 line than of the laboratory model. It must be noted that the laboratory modeling was based on 45 samples whereas only 17 samples were available for the image model.

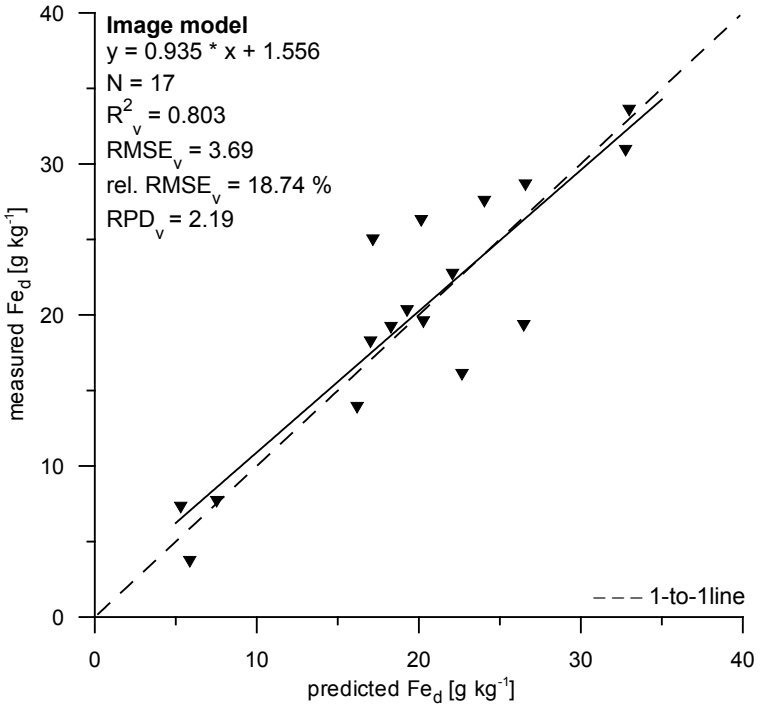

Figure 6.6: Image-calibrated Fe_d prediction model: Scatter plot of the cross-validated results.

6.4 Evaluating vegetation impact on Fe_d prediction accuracy

Vegetation had a dominant influence on the Fe_d prediction accuracy. In the laboratory study (see chapter 5.4), the 970 and 1170 nm plant water absorption was found to dominate the right wing of the Fe-NIR absorption band and induced a new absorption maximum when leaf cover exceeded 20 %. No significant shift of Fe-NIR wavelength position towards

longer wavelength was found for vegetation-affected image spectra. Soil samples collected from dense vegetated area did not show a detectable Fe-NIR absorption band in the image. The influence of vegetation was evaluated on the basis of 26 soil samples which were collected from surfaces with variable vegetation cover. Now the image calibrated Fe_d model was applied to the vegetation-influenced samples. Figure 6.7 depicts the prediction results of vegetation-influenced samples in comparison to the pure soil samples.

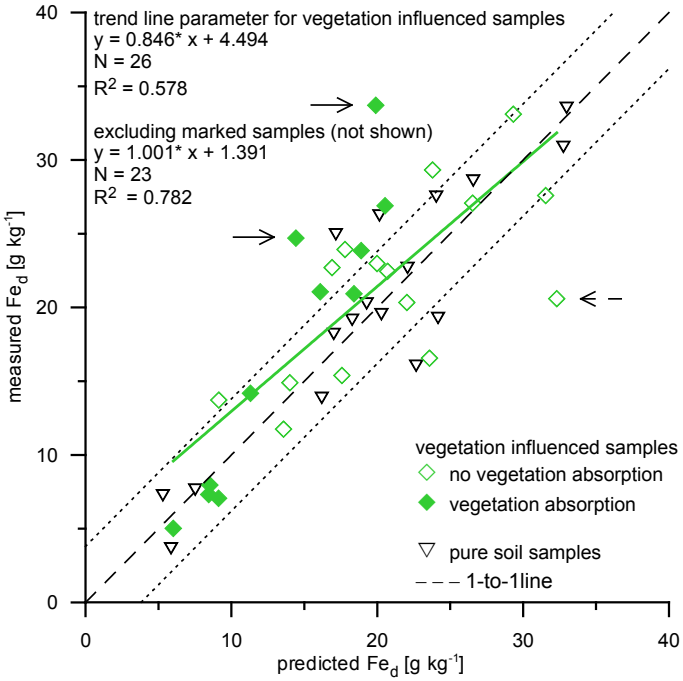

Figure 6.7: Fe_d prediction results for pure soil and vegetation-influenced soil samples. Confidence intervals are given for ±1 RMSE (3.85 g kg^{-1} Fe_d).

Vegetation-related absorption features (only cellulose absorption ~2100 nm) were detected in the image spectra of 11 soil samples indicating the presence of dry NPV. Chlorophyll absorption features, diagnostic for PV, were not determined. The Fe_d content was underestimated for seven soil samples with both Fe-NIR and cellulose absorption band detectable. This confirmed the findings of the laboratory analysis (see chapter 5.4) where increasing leaf cover caused the decrease of soil-related absorption features. The largest underestimation was obtained for the two soil samples marked with solid arrows in Figure 6.7. One sample was collected from small iron-rich eroded surface which was represented in only a few image pixels together with the surrounding vegetation. The second sample originated from a relatively pure soil surface which was interrupted by narrow stripes with opuntia plantations. The four samples containing relatively little Fe_d

were only slightly overestimated between 0.5 to 2 g kg^{-1}. No correlation (R=0.37) was found between the degree of Fe_d underestimation of the samples and their normalized cellulose absorption depth. This was attributed to the limited number of samples and their similar cellulose absorption intensity indicating similar vegetation cover. Hence, a relationship between Fe_d prediction accuracy and vegetation cover similar to the laboratory results could not be derived from the image data.

For the 15 other soil samples that were collected from areas with variable vegetation cover no vegetation-related absorption features were found in the image spectra. These areas were all abandoned from agricultural use for some years and were overgrown with different stages of vegetation succession. The vegetation cover, however, was still too low to show detectable absorption features in the spectra. In the laboratory study an average of about 20 % leaf cover was necessary to produce detectable vegetation-related absorption features that were distinguishable from other soil-related features. The sample marked with the dashed arrow in Figure 6.7 shows a significant Fe_d overestimation for which no meaningful explanation was found. There was no clear indication for an erosive surface found in the field and also the location in the image data appeared to be correct. The surrounding 3 x 3 pixels area was homogeneous and shows partly even higher Fe-NIR absorption intensity which would lead to higher overestimations. Even, when assuming no vegetation influence on this sample location, the overestimation for pure soil samples would be significant and beyond the models variance.

Table 6.1: Comparison of Fe_d model performance for cross-validated pure soil samples and vegetation samples.

	cross-validated results (pure soil samples)	**vegetation-influenced samples** (excluding three samples)	(all samples)
N	17	23	26
R^2	0.783	0.782	0.578
RMSE	3.85	3.83	5.47
rel. RMSE	19.5 %	21.8 %	30.1 %
RPD	2.19	1.80	1.31
trend line	0.934x + 1.454	1.001x + 1.381	0.846x + 4.494

The samples from plant-covered sites were not used for the model calibration. When interpreting them as validation samples, they reflected the excellent performance for the Fe_d prediction model. The trend line for all vegetation-influenced samples showed deviation on the order of one RMSE for samples with low Fe_d ($\leq$15 g kg^{-1}) and was close to the 1-to-1 line for high Fe_d content ($\geq$20 g kg^{-1}). However both R^2 and the trend line of

the vegetation-influenced samples were strongly affected by the three marked, significantly under- and overestimated samples. Excluding these samples, the R^2 improved strongly from 0.578 to 0.782 and the trend line shifted very close to the 1-to-1 line. Table 6.1 summarizes and compares the statistical quality parameters for the model performance for the cross-validated pure soil samples and the vegetation-influenced samples. R^2 and RMSE were identical for both data sets when not considering the three extreme samples. The trend line of vegetation-influenced samples was slightly closer to the 1-to-1 line than of the pure soil samples. Weak deviations were observed for the rel. $RMSE_v$. While the model could explain 80 % of the total variation in the pure soil samples, slightly less variation of 78 % was explained for the vegetation-influenced samples.

There was a higher uncertainty and inaccuracy for the Fe_d prediction of the samples from vegetated surface. With respect to the two underestimated samples with significant vegetation influence, the performance of the model was classified in three categories. The first category included the pure soil surfaces with agricultural use, where Fe_d content was predicted with excellent accuracy. The outline of the cultivation areas in Cortijo del Fraile was mapped manually. The second category comprises areas for which no vegetation absorption features (chlorophyll and/or cellulose absorption depths) were detectable and that did not belong to the first category. For these areas Fe_d predictions were possible with high accuracy. The third category included all areas for which Fe-NIR and vegetation absorption features were determined. Here Fe_d predictions were possible with a somewhat reduced accuracy.

6.5 Spatial distribution of pedogenic iron oxides

6.5.1 Development of soil iron surface map and prediction accuracy

The pedogenic iron oxide content was estimated from the geo-coded, radiometrically and atmospherically corrected HyMap image data based on the image-calibrated prediction model. The Fe_d regression model was applied for all soil surfaces with detectable Fe-NIR absorption. The Mediterranean Sea, roads and settlements were masked in the image, also areas with high vegetation density covering all soil spectral absorption features. Mining areas such as east of Cortijo del Fraile were especially indicated. Due to the non-linear exponential relationship between the variables of the model, predictions outside the calibrated model range contained an increasingly high error fraction. The laboratory measured Fe_d content ranged from 3.5 to 33.7 g kg^{-1} for the collected soil samples which

defined the calibration range for the developed regression model. Those pixels with higher predicted Fe_d concentration than 33.7 g kg^{-1} were assigned to a special class. Figure 6.8 shows the spatial distribution of pedogenic iron oxide in the study area. The prediction accuracy of the Fe_d modeling depending on the vegetation influence is depicted in the subsequent Figure 6.9.

The Fe_d concentration of most soil surfaces (mining areas excluded) in the image was within the calibrated model range (6.33 - 33.7 g kg^{-1}). The model range was exceeded mostly by single pixels or groups of less than ten pixels. These were mainly identified as beach sediments and rock outcrops located at the upper mountain regions and tops within the dense vegetated areas. There were no large contiguous areas where the model needed to extrapolate. This showed that the soil sampling covered the large variability of the pedogenic iron oxide content in natural soils in the study area. In the upper part of the image, the transition between iron-rich volcanic geology and iron-absent volcanic and carbonatic geology was clearly visible. The pedogenic iron oxides on the carbonatic bedrock accumulated slowly during the pedogenesis while carbonates were dissolved. On average 0.61 % (equal to 6.1 g kg^{-1}) Fe_2O_3 were determined by XRF as iron source in the carbonatic parent material. The carbonatic soils of the vegetation-free cultivated areas contained on average 12.8 ±2.2 g kg^{-1} Fe_d indicating the beginning accumulation (green-yellow coded in Figure 6.9). The abandoned cultivated areas with low vegetation cover showed no to very little iron oxide content with Fe_d concentrations close to the lower detection limit. The soils in the transition zone between carbonatic and volcanic bedrock contained on average 14.4 ±3.1 g kg^{-1} Fe_d (yellow coded). The pedogenic iron oxide content in the soils with volcanic parent material was on average 19.7 ±4.1 g kg^{-1}. The volcanic parent material with its iron-bearing minerals was highly variable in composition which was reflected in the high standard deviation. The highest Fe_d concentrations were found southwest of Cortijo del Fraile where dacites with Fe-rich biotite and amphiboles occurred as parent material over large areas.

Growing plants on the soil surface can lead to underestimations of the Fe_d concentration. When directly comparing the Fe_d content of the cultivated (non-vegetated) and the abandoned cultivated (vegetated) areas, no evidence for continuous underestimation of the vegetated areas was found. The average Fe_d concentrations of both areas was very similar 18.3 ±6.4 g kg^{-1} for the cultivated and 19.3 ±4.4 g kg^{-1} for the abandoned cultivated areas. Both cultivated and non cultivated areas were located on the volcanic and carbonatic bedrocks and hence covered the full variety of pedogenic iron oxide distribution.

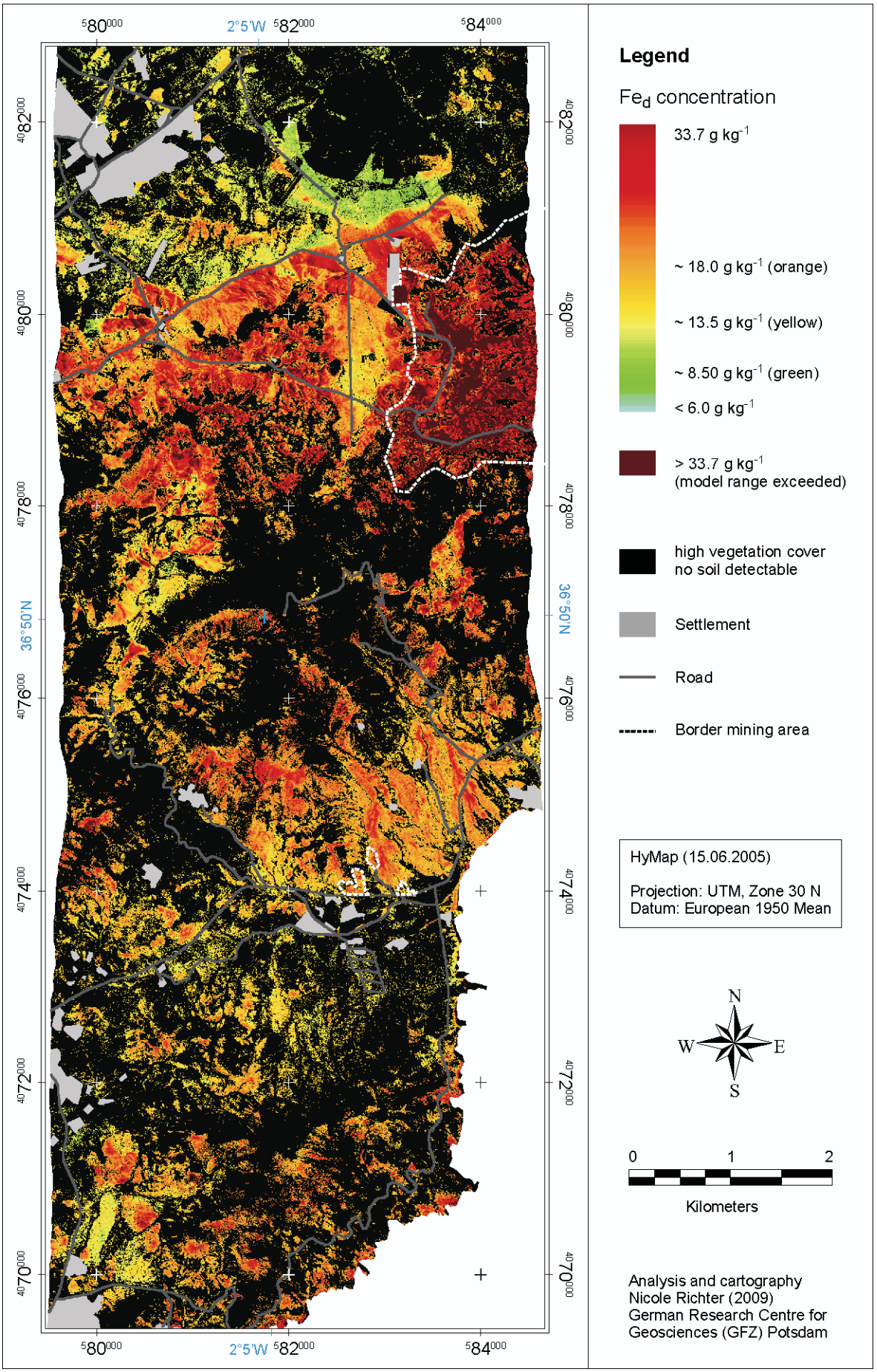

Figure 6.8: Spatial distribution of pedogenic iron oxide (Fe_d) concentration.

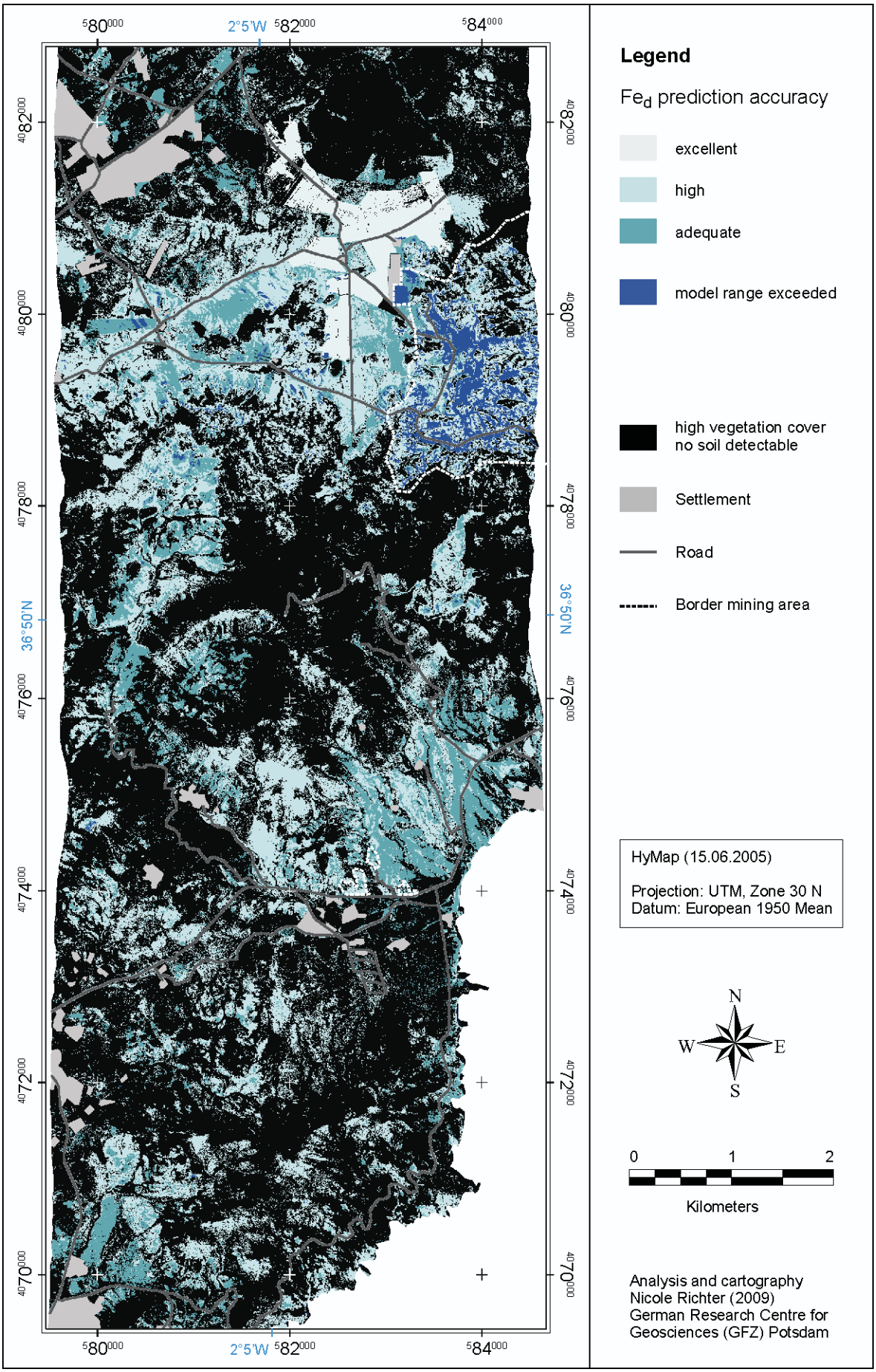

Figure 6.9: Prediction accuracy of Fe_d modeling.

6.5.2 Fe_d concentration as pedogenic indicator

The pedogenic iron oxide concentration is an important indicator for soil development and formation because it accumulates in the soil profile during pedogenesis as a weathering residual. Figure 6.10 summarizes the characteristics of a well-developed soil profile with distinct iron oxide accumulation in the B horizon that was exposed along a road cut on the alluvial fan near the village La Isleta del Moro. Well developed soils show a characteristic separation into different soil horizons which can be distinguished by their typical chemical and physical properties. Three main soil horizons were distinguished in the shown profile with the mineral B horizon divided into two sub-horizons. The organic Ah horizon contained the highest SOC contents compared to the underlying horizons. The Bw/t sub-horizon was characterized by accumulation of iron oxides and clay minerals whereas secondary pedogenic carbonate accumulations dominated the BCk sub-horizon below. The parent materials (C horizon) were alluvial sediments originating from biotite and amphibole bearing dacites and andesites from the surrounding mountains. Biotite and amphibole acted as main iron sources for the formation of pedogenic iron oxides. Plagioclase and hornblende were calcium source for the formation of pedogenic carbonates. No intercalations of carbonatic rocks were described for this area.

Besides chemical properties (Figure 6.10b), also reflectance spectra of the soil horizons were clearly distinguishable. Most obvious were the albedo variances between the spectra which were mainly caused by differences in $CaCO_3$ content (Figure 6.10c). The $CaCO_3$ content of samples from both B horizons (542 and 627 g kg^{-1}) was even higher than those determined from the 50 soil surface samples and produced a detectable absorption band centered at 2340 nm. The significantly lower albedo of the Ah horizon spectrum was mainly attributed to the low $CaCO_3$ content of only 90 g kg^{-1} which matched the average $CaCO_3$ content of the 50 soil surface samples. The 10.4 g kg^{-1} SOC of the Ah horizon seemed to cause a flattening of the spectrum in the VIS/NIR region and reduced detectability of the Fe-VIS and Fe-NIR absorption bands. This was in contradiction to literature (e.g. Baumgardner et al. 1985; Ben-Dor et al. 1999) where a visual spectral influence of SOC was described for concentrations greater than 20 g kg^{-1}. Compared to the collected soil samples, the Ah horizon spectrum resembled in its SOC impact very much the spectra of two samples taken from densely vegetated surface both containing over 20 g kg^{-1} SOC (compare to Figure 5.7). However, there was no conclusive explanation found for the unusual strong SOC impact on the reflectance spectra of the profiles Ah horizon.

(a) soil profile = steeply dipping road cut (blue pen as scale about 15 cm)

soil horizon	Fe_d [g kg^{-1}]	SOC [g kg^{-1}]	$CaCO_3$ [g kg^{-1}]
Ah	21.8	10.4	9
Bw/t	15.1	6.2	452
BCk	7.5	4.3	627

(b) chemical composition of soil horizons

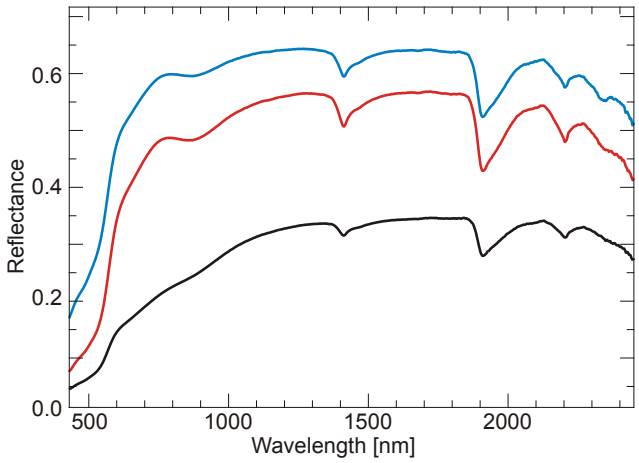

(c) reflectance spectra

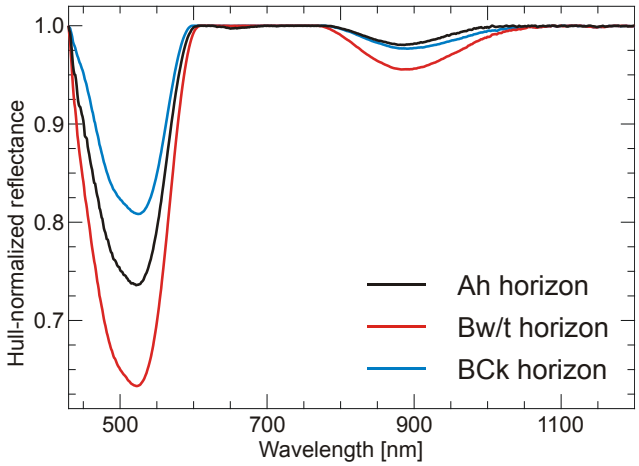

(d) hull-normalized spectra

Figure 6.10: Characterization of a natural soil profile (road cut) on the alluvial fan near the village La Isleta del Moro.

When analyzing the hull-normalized iron absorption bands, the Bw/t horizon spectrum showed a significant deeper absorption than the Ah horizon despite its lower Fe_d content of 15.5 g kg^{-1} compared to 21.8 g kg^{-1} of the Ah horizon (Figure 6.10d). Due to SOC influence, the Fe-NIR absorption band of the Ah horizon spectrum was even as low as the BCk horizon which only contained 7.5 g kg^{-1} Fe_d. The Fe-NIR absorption band of the Bw/t horizon spectrum was significantly deeper than the spectra of most collected soil samples. Only one soil surface sample showed a similar intensive Fe-NIR absorption which led to significant overestimation of the Fe_d content by both laboratory and image models. This sample was collected undoubtedly from an eroded site where a lower soil horizon was exposed to the surface. However, the Fe-VIS and Fe-NIR absorption depth range of Ah and Bw/t horizon spectra was found to be most similar to the according surface soil samples of

comparable Fe_d content. The generally low vegetation density on the investigated 50 soil surfaces and historically intensive agricultural land use accounted for the low SOC content and accumulation which was the opposite of the examined soil profile where dryland agriculture of cereals was still practiced.

The different physicochemical properties of the horizons also contributed to the differences in iron oxides absorption behavior as they impinged the way of how iron is bound and distributed in the soil profile. Hence the Fe_d prediction model needs to be adapted to varying conditions of the soil horizons and if possible applied independently in order to minimize the prediction error and avoid significant overestimations. Considering the different chemical composition of the B horizons, the joint occurrence of iron oxides and carbonates in volcanic regions can be used as pedogenic indicator for potentially capped profiles of which lower soil horizons are exposed after removal of top soil layers. By combining the Fe_d and C-O absorption map, large contiguous soil surfaces near the villages Casas los Precillas (Figure 6.11) and La Isleta del Moro (Figure 6.12) were identified where both iron oxides and carbonate occur at the same time.

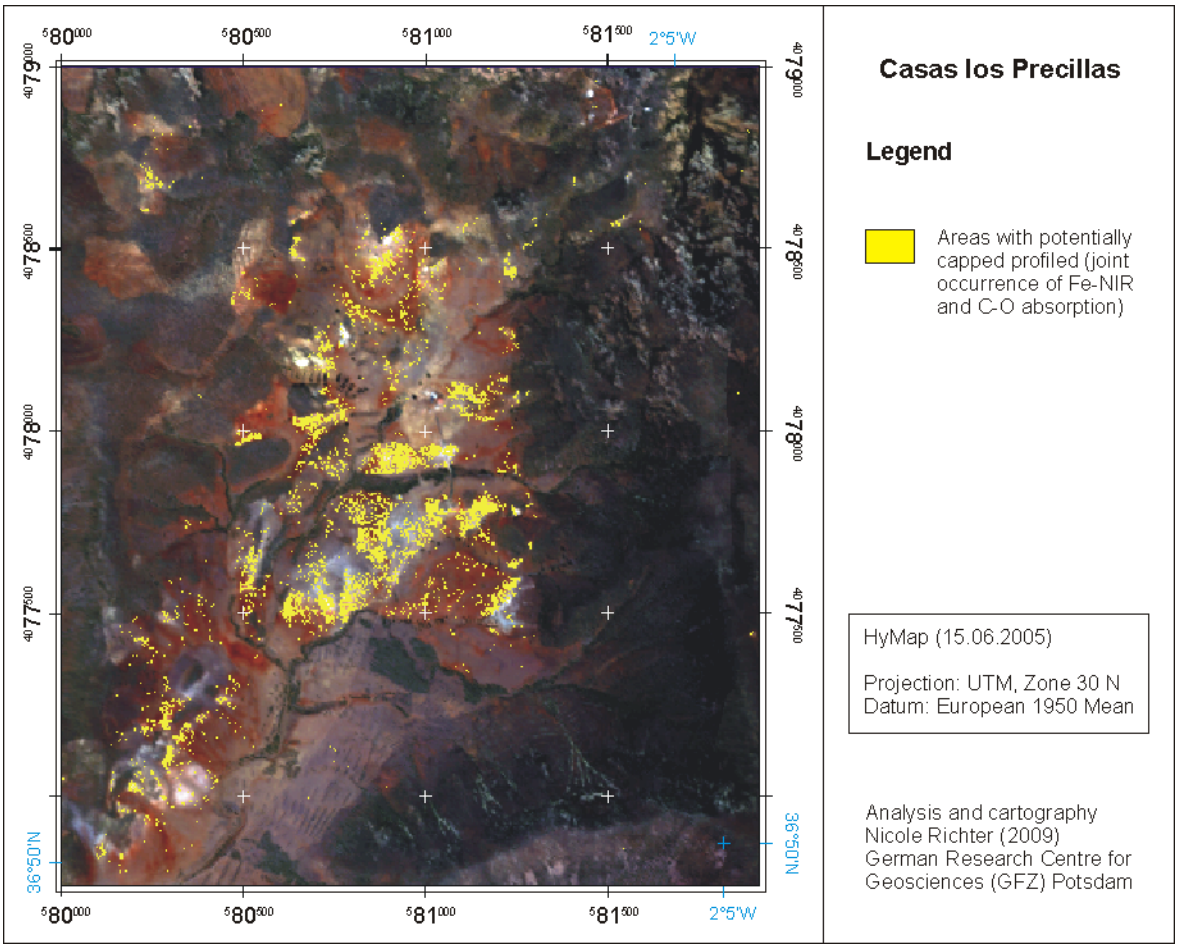

Figure 6.11: Map of potentially capped soil profiles near Casas los Precillas based on joint occurrence of pedogenic iron oxides and carbonates on the soil surfaces.

The potentially capped soil profiles in the valley of Casas los Precillas are shown as yellow-coded surfaces in Figure 6.11. Volcanic material, mainly andesites and dacites, underlay the area with no record of intercalated carbonatic bedrock in the geological map (Instituto Geologico y Minero de Espana 1983). The continuous accumulation of pedogenic carbonates in the B horizon was described for most soil profiles in the valley. Due to high erosion rates (Aguilar et al. 1989), the upper soil layers were removed and both iron oxides and carbonates could spectrally be detected on the soil surface. The determined areas with joint occurrence of both mineral groups were located on the upper slopes and the edges of cultivated fields. Additional large areas were mapped at the lower slopes and the valley bottoms, where carbonatic soil material seemed either to be deposited from the above eroded sites or exposed by cultivation processes such as plowing.

The detected carbonates occurring in conjunction with iron oxides on the quaternary alluvial fans near the village La Isleta del Moro (Figure 6.12) are secondary pedogenic formations (Aguilar et al. 1990; Harvey et al. 1999).

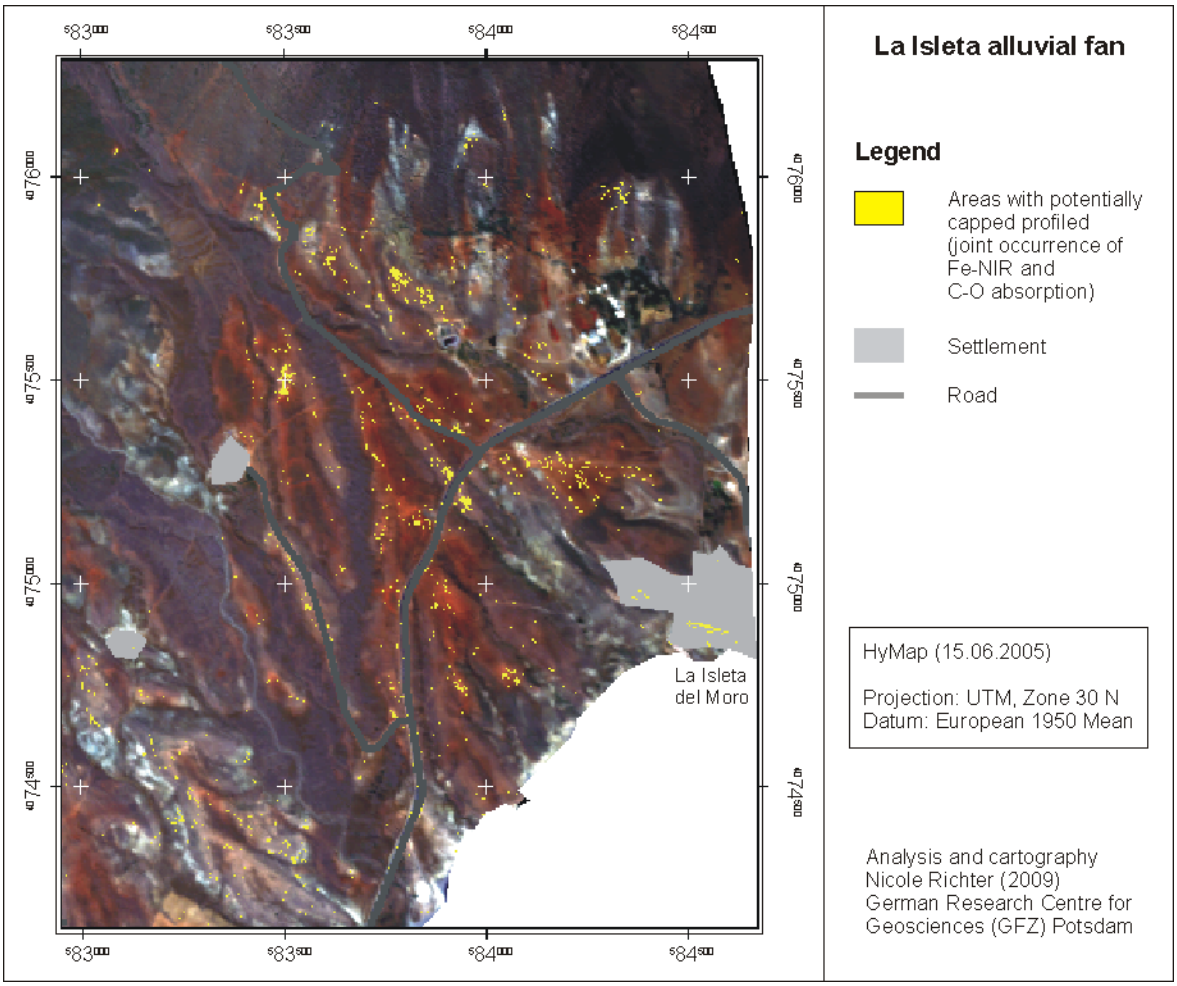

Figure 6.12: Map of potentially capped soil profiles near La Isleta del Moro based on joint occurrence of pedogenic iron oxides and carbonates on the soil surfaces.

The highest quantities of pedogenic carbonates accumulated in the B horizon of soils that developed on depositional surfaces of the fan. These were separated by differently sized trenches which cut into the older sediments during erosional phases. The depositional surfaces were primary humps between two trenches from where soil material could easily be translocated (Figure 6.13). Here, the detectability of carbonates on the surface was a strong indicator for the erosion of former A horizon material.

(a) depositional surface in the middle part of the fan (b) trench in the lower part of the fan

Figure 6.13: Characteristic geomorphologic surface types of the La Isleta alluvial fan.

The soils on the depositional surfaces were characterized in Harvey et al. (1999) study mainly as the oldest and most mature (Qf1) out of three soil surfaces of different age. As distinguishing features, the redness rating, stage of carbonate accumulation and Fe_d values were used. High values of these parameters were indications for distinct pedogenesis and hence older soil. The relation between redness rating and iron oxide content and soil age was already described in previous studies (e.g. Torrent et al. 1983; McFadden and Hendricks 1985). Indeed, there was a very good match found when overlaying Fe_d and Harvey's map. High Fe_d concentrations were mainly located on Qf1 soil surface while Qf3 soils showed mainly lower Fe_d contents (Figure 6.14). Harvey et al. (1999) had described a significant difference (using Student's t-test) in Fe_d values between Qf1, Qf3 and Qf5 surface groups. Also other studies (McFadden and Hendricks 1985; Bullard and White 2002; Ben-Dor et al. 2006) had used the accumulation of iron oxides in the process of pedogenesis and linked the iron oxide content as an important indicator to soil age and development status.

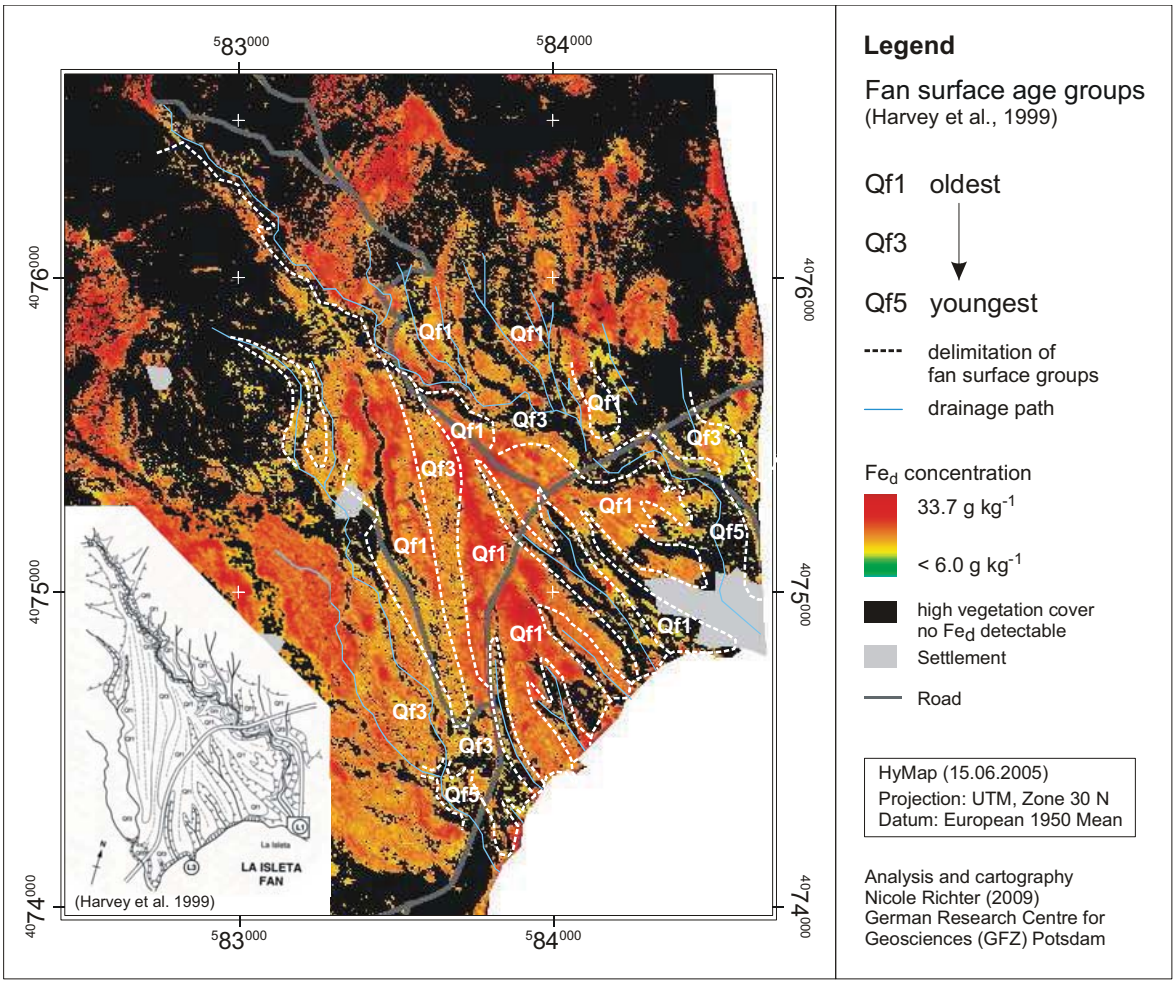

Figure 6.14: Fe_d content map of La Isleta alluvial fan with delimitated fan surface age groups integrated from Harvey et al. (1999).

Chapter 7: **Discussion**

In the previous chapters regression models for the determination of pedogenic iron oxide concentration from spectral reflectance measurements were developed under laboratory conditions (see chapter 5) and applied to image data for the assessment of spatial pedogenic iron oxide distribution (see chapter 7). A number of possible factors affect the model performance when moving across scales and employing different sensors. The laboratory models were developed on homogenized soil samples that allowed the detailed study of soil texture spectral impact as well as soil-vegetation interaction. Sensor and data related factors play an important role when leaving the laboratory level towards in-situ conditions. According to Lagacherie et al. (2008) these factors include amongst others spectral sensor characteristics (spectral resolution and SNR), radiometric calibration, spatial variability, view conditions and surface status.

In the course of this chapter, the performance of the iron prediction models is discussed in terms of model, sensor and surface conditions. The initially proposed research questions are answered.

7.1 Modeling assumptions

Models represent a simplification of the real world. Based on a small number of variables it is tried to explain rather complex relationships and processes. The developed regression models described the complex relationship between pedogenic iron oxide content and the reflectance properties in a simplified procedure. Three basic assumptions were made for the model development and evaluation under laboratory conditions and subsequent transfer to image data and natural environments.

- Pedogenic iron oxides have an influence on the spectral reflectance characteristics of soils.

Fundamental basis for the quantitative determination of soil chemical properties from reflectance measurements is that the considered parameter affects the soil reflectance behavior. For pedogenic iron oxides this was reported extensively in literature (see chapter 2.2) and shown in own independent laboratory investigations (chapter 5.2).

- The Fe_d content can be directly related to iron absorption features which in turn can be used as basis for a Fe_d regression model.

Ferrous and ferric ions as other chemical components of the soil particles produce wavelength-dependent and material specific absorption bands due to specific dielectric properties. Three diagnostic iron absorption features were determined in the VIS and NIR wavelength region with the second iron absorption band appearing only as weakly developed feature. A strong relationship was found between the Fe_d concentration and spectral absorption features of the Fe-VIS and Fe-NIR bands (see chapter 5.2 and 5.3).

- Other soil chemical properties (e.g. clay or carbonates, organics, moisture) have negligible influence on the developed Fe_d regression models.

Mineralogical components of the soils (clay and carbonates) produce detectable absorption features mainly in SWIR wavelength region outside the range of iron absorption. Spectrally effective soil organic content above 20 g kg^{-1} was only determined for soil below dense plant cover. From these surfaces, however, no Fe_d content could be determined in the image due to the vegetation coverage. The majority of examined soil samples from open or low vegetated surface contained spectrally negligible SOC (chapter 5.2). Spectrally significant variations in the soil moisture content of the soil surfaces were ruled out due to the HyMap data acquisition during a continuous dry period.

7.2 Model evaluation

7.2.1 Model variables

The selection of suitable input variables is important for the successful modeling. The number of variables determines the model complexity. A larger number of variables may increase the accuracy of prediction, but with each new variable the model complexity increases and manageability decreases. The actual gain of additional model variables is therefore difficult to foresee because a high model complexity makes it more difficult to apply or transfer it to different data sets. In the following, the suitability of the used model input variables are discussed on the basis of correlation spectra and in comparison with other spectral features.

Correlation spectra

The correlation spectrum described the relationships between Fe_d content and each individual wavelength of soil reflectance or hull-normalized spectra. The correlation spectra of the Fe_d content and reflectance spectra demonstrated significant relationships for the VIS wavelengths that related to Fe-VIS absorption (Figure 7.1a). No distinct deviation was found in this wavelength region for the three different texture groups. The NIR and SWIR wavelength region of the reflectance spectra showed a different correlation behavior depending on texture. Only the clay-silt-dominated samples showed a significant correlation between Fe_d and wavelengths for the Fe-NIR absorption region ($R<-0.71$) which slightly reduced with longer wavelength. Albedo variations between the different texture groups seemed to be a possible explanation as well as the different chemical compositions of the soil texture groups that could induce an indirect relationship of iron oxide content and reflectance intensity (described e.g. by Jarmer 2005).

The correlation spectra of Fe_d content and the wavelength of the hull-normalized spectra showed good correlations ($R<-0.85$) in the VIS and NIR wavelength region related to the Fe absorption bands (Figure 7.1b). Through the performed hull-normalization texture-related albedo variations were removed, thus texture-dependent differences in the correlation coefficients were reduced. This demonstrated the necessity of the prior spectral pre-processing. The strong relationships of Fe_d content and Fe-VIS and Fe-NIR absorption wavelengths for texture-dependent and texture-independent soil sample groups proved the significance and suitability of the derived spectral absorption features in the Fe_d modeling.

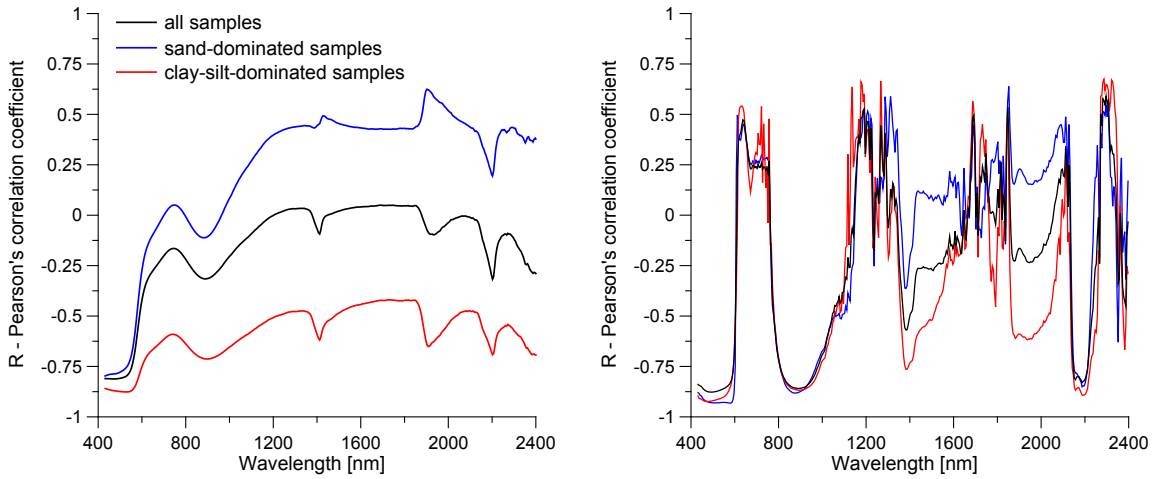

(a) for reflectance spectra

(b) for hull-normalized spectra

Figure 7.1: Correlation spectra for Fe_d content.

Iron absorption features

The Fe_d models were based on single linear regression analysis. The hull-normalized absorption depth of either the Fe-VIS or Fe-NIR absorption band was used as predictor variable. This approach was favored over the multiple linear regression analysis because no significant improvements of the model performance were obtained by combining iron absorption features with each other or with standard color indices. The interdependence of the predictor variables was identified as the main reason. Therefore no information increase was gained for the model by additional variables.

From all extracted spectral features, the normalized depth feature returned the best correlation for both iron bands (see chapter 5.3). The use of the absorption depth feature for modeling was preferred over other highly correlated spectral features (e.g. absorption area), because the specific selection of wavelength neighboring the maximum absorption depth avoided the unwanted extraction of vegetation or processing artifacts (see chapter 6.2.3). Although both iron absorption bands showed the same high suitability for Fe_d modeling (compare in Figure 7.1b), the Fe-NIR based model was chosen to apply to hyperspectral image data. Main benefit over the Fe-VIS absorption was its relative independence from vegetation-related absorption features as described in chapter 5.4. This was especially important because most image pixels represented mixtures of different surface components (such as soil and plants). While the Fe-VIS absorption band was masked quickly by chlorophyll absorption when green vegetation cover increased (Figure 5.16), the right slope of the Fe-NIR feature was only affected by weak plant water absorption at 970 nm (Figure 5.16). Using the normalized absorption depth of a single wavelength from the left slope of the Fe-NIR absorption band allowed accuracy-limited Fe_d predictions also for higher vegetation coverage. The correlation spectra for hull-normalized soil spectra proved strong relationships of Fe_d content and neighboring wavelengths of the maximum absorption

Another advantage of favoring the Fe-NIR over the Fe-VIS absorption was its complete representation in the reflectance spectrum. In general the Fe-VIS band has a very wide character and only the right shoulder can be measured in the visible part of the spectrum. Therefore, the first wavelength at which the hull-normalization starts is user-biased. This has implications on the subsequently extracted spectral features. Especially the wavelength position of maximum absorption may be shifted.

7.2.2 Calibration range

The Fe_d prediction models were calibrated between 3.5 and 33.7 g kg^{-1} Fe_d concentration because this range was covered by the soil samples. The Fe_d contents of soils exceeding the calibrated range need to be extrapolated by the model and may therefore not be correct. It is rather expected that higher iron oxide concentrations will cause an intensity saturation of the absorption band. For example Torrent et al. (1983) observed absorption saturation for hematite content above 50 g kg^{-1} when investigating soils of Brazil containing up to 160 g kg^{-1}. The soils examined in the frame of this study, did not reach the Fe_d content at which saturation of Fe-VIS or Fe-NIR absorption band occurred. Due to the exponential nature of the Fe-NIR model, significant Fe_d underestimations were expected for all samples exceeding the model calibration range. These regions were therefore designed separately in the Fe_d content map. The affected pixels were mainly attributed to natural and mining-related rock outcrops. The Fe_d content of all contiguous soil surfaces (cultivated and agricultural abandoned) fell within the model calibration range.

The sensor spectral sensitivity and SNR limited the prediction of Fe_d concentrations below the calibration interval. Both in the laboratory and image spectral data sets, some soil samples with Fe_d content below < 10 g kg^{-1} showed distinct Fe-NIR absorption bands whereas some did not. Therefore a 10 g kg^{-1} threshold was defined to assure reliable predictions based on the Fe-NIR model also for low Fe_d content. Fe_d estimation below this concentration may still be possible for some samples but involves higher error probability.

In contrast, the Fe-VIS absorption band resolved well even very low Fe_d concentrations due to approximately five times larger absorption intensity (Figure 5.4). Ben-Dor et al. (2006) for example found a good correlation (R^2=0.834) between very low Fe_d concentrations of sand dunes (0.2 to 3.9 g kg^{-1}) and Fe-VIS absorption depth. For accurate prediction from image data, however, the absence of vegetation from the soil surface is mandatory, since vegetation-related absorption features interfere strongly with Fe-VIS absorption.

7.2.3 Model performance

Laboratory modeling

Best prediction accuracies in the laboratory were obtained for Fe-VIS texture-dependent models (R^2_v 0.878 for sand, 0.813 for clay-silt), which was explained by the significantly deeper Fe-VIS compared to the Fe-NIR absorption band (factor 12). The Fe-NIR depth-based model for sand-dominated soil samples, however, explained a data variation

(more than 86 %) as good as the corresponding Fe-VIS model (Table 7.1). The performance for sand-dominated samples was significantly better (on average + 5 % explained total variation), which was attributed to the homogeneous distribution and binding of iron on the soil grains. The more heterogeneous texture range of the clay-silt-dominated samples (see Table 5.3) was one main cause of a higher variance of the prediction results and consequently a weaker model performance. Only a sufficient prediction accuracy was determined for the Fe-NIR based clay-silt model, which was the lowest for all models (R^2_v=0.695). Additional factors interfering in this case may for example be different ratios of hematite and goethite concentration, which could lead to high variation of the absorption intensity. Due to the lack of appropriate mineralogical analyses, this assumption could not further be examined but remaining an interesting aspect for future investigations.

In comparison to the texture-dependent models, the texture-independent laboratory models obtained just sufficient accuracies. Fe_d predictions with similar R^2_v but significantly lower error were obtained from texture-independent Fe-NIR than the Fe-VIS model (Table 7.1).

Table 7.1: Summary of Fe_d prediction results from laboratory study (Fe-NIR only) and HyMap image data on volcanic soils.

Model	texture	N	R^2_v	$RMSE_v$ [g kg^{-1}]	rel. $RMSE_v$ [%]	RPD_v
Fe-VIS laboratory	**sand-dominated**	25	0.878	2.86	15.89	2.69
Fe-NIR laboratory	**sand-dominated**	22	0.875	2.72	13.91	2.89
Fe-VIS laboratory	**clay-silt-dominated**	25	0.813	3.59	17.57	2.02
Fe-NIR laboratory	**clay-silt-dominated**	23	0.695	4.13	19.04	1.72
Fe-VIS laboratory	**texture-independent**	50	0.772	3.98	20.74	1.94
Fe-NIR laboratory	**texture-independent**	45	0.755	3.74	18.11	1.93
HyMap image (Fe-NIR)	**texture-independent**	17	0.803	3.69	18.74	2.19

Results are cross-validated using ‘leave one out’ method.

Compared to conventional laboratory chemical analysis, the higher prediction error of the spectroscopic analysis is compensated by the possibly significant higher number of samples to be analyzed. The particular objective of the study defines the requirements for the prediction accuracy. In this study, a cross-validated model performance with more than 75 % explained total variation and prediction error of less than 15 % were considered appropriate.

For both texture-dependent and texture-independent groups, the use of the Fe-VIS and Fe-NIR absorption depth as predictor variables allowed better estimates than the methodologies presented in other laboratory studies. Indeed, in comparable texture-dependent studies, good Fe_d estimations for homogeneous dune sands were obtained by Ben-Dor et al. (2006) with R^2=0.89 and by Bullard and White (2002) with R^2=0.73. Both investigated the Fe_d linked to rubification with redness indices derived from spectral measurements. Using the iron absorption depths in this study, we attained an R^2=0.834 for Fe-VIS and 0.875 for Fe-NIR model. Comparable texture-independent studies on natural soils were performed with reasonable to good results by Bartholomeus et al. (2007) (R^2_v=0.67) and Brown et al. (2006) (R^2_v=0.73). These approaches were based on statistical parameters of the Fe-VIS absorption band (Bartholomeus et al. 2007) and PLS regression models (Brown et al. 2006) using multiple input variables. The presented single variable approaches for both Fe-VIS and Fe-NIR absorption bands gave even better estimates (R^2_v=0.744 and 0.755).

Image modeling

The texture-independent modeling of HyMap image data yielded slightly better results (R^2_v=0.803) than the corresponding laboratory model (Table 7.1) which was attributed to the coarser spatial resolution of the image (25 m² per pixel) compared to the laboratory (4 cm²) causing a homogenization of small scale textures and Fe_d spatial variations. The explained total variation in the data of over 80 % demonstrates the excellence of the model on image level.

The quantitative determination of Fe_d concentration from remote sensing image data and spatial distribution was performed in only a few studies. As continuation to the laboratory study, Ben-Dor et al. (2006) predicted the Fe_d content of homogenous dune sands from CASI data (spectral sensor range: 400-1000 nm) based on the redness index. They obtained a validated R^2 of 0.73 and RMSE of 0.04 g kg^{-1} for 13 validation samples and an overall accuracy of 78 %. In contrast to that a much weaker correlation was determined by Bartholomeus et al. (2007) when applying the laboratory Fe_d prediction model to ROSIS data (spectral sensor range: 417-873 nm). Based on the redness index a validated R^2 of 0.22 was obtained for 16 validation plots and R^2_v of 0.19 using standard deviation of spectral features in the 550-nm absorption band. Despite the variability of the soil texture, the model performance of the presented study based on the Fe-NIR absorption depth yielded a significantly better prediction accuracy (R^2_v=0.78, $RMSE_v$=3.85 g kg^{-1}) than

Bartholomeus' and Ben-Dor's studies considering that the latter was performed on homogeneous sand dunes.

The accuracy of the Fe_d map was further evaluated against soil sample analyses provided by Harvey et al. (1999). Harvey sampled the B horizon of soils at various locations on the alluvial fan near the village La Isleta and obtained an average Fe_d content of 15 g kg^{-1}. This fitted very well with own measured Fe_d concentration of the soil profiles B horizon (15.5 g kg^{-1} Fe_d) investigated in the same area (see Figure 6.10). The average Fe_d concentration determined for the soil surface from the HyMap image data was 19.6 g kg^{-1}. It fitted well with Fe_d content measured in the same soil profiles A horizon (21.8 g kg^{-1}). Local variations and spatial averaging of Fe_d concentrations in the image data may cause the deviation of approximately 2 g kg^{-1}.

7.3 Sensor-related impact factors

7.3.1 Spatial and spectral resolution

Spatial resolution is a limiting factor when locating the soil samples in the image for model evaluation. There was a large difference in scale between soil sampling in the field on 1 m² and 25 m² pixels in the HyMap image. The soil sample locations in the field were measured with ±5 m precision by GPS. The geometric accuracy of the HyMap data was determined between 5 to 10 m (±2 pixels). Despite possible spatial deviation, the closest pixels to the GPS coordinates were assigned as soil sampling locations. The comparison of the corresponding laboratory and image derived Fe-NIR features yielded a good correlation of R^2=0.76 for the majority of samples (see Figure 6.3a). Only one strongly mismatching sample was identified. The good model performance and evaluation in the image proved the suitability of combining 5 m resolution, geometrically corrected HyMap data with GPS coordinates.

The 30 x 30 m spatial resolution of image data from e.g. current (Hyperion) and future (EnMap) spaceborne hyperspectral instruments is too low to represent a 1 m² (or less) sampling location within a 900 m² pixel. So the described model's validation procedure cannot be applied. A consistency check of predicted data and Fe_d spatial distribution based on field knowledge is recommended for qualitative evaluation of the model accuracy as presented in a study on Landsat TM data by Jarmer (2005).

The spectral resolution affects the detectability of absorption features, their shape, size and location of absorption maximum. The spectral resolution of the HyMap image data (128 spectral bands with 12-16 nm bandwidth) was much lower than the ASD spectra (2151 bands with interpolated 1 nm bandwidth) and thus had direct influence on the size of the spectral features. The absorption position extracted from the HyMap image spectrum can be shifted by ±8 nm due to the different bandwidths. In order to evaluate the impact of the spectral resolution on the absorption feature calculations, laboratory ASD spectra of the soil samples were resampled to 2005 HyMap sensor configuration and spectral features were extracted automatically using the parameters in Table 4.4. The comparison of measured ASD and simulated HyMap spectra showed a very good match for both Fe-VIS and Fe-NIR absorption bands. The average deviation between ASD and simulated HyMap for the Fe-NIR absorption depth was 4.2 % and the area feature 5.3 %. The average deviation for Fe-VIS absorption depth and area features was estimated with only 2.1 % due to the three times more intense absorption in this wavelength region. This demonstrated the high suitability of both sensors for the Fe_d modeling.

7.3.2 SNR and radiometric resolution

Besides the spectral resolution, the detectability and quality of the spectral features depends significantly on the signal-to-noise ratio (SNR) and radiometric calibration of the sensor. The impact of SNR on the Fe_d prediction accuracy was simulated on the basis of HyMap reflectance spectra of pure soil samples. Ten SNR steps were investigated 1000:1, 850:1, 650:1, 500:1, 400:1, 300:1, 200:1, 100:1, 50:1, and 10:1. The percentage noise fraction equivalent to each SNR step, e.g. 0.002 % for SNR of 500:1, was calculated for each wavelength and spectrum, individually and then subtracted from it. The change of the SNR with albedo of the spectra was not considered. The hull-normalization was then applied to the SNR-simulated spectra and the depth of the Fe-NIR absorption band at 876 nm was extracted. Subsequently the Fe_d contents were predicted from these depths (Fe-NIR image model). The maximum Fe_d prediction error was calculated as difference between predicted Fe_d concentrations of the SNR-simulated and original unmodified spectra. Figure 7.2 shows the maximal prediction error with the percentage noise fraction for the SNR on the x-axis. A perfectly linear relationship was found between the increasing noise fraction and resulting prediction error. However, for better visualization purposes the x-axis in the figure is shown in logarithmic scale. The results showed that noise-induced

inaccuracy in the prediction become relevant when SNR dropped below 200:1 (0.005 % noise fraction). The model yielded very robust predictions for spectra with simulated SNR higher than 200:1.

Both the ASD field spectrometer and HyMap sensor have very high SNR which will not affect the spectral absorption features. Most airborne hyperspectral instruments achieve nowadays a high performance level in terms of SNR. However this is not the case for current hyperspectral spaceborne instruments which cannot achieve such a good SNR performance in the SWIR. On the other hand satellite instruments are especially interesting for mapping Fe_d distribution because they acquire regularly data over very large areas and in most cases reasonable SNR can be achieved in the VNIR. Currently available data of the Hyperion sensor showed rather low SNR between 147 (at 700 nm) and 90 (at 1025 nm) (Beiso 2002), thus Fe_d predictions would contain an increased error level. In contrast the upcoming spaceborne EnMap hyperspectral instrument has a great potential for large-scale mapping of Fe_d since the sensor is designed to achieve a SNR of >500:1 in the VIS/NIR (Kaufmann et al. 2006).

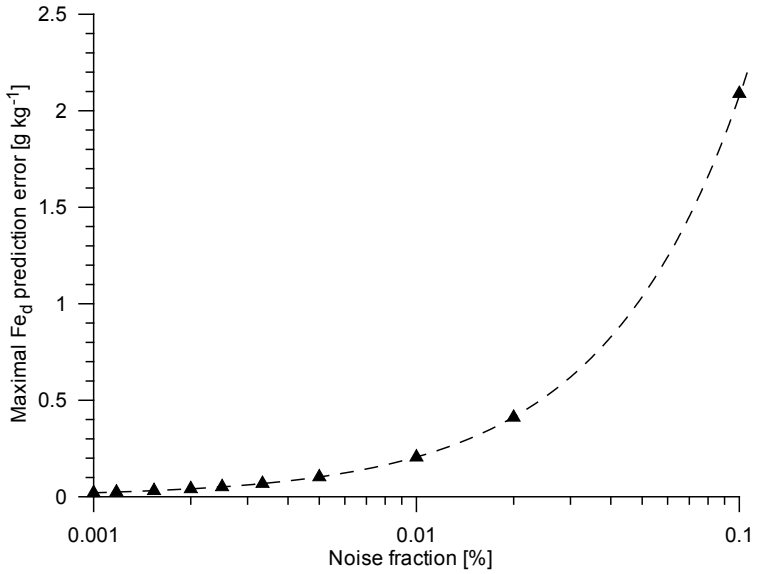

Figure 7.2: Impact of different SNR to Fe_d prediction.

7.3.3 Atmospheric correction

During the atmospheric correction of images, the at-sensor radiance data were corrected for atmospheric influences and transformed into surface reflectance. The atmospheric water absorption band centered near 940 nm impacted the Fe-NIR feature, because it

overlaid the right side of the absorption feature. In order to avoid residual artifacts in the reflectance spectrum, the atmospheric water vapor content was determined on a pixel to pixel basis from the image data to adjust for variations (Richter and Schläpfer 2002). Due to the complexity of atmospheric modeling an artifact-free correction was rarely achieved and spectral smoothing was applied afterwards. If the remaining artifacts were located in the maximum Fe-NIR absorption region, these were likely to be extracted as spectral feature by the automatic extraction procedure instead. Consequently the extracted absorption depths would yield significant Fe_d misestimations (see chapter 6.2). By using hull-normalized depth of the neighboring spectral band at 876 nm on the left slope of the Fe-NIR, a more realistic estimation of the Fe_d content was possible. Due to the lower variation of the spectral absorption depth values, the image model needed to be re-calibrated and obtained the same good performance as the laboratory models.

Wrongly extracted spectral features and errors remaining after atmospheric calibration can affect the Fe_d prediction. In order to evaluate their potential impact on the model prediction accuracy, an error of ±5 % was applied individually for each wavelength and spectrum. The hull-normalization was performed and absorption depths at 876 nm were extracted. The Fe_d contents were predicted based on the Fe-NIR image model and compared to the original prediction.

The ±5 % noise added to the image data resulted in an under- or overestimation of the Fe_d content between -1.01 and 1.03 g kg^{-1}. The size of the error increased with Fe_d content. Samples with measured Fe_d concentrations up to 15 g kg^{-1} were under- and overestimated up to 0.5 g kg^{-1}, samples with higher Fe_d content up to 1 g kg^{-1}. The performance of the model in terms of R^2, RMSE and rel. RMSE remained unaffected. The impact of higher noise fraction or miscalculation of the feature size on the prediction errors was much lower than expected, which proves the stability and robustness of the models. However, the noise fraction is in reality not constant over the entire image as in the simulation, why weaker model performance is expected. It is therefore highly recommended to use a spectral band which is unaffected by the artifacts of radiometric calibration to minimize a large noise-driven variation of the Fe-NIR absorption depth values.

7.3.4 View conditions

A possible cause for variable noise fractions in the image data was attributed to the view conditions (illumination and viewing angles of the sensor). Depending on the pixel location across the image (image edges or center location) deviations could be found in the

corresponding reflectance spectra. This is especially the case for sensors with wide FOV such as HyMap (61°) where the pixels at the edge are recorded with a 30° sensor viewing angle. In fact, the HyMap sensor was used in the past to investigate the impact of the viewing geometry on the spectral measurements (Beisl et al. 2000).

With respect to the Fe_d prediction, larger deviations of the model residues were expected at the images edges than in the center. Although no specific correction for the view conditions were applied during the atmospheric correction, the Fe_d prediction residues seemed not to show a relationship to the across-track location in the image (Figure 7.3). Both center and edge pixels (viewing angles larger than 15 %) showed the same variance level.

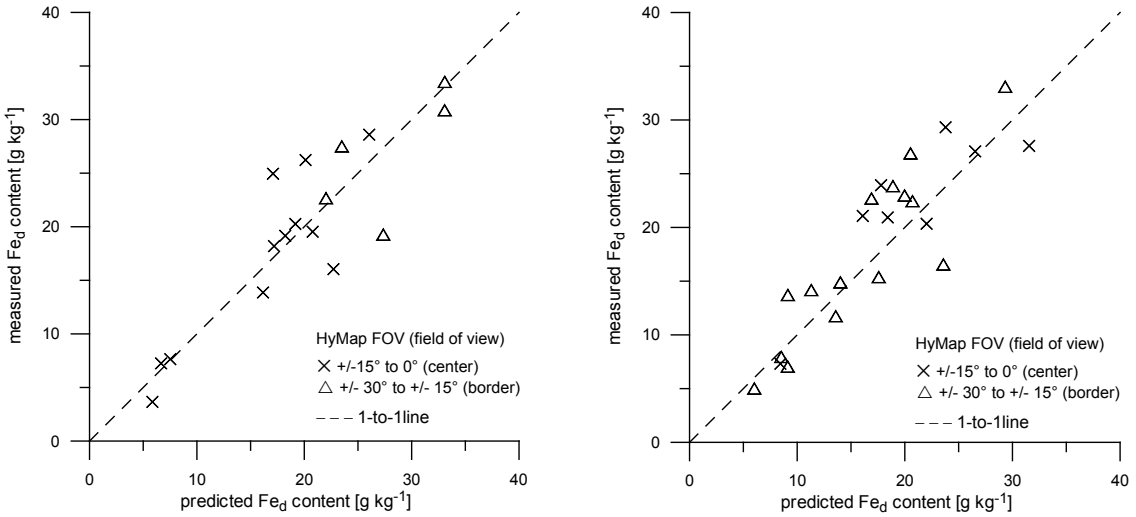

(a) pure soil samples (cross-validated results) (b) vegetation influence samples

Figure 7.3: Location of the soil samples across the image.

7.4 Soil surface-related impact factors

7.4.1 Soil texture and surface roughness

Due to the heterogeneous grain size distribution, the examined soil samples were subdivided into two soil texture group using 50 % sand content as criteria. A significant difference in the laboratory spectral reflectance of sand-dominated and clay-silt-dominated soil samples was found which consequently led to the development of texture-dependent Fe_d prediction models. With exception of the Fe-NIR clay-silt model, these models obtained significantly better prediction accuracies than texture-independent models.

Interesting in this context was the question whether better Fe_d predictions could be obtained when separating soils in the image data with respect to their texture (Figure 7.4). The setup and calibration of a Fe-NIR depth image model based only on the image spectra from pure sand-dominated samples resulted in excellent prediction accuracy for the sandy samples itself (N=8, R^2=0.963, RMSE=1.48 g kg^{-1}). However, only eight samples were available for the model building, which were considered not to represent the entire data set. The setup of a corresponding model with clay-silt-dominated samples did not give reasonable results due to the low number of samples (N=9), all with similar Fe_d concentrations. For the entirety of pure soils in this study with mixed grain size distribution, very accurate Fe_d predictions (R^2=0.803, RMSE=3.69 g kg^{-1}) were obtained indicating that the strong relationship between Fe_d content and Fe-NIR absorption depth for the sand-dominated samples may act as stabilizing element in the model.

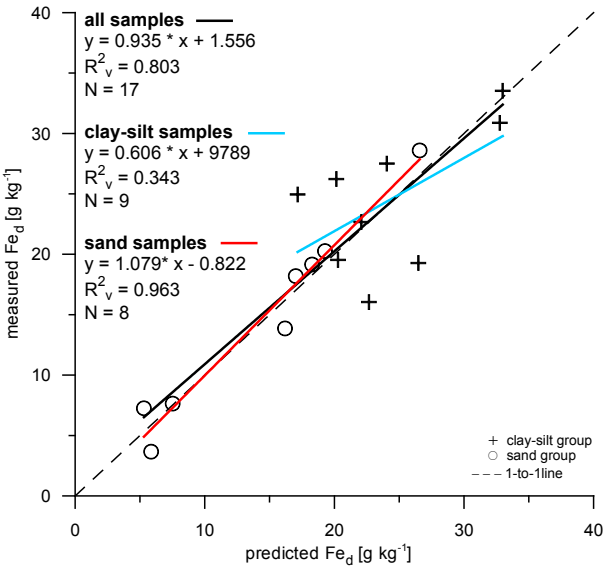

Figure 7.4: Image model results for texture-dependent and independent soil sample groups.

The Fe_d prediction from hyperspectral image data was performed on the basis of the texture-independent Fe-NIR model because the dominating soil texture could neither be determined directly from the image data nor derived from other information sources (e.g. soil or geological maps). In addition, the texture of pixels in the HyMap image could be of much higher variability than in the laboratory, because rocks or plowed fields for example can also be present in the FOV introducing much higher surface roughness. When highlighting associated soil texture in the image model results (Figure 7.4) no trend for Fe_d over- or underestimation of the soil texture groups was found as observed in the laboratory

(compare Figure 5.13). Results were evenly distributed around the 1-to-1 line. However the variance of the prediction results showed distinct differences between the soil texture groups. An excellent model performance with very low variance characterized the Fe_d prediction results for the sand-dominated samples. These accurate predictions were obtained due to the homogeneous distribution of iron oxides that were mainly bound as coatings on the soil grains.

In contrast, the Fe_d prediction results for clay-silt-dominated samples yielded a much wider variance which agreed with findings of the laboratory study. There, the more heterogeneous grain size and a less even iron oxide distribution were identified as potential sources. In fact, the iron oxides in finer-grained soils occur e.g. as free crystals, are bound in various ways to clay minerals and organic components, and act as aggregating component between individual soil grains (Birkeland 1999). The larger internal surface areas make the finer-grained soils chemically more active than coarse-grained soils and cause a higher degree of aggregation between soil particles. The heterogeneous iron oxide distribution and soil aggregation affected the spectral response of the soil surface and led to larger variation between different samples. In contrast to soil samples examined in the laboratory where aggregation influences (e.g. multiple scattering and shadowing) were minimized by homogenization, the aggregate size rather than the soil texture altered the soil spectra under field conditions and hence affected the Fe_d prediction from natural soil surfaces (Orlov 1966; Baumgardner et al. 1985). There, large aggregate size may overlay the spectral influence of the soil texture.

Besides soil texture and aggregation, the soil roughness was characterized by the presence and nature of pebbles and rocks. High fraction of rocks on the soil surface may lead to significantly different spectral behavior as Jarmer (2005) showed for limestones and soil color. Similarly impacts on iron absorption bands and subsequently on Fe_d prediction results can be expected for increased rock cover because the parent material contains in general considerably different (often higher) iron concentrations than the soils (compare XRF results in 5.1). During the field sampling campaign, the rock cover on the soil surface was only qualitative categorized in three groups (low, medium and high) without precise quantification. This information did not allow an accurate evaluation of the impact of rock cover. The soil map described medium cover of pebbles on the soil surfaces in the study area but without giving a percentage fraction. For the cultivated areas a medium

pebbles/rocks cover was also described during the field campaign. However pebbles and rocks were completely covered by the soil material. A medium to high pebbles/rock cover was determined for abandoned fields and areas with matorral vegetation, but again fine soil particles largely covered the rock surface due to strong winds in the study area.

7.4.2 Vegetation cover

The accuracy of the pedogenic iron oxide mapping from hyperspectral image data was impaired when plants were growing on the soil surface. Important influencing factors were the surface coverage of the plants and their vitality status. The vitality status of plants is decisive for their absorption features. Exemplarily, the spectral influences of different green, dry and a mixed grass leaves cover on soil surface reflectance were investigated in a laboratory study (see chapter 5). The results implied that an increasing coverage of the soil surface with plant material caused a decreasing of Fe-VIS and Fe-NIR absorption depths. At 10 % coverage with green leaves, Fe_d prediction from Fe-VIS absorption depth was already inhibited due to strong overlaying of chlorophyll absorption. As indicator for mixed and dry leaf cover, plant water and cellulose absorption features were determined as they were spectrally extractable for 20 % and more leaf cover. For lower leaf cover, impacts on the albedo were observed which reduced the Fe-NIR absorption depth already at 10 % leaf cover. Consequently lower Fe_d concentrations were predicted (Figure 5.18).

A corresponding behavior was found in the image data for those soil pixels which also showed detectable vegetation absorption features. The Fe_d contents of these pixels were clearly underestimated. A different behavior was observed for the soils with low vegetation cover that did not show vegetation absorption features in the image pixels. They were predicted in the same accuracy range as the pure soil samples (see Figure 6.7) with no trend for Fe_d underestimation. A Fe-NIR absorption decrease due to albedo influence of the plants in the VIS/NIR was rarely noticeable other than in the laboratory results. A possible cause could be dust containing reflective iron oxide particles that partly covered the plants in the field. Strong westerly winds and the east-west orientation of most valleys in the study area support the blow out of fine soil particles and their subsequent deposit on plants and rocks.

Furthermore, the complexity of the natural spectral response of plants can hardly be modeled in the laboratory. The use of horizontally lying leaves represented a simplification of the natural conditions. First, leaves are spectrally very variable between different species (Curran 1989; Elvidge 1990). Further other plant components such as branches and stems

are contributing to the spectrum. Most important, the vertical structure and geometry of the plant has a decisive influence on the spectral response of the plant which cannot be modeled adequately by using only one horizontal layer. Fully leaved plants can cover the underlying soil almost completely. Return reflectance spectra are dominated accordingly by vegetation absorption features.

A single leaf layer was chosen for the laboratory setup despite its inhibited simplification because it allowed a very good estimation of the percentage leaf coverage on the soil surface. A similar controlled experiment with complete plants would require a significantly larger setup that is hardly practicable in the laboratory. Accordingly the experiment would entail other interfering parameters, such as the dependence of estimated plant coverage from the viewing geometry. Numerous different species would be needed due to their variable spectral response and plant geometries, in order to allow a more realistic modeling of the vegetation cover.

As an alternative approach for estimating the fractional vegetation cover, the spectral mixture analysis (SMA) is often used. Its suitability was tested to evaluate the Fe_d prediction accuracy. The results of the performed iterative multiple endmember SMA (μMESMA) computation (Bachmann 2007) did not show a relationship between fractional vegetation cover and residues of the Fe_d estimation, neither for the pure nor the vegetation-influenced soil samples (Figure 7.5). Nine different endmember spectra for soil, non-photosynthetic and photosynthetic active vegetation were used for the calculation performed by Bachmann (2007). In the result the fractional cover of PV and NPV were summed up. An average error of ±10 % was estimated for the determined surface cover abundances based on field data.

Both samples with high and low fractional vegetation cover showed a similar range of the prediction residues. Only the vegetation-influenced samples with fractional vegetation cover greater than 30 % and detected absorption features showed a higher deviation from the 1-to-1 line. For the vegetation-influenced samples without detectable absorption features, fractional vegetation cover between 6 and 42 % was determined and no trend of less precise Fe_d predictions was found. The Fe_d concentration of two soil samples was almost accurately predicted by the model although fractional vegetation cover greater than 30 % was estimated. Only for three pure soil samples 0 % fractional vegetation cover was obtained and their predicted Fe_d concentrations fitted well in the model accuracy range.

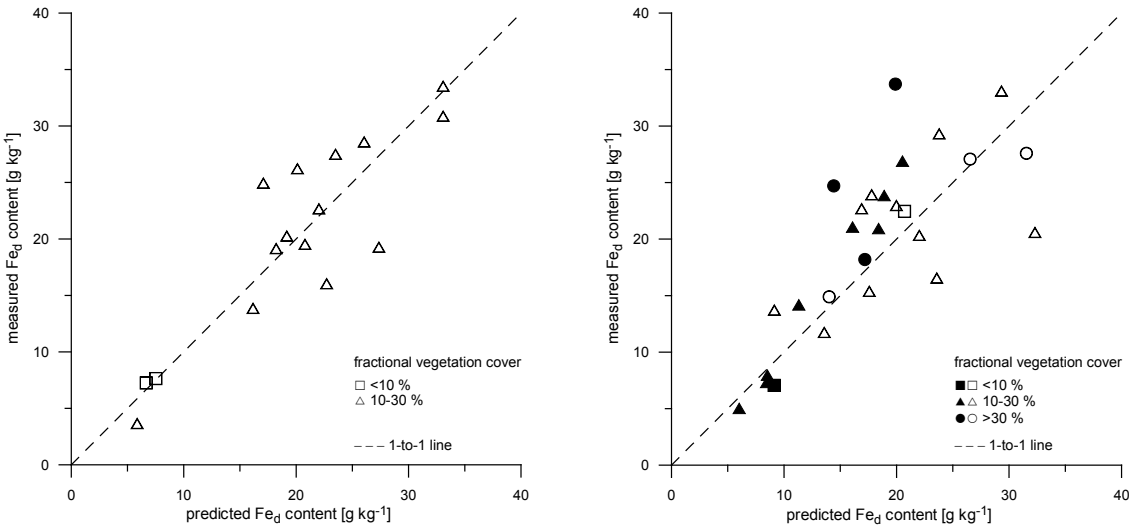

(a) pure soil samples

(b) vegetation-influenced samples

(filled symbols = detectable veg. absorption feature,
unfilled symbol = no detectable veg. absorption feature)

Figure 7.5: Fe_d modeling results indicating µMESMA fractional vegetation cover.

The fractional vegetation cover of the other 14 samples that were categorized "pure soils" in the field ranges between 2 and 26 % based on unmixing analysis. This illustrates the general challenge for spectral mixing analysis procedures to perform absolute quantification which were described to deliver at the best "relative" contributions of each endmember (Chabrillat et al. 2000). An additional difficulty was the spectral similarity of dry vegetation and soils in the VIS/NIR wavelength region which was preferably discriminated by their SWIR absorption features (cellulose, clay, carbonates). However, the µMESMA algorithm design accounted for these difficulties by pixel-wise optimization of the used endmembers based on relevant spectral absorption features, e.g. chlorophyll absorption, clay-OH absorption and cellulose absorption among others (Bachmann 2007).

Both, SMA algorithms and the absorption feature-based approach depend on the detectability of material-specific spectral characteristics. While the spectral feature-based approach directly derives vegetation absorption features from the hull-normalized image without additional calculations, SMA uses a more complex modeling to determine the fractional abundance of each material in the image pixel. The potential use of the SMA algorithm as indicator for vegetation impact on Fe_d prediction accuracy was not favored, because reliable quantitative estimations of especially low vegetation cover were not achieved.

Chapter 8: **Conclusion and outlook**

The overall goal of this thesis was the determination of pedogenic iron oxide (citrate-dithionite extractable iron oxide content - Fe_d) from spectral reflectance measurements at laboratory and image scale. The influence of soil texture and vegetation cover on Fe_d prediction accuracy was examined as main soil surface-related impact factors in a sensitive semi-arid area in southern Spain.

The laboratory spectroscopic investigations were performed on 50 soil samples collected in the semi-arid Cabo de Gata-Níjar Natural Park. Strong relationships were found between Fe_d content and diagnostic iron absorption bands. The increase of Fe_d content caused more intensive iron absorption bands in the VIS (~520 nm) and NIR (~900 nm) wavelength region and showed significant correlations with extracted spectral absorption features, such as depth, width and area of absorption. The spectral influence of different soil textures on the reflectance spectra simulated by different grain sizes (2-mm sieved vs. homogenized) for a single soil sample showed the characteristic brightness decrease and increase of absorption band depth with increasing grain size as reported in other studies. However, the contrary behavior (deeper Fe-VIS and Fe-NIR absorption bands for finer-grained soils) was found when comparing the reflectance spectra of two soils with different textures (sand-dominated vs. clay-dominated) but identical chemical composition. This was attributed to different optical sensitivity of the iron oxides in both soil texture groups and multiple light reflection between the individual grains on the sample surfaces (Richter et al. 2009). Alteration in the samples spectral reflectance, however, may also be triggered by variable hematite/goethite ratio or Fe_t/Fe_d ratio in the soils. Due to the insufficient number of Fe_t analyses (only 13 of 50 soil samples) and the lack of detailed mineralogical analysis of the samples, this examination could not be performed in the frame of this study.

Texture-dependent prediction models were developed using the hull-normalized depths of both Fe-VIS and Fe-NIR absorption bands. They yielded reliable Fe_d estimates with high

accuracy, low prediction error and exhibited high model stability (clay-silt Fe-VIS model: R^2_v=0.813, $RMSE_v$=3.59; sand Fe-NIR model: R^2_v=0.875, $RMSE_v$=2.72). For the subsequent hyperspectral image analysis, texture-independent models were calibrated based on the same input parameter of all soil samples. The evaluation of the prediction results confirmed the high stability of these models (Fe-VIS: R^2_v=0.772, $RMSE_v$=3.98; Fe-NIR: R^2_v=0.755, $RMSE_v$=3.74). The slightly lower prediction accuracy reflected the high textural variability of the samples. The heterogeneous grain size and iron oxide distribution in the samples, the latter caused by the different ways of iron binding in the finer-grained soil, were identified as potential cause.

To determine the spatial distribution of Fe_d concentration in the Cabo de Gata-Níjar Natural Park from HyMap image data, the texture-independent Fe_d model was employed because a pixel-wise determination of predominant texture was not possible. The model was recalibrated on the basis of 17 soil samples reflecting pure soil surface in the image data for the use of the 876 nm waveband absorption depth as predictor variable. The excellent prediction accuracy (R^2_v=0.803, $RMSE_v$=3.69) and slightly better performance in comparison to the laboratory models was attributed to the homogenization of small scale variations due to the size of the HyMap pixel (25 m² per pixel). The application of texture-dependent models would be feasible for soil surfaces with known texture such as sand dunes. Highly accurate Fe_d predictions would be expected. Nevertheless, in this study soil texture variations had negligible impact on the Fe_d prediction accuracy from the image data. Rather, the size of aggregated soil particles was responsible for variation of the results. The Fe_d model performance and prediction accuracy were affected by sensor and surface-related factors. Besides spatial and spectral resolution especially the SNR and quality of radiometric data correction were decisive for the predictions quality.

The vegetation impact on the Fe_d prediction accuracy was examined with laboratory spectral measurements of soil surfaces with varying leaf cover and leaf vitality status. In general, a decrease of the iron absorption band intensity and an albedo increase in the NIR and SWIR wavelength region was found for increasing leaf cover. A decreasing albedo of VIS region was only examined in the presence of chlorophyll absorption features. Chlorophyll absorption was found to overlap the Fe-VIS band for leaf covers greater than 10 % which limited the application of Fe-VIS based prediction models significantly. The Fe-NIR absorption region was partly overlapped by 970-nm plant water absorption band for green leaf covers exceeding 20 %. The caused shift of the absorption maximum position from 910 nm (Fe-NIR) to 970 nm (plant water) was a suitable indicator for green

vegetation influence. The use of a single fixed wavelength from the plant water unaffected left shoulder of the Fe-NIR absorption region allowed Fe_d prediction also for higher leaf cover independent of its vitality status. The appearance of the cellulose-lignin absorption (~2100 nm), usually when leaf cover exceeded 20 %, indicated distinct dry vegetation influence on Fe_d prediction results.

An influence of green vegetation on the soil surfaces could not be determined in the image. The vegetation impact on Fe_d prediction results from the HyMap data was therefore evaluated based on the detectability of cellulose-lignin absorption in the image pixels. Three Fe_d prediction accuracy levels were defined. An excellent accuracy was determined for the pure soil surfaces of agricultural fields. From other soil surfaces without detectable vegetation absorption features a high Fe_d prediction accuracy was achieved, while adequate accuracy resulted from soil surfaces with detectable vegetation absorption features. Based on the laboratory and image findings, more comprehensive and systematic investigations are needed for a quantification of vegetation impact on iron absorption bands. This should include measurements of different soil surfaces with variable vegetation cover, status and geometries.

The final Fe_d content map was used to determine soil surface status and potentially eroded soil profiles. Based on a soil profile analysis, these eroded surfaces can be identified by the joint occurrence of pedogenic iron oxides and carbonates. Both parameters form in lower soil horizons above carbonate-free parent material and appear on the soil surface after overlying soil layers were removed. Two areas with eroded surfaces were identified in surroundings of Casas los Precillas and on the quaternary alluvial fan near La Isleta. Monitoring over time will enable an assessment of the surfaces stability.

Reflectance spectroscopy is a rapid, timely, less expensive and non-destructive method to quantify physical and chemical soil properties and therefore of growing interest in the soil science community. The thesis showed that robust material specific absorption features can be used to derive rather simple models defined by a limited number of input parameters. These models proved to be accurate and have the potential to be successfully applied to other regions. Current and future hyperspectral airborne (e.g. AVIRIS, HyMap, CASI, AISA, ARES, APEX) and spaceborne systems (e.g. CHRIS-PROBA, Hyperion, EnMAP, Hyper-5, HYPSEO) will have sufficient spectral and radiometric resolution to determine the spatial distribution of Fe_d concentration over wide areas directly based on the Fe-NIR

band. As with most empirical-statistical models, adapting the current Fe_d prediction model to other study areas will require model calibration on a limited number of samples to adjust for local soil conditions. In consequence, the Fe_d content for a large number of samples can be estimated with good accuracy within short time and reduced costs.

It is envisioned that the method developed in this thesis can be applied to other semi-arid and arid regions, where vegetation is sparse and soils are largely exposed. Determining Fe_d spatially is an important issue since it can support the evaluation of current soil development over large areas with limited laboratory analysis. Through periodic observation of a specific area, spatial changes in the pedogenic iron oxide content can be located at an early stage and associated with soil surface processes, such as erosion and deposition. Besides that, the pedogenic iron oxide concentration is a suitable indicator for evaluating the relative age of soil as is accumulates with time and continuous pedogenesis. In this context also other iron extracts beside citrate-dithionite extractable iron, e.g. oxalate-soluble iron oxides (Fe_o) or total iron oxide (Fe_t) content, are of interest for soil scientists. Their joint analysis with Fe_d allows the evaluation of complex pedogenic processes and conditions for example by calculating several iron ratios (Birkeland 1999). Hence the potential of reflectance spectroscopy and especially spectral absorption feature analysis for the determination of Fe_o and Fe_t will be undoubtedly in focus of further research.

Economic geology and planetary science are also strongly interested in the analysis and quantification of iron oxides. In economic geology, the type and quantity of iron oxides are important indicators for various types of deposits, including iron and ilmenite, iron oxide copper-gold deposits and porphyry type deposits. The latter one is associated with hydrothermal alterations such as phyllic, argillic, potassic and propylitic all containing hydroxyl minerals. At the same time, an oxide zone is developing over many of the porphyry bodies, which are rich in iron oxide minerals. These alteration minerals can be detected by remote sensing techniques. Hydroxyl and iron oxide minerals can be identified through remote sensing techniques (Rutz-Armenta and Prol-Ledesma 1998; Tangestani and Moore 2001).

Planetary surfaces have been surveyed for many years with hyperspectral imagery (Mars: ISM on Phobos-2, OMEGA on Mars Express, CRISM on MRO; Venus: VIRTIS on Venus Express; Saturn: VIMS on Cassini). The mapping of the Martian surface, which is covered with a variety of iron oxides, has been in focus of research over the last decades (Sherman

et al. 1982; Chevrier et al. 2006). For example, the Mars Express OMEGA instrument revealed a significant amount of sulfates and ferric oxides in the region of Aram Chaos (Massé et al. 2008) that suggest that certain depositional processes, revealed by erosion, have been at work. These identifications are based mostly on the identification of absorption bands in VIS, NIR and SWIR, and on spectral feature extraction methods such as the ones developed in this thesis.

Chapter 9: **References**

Aguilar, J., Fernández, J., Rodrígez, T., Sánchez, J.A., & Fernández, E. (1990). Proyecto Lucdeme. Mapa de Suelos Escala 1:100.000. El Cabo de Gata - 1059 y El Pozo de los Frailes - 1060: Ministerio de Agricultura, Pesca Y Alimentación and ICONA and Universidad de Granada.

Aguilar, J., Fernández, J., Sánchez, J.A., De Haro, S., & Fernández, E. (1989). Proyecto Lucdeme. Mapa de Suelos Escala 1:100.000. Carboneras - 1046: Ministerio de Agricultura, Pesca Y Alimentación and ICONA and Universidad de Granada.

Alados, C.L., ElAich, A., Papanastasis, V.P., Ozbek, H., Navarro, T., Freitas, H., Vrahnakis, M., Larrosi, D., & Cabezudo, B. (2004a). Change in plant spatial patterns and diversity along the successional gradient of Mediterranean grazing ecosystems. *Ecological Modelling, 180*, 523-535.

Alados, C.L., Pueyo, Y., Barrantes, O., Escos, J., Giner, L., & Robles, A.B. (2004b). Variations in landscape patterns and vegetation cover between 1957 and 1994 in a semiarid Meditarranean ecosystem. *Landscape ecology, 19*, 545-561.

Alados, C.L., Pueyo, Y., Giner, L., Navarro, T., Escós, J., Barroso, F., Cabezudo, B., & Emlen, J. (2003). Quantitative characterization of the regressive ecological succession by fractal analysis of plant spatial patterns. *Ecological Modelling, 163*, 1-17.

Aranda, V., & Oyonarte, C. (2005). Effect of vegetation with different evolution degree on soil organic matter in a semi-arid environment (Cabo de Gata-Nijar Natural Park, SE Spain). *Journal of Arid Environments, 62*, 631-647.

Arduino, E., Barberis, E., Ajmone Marsan, F., Zanini, E., & Franchini, M. (1986). Iron oxides and clay minerals within profiles as indicators of soil age in northern Italy. *Geoderma, 37*, 45-55.

ASDI (2002). ASD FieldSpec Pro User's Guide. Analytical Spectral Devices Inc. Boulder, CO, USA

Bachmann, M. (2007). Automatisierte Ableitung von Bodenbedeckungsgraden durch MESMA-Entmischung. Würzburg: Bayerischen Julius-Maximilians-Universität Würzburg.

Backhaus, K., Erichson, B., Plinke, W., & Weiber, R. (1990). *Multivariate Analysemethoden: eine anwendungsorientierte Einführung*. Berlin: Springer-Verlag.

Bahrenberg, G., Giese, E., & Nipper, J. (1999a). *Statistische Methoden in der Geographie. Band 1: Univariate und bivariate Statistik*. Stuttgart, Leipzig: B.G. Teubner

Bahrenberg, G., Giese, E., & Nipper, J. (1999b). *Statistische Methoden in der Geographie. Band 2: Multivariate Statistik*. Stuttgart, Leipzig: B.G. Teubner

Bartholomeus, H.M., Epema, G., & Schaepman, M. (2007). Determining iron content in Mediterranean soils in partly vegetated areas, using spectral reflectance and imaging spectroscopy. *International Journal of Applied Earth Observation and Geoinformation, 9*, 194-203.

Baumgardner, M.F., Silva, L.F., Biehl, L.L., & Stoner, E.R. (1985). Reflectance properties of soil. *Advances in Agronomy, 38*, 2-44.

Bech, J., Rustullet, J., Garrigo, J., Tobias, F.J., & Martinez, R. (1997). The iron content of some red Mediterranean soils from northeast Spain and its pedogenic significance. *Catena, 28*, 211-229.

Beisl, U., Strub, G., & Dickerhof, C. (2000). Validation of hyperspectral imaging data from the Barrax test site with BRDF ground measurements in the reflective wavelength range. *2nd EARSeL Workshop on Imaging Spectroscopy*, Enschede: (p. 9).

Beiso, D. (2002). Overview of Hyperion on-orbit instrument performance, stability, and artifacts. In IEEE Computer Society (Ed.) *Proceedings of the 31st Applied Imagery Pattern Recognition Workshop*, Washington, DC, USA: (pp. 95-101).

Ben-Dor, E. (2002). Quantitative remote sensing of soil properties. *Advances in Agronomy, 75*, 173-243.

Ben-Dor, E., & Banin, A. (1990). Diffuse reflectance spectra of smectite minerals in the near infrared and their relationship to chemical composition. *Science Géologique Bulletin, 43*, 117-128.

Ben-Dor, E., Goldlshleger, N., Benyamini, Y., Agassi, M., & Blumberg, D.G. (2003). The spectral reflectance properties of soil structural crusts in the 1.2- to 2.5-µm spectral region. *Soil Science Society of America Journal, 67*, 289-299.

Ben-Dor, E., Inbar, Y., & Chen, Y. (1997). The reflectance spectra of organic matter in the visible near-infrared and short wave infrared region (400-2500 nm) during a controlled decomposition process. *Remote Sensing of Environment, 61*, 1-15.

Ben-Dor, E., Irons, J.R., & Epema, G.F. (1999). Soil reflectance. In Rencz, A.N. (Ed.) *Remote sensing for the Earth sciences: Manual of remote sensing* (pp. 111-188). New York: John Wiley & Sons Inc.

Ben-Dor, E., Levin, N., Singer, A., Karnieli, A., Braun, O., & Kidron, G.J. (2006). Quantitative mapping of the soil rubification process on sand dunes using an airborne hyperspectral sensor. *Geoderma, 131*, 1-21.

Ben-Dor, E., Patkin, K., Banin, A., & Karnieli, A. (2002). Mapping of several soil properties using DAIS-7915 hyperspectral scanner data a case study over clayey soils in Israel. *International Journal of Remote Sensing, 23*, 1043-1062.

Ben-Dor, E., & Singer, A. (1987). Optical density of vertisol clay suspensions in relation to sediment volumes and dithionite-citrate-bicarbonate-extractable iron. *Clays and Clay Minerals, 35*, 311-317.

Birkeland, P.W. (1999). *Soils and Geomorphology*. New York: Oxford University Press Inc.

Bronstein, I.N., Semendjajew, K.A., Musiol, G., & Mühlig, H. (2000). *Taschenbuch der Mathematik*. Frankfurt am Main: Verlag Harri-Deutsch.

Brown, D.J., Shepherd, K.D., Walsh, M.G., Mays, M.D., & Reinsch, T.G. (2006). Global soil characterization with VNIR diffuse reflectance spectroscopy. *Geoderma, 132*, 273–290.

Bullard, J.E., & White, K. (2002). Quantifying iron oxide coatings on dune sands using spectrometric measurements: An example from the Simpson-Strzelecki Desert, Australia. *Journal of Geophysical Research, 107*, 2125– 2138.

Caballero, E., Reyes, E., Huertas, F., Linares, J., & Pozzuoli, A. (1991). Early-stage smectites from pyroclastic rocks of Almeria (Spain). *Chemical Geology, 89*, 353-358.

Chabrillat, S., Pinet, P.C., Ceuleneer, G., Johnson, P.E., & Mustard, J.F. (2000). Ronda peridotite massif: Methodology for its geological mapping and lithological discrimination from airborne hyperspectral data. *International Journal of Remote Sensing, 21*, 2363-2388.

Chang, C.W., Laird, D.A., Mausbach, M.J., & Hurburgh Jr., C.R. (2001). Near-infrared rerflectance spectroscopy - Principle components regression analysis of soil properties. *Soil Science Society of America Journal, 65*, 480-490.

Chevrier, V., Roy, R., Le Mouélic, S., Borschneck, D., Mathé, P.E., & Rochette, P. (2006). Spectral characterization of weathering products of elemental iron in a Martian atmosphere: Implications for Mars hyperspectral studies. *Planetary and Space Science, 54*, 1034-1045.

Clark, R.N. (1995). Reflectance spectra. In Ahrens, T.J. (Ed.) *AGU Reference Shelf 3, Rock Physics and Phase Relations: A Handbook of Physical Constants* (pp. 178-188). Washington, USA: American Geophysical Union.

Clark, R.N. (1999). Spectroscopy of rocks and minerals, and principles of spectroscopy. In Rencz, A.N. (Ed.) *Manual of remote sensing, Remote sensing for the earth sciences* (pp. 3-58). New York, NY, USA: John Wiley & Sons.

Clark, R.N., King, T.V.V., Klejwa, M., Swayze, G.A., & Vergo, N. (1990). High spectral resolution reflectance spectroscopy of minerals. *Journal of Geophysical Research, 95*, 12653-12680.

Clark, R.N., & Roush, T.L. (1984). Reflectance spectroscopy: Quantitative analysis techniques for remote sensing applications. *Journal of Geophysical Research, 89*, 6329-6340.

Clark, R.N., Swayze, G.A., & Gallagher, A. (1993). Mapping minerals with imaging spectroscopy. *U.S. Geological Survey, Office of Mineral Resources Bulletin, 2039*, 141-150.

Cocks, T., Jenssen, T., Steward, A., Wilson, I., & Schields, T. (1998). The HyMap airborne hyperspectral sensor: the system, calibration, and performance. In Schaepman, M. (Ed.) *Proceedings of the First EARSeL Workshop on Imaging Spectroscopy*, Zurich, 37-42.

Cohen, M., Mylavarapu, R.S., Bogrekci, I., Lee, W.S., & Clark, M.W. (2007). Reflectance spectroscopy for routine agronomic soil analysis. *Soil Science, 172*, 469-485.

Cornell, R.M., & Schwertmann, U. (1996). *The iron oxides*. Weinheim: VCH Verlagsgesellschaft mbH.

Cunningham, C.G., Arribas Jr., A., Rytuba, J.J., & Arribas, A. (1990). Mineralized and unmineralized calderas in Spain; Part I, evolution of the Los Frailes Caldera. *Mineralium Deposita, 25*, 21-28.

Curran, P.J. (1989). Remote sensing of foliar chemistry. *Remote Sensing of Environment, 30*, 271-278.

Diouf, A., & Lambin, E.F. (2001). Monitoring land-cover changes in semi-arid regions: remote sensing data and field observations in the Ferlo, Senegal. *Journal of Arid Environments, 48*, 129-148.

Dunn, B.W., Beecher, H.G., Batten, G.D., & Ciavarella, S. (2002). The potential of near-infrared reflectance spectroscopy for soil analysis - a case study from the Riverine Plain of south-eastern Australia. *Australian Journal of Experimental Agriculture, 42*, 607-614.

Elvidge, C.D. (1990). Visible and near infrared reflectance characteristics of dry plant materials. *International Journal of Remote Sensing, 11*, 1775-1795.

FAO (2005). Guidelines for soil description. Rome: FAO.

Fernández-Soler, J.M. (2001). Volcanics of the Almería Province. In Mather, A.E. (Ed.) *A field guide to the neogene sedimentary basins of the Almería province, SE Spain* (pp. 58-88). Oxford: Blackwell Science.

Fontes, M.P.F., & Carvalho Jr., I.A. (2005). Color attributes and mineralogical characteristics, evaluated by radiometry, of highly weathered tropical soils. *Soil Science Society of America Journal, 69*, 1162-1172.

Gaffey, S.J. (1986). Spectral reflectance of carbonate minerals in the visible and near infrared (0.35-2.55 microns): Calcite, aragonite, and dolomite. *American Mineralogist, 71*, 151-162.

Geerken, R. (1991). Informationspotential von spektral hochauflösenden Fernerkundungsdaten für die Identifizierung von Mineralen und Gesteinen: Laborversuche und Anwendungsbeispiele in der Geologie. Karlsruhe: University of Karlsruhe.

Goldshleger, N., Ben-Dor, E., Benyamini, Y., & Agassi, M. (2004). Soil reflectance as a tool for assessing physical crust arrangement of four typical soils in Israel. *Soil Science, 69*, 677-687.

Grove, C.I., Hook, S.J., & Paylor, E.D. (1992). *Laboratory reflectance spectra of 160 minerals, 0.4 to 2.5 micrometers*, JPL Publication, 92-2. National Aeronautics and Space Administration - Jet Propulsion Laboratory.

Habermeyer, M., Müller, A., Holzwarth, S., Richter, R., Müller, R., Bachmann, M., Seitz, K.-H., Seifert, P., & Strobl, P. (2005). Implementation of the automatic processing chain for ARES. In Zagajewski, B. & Sobczak, M. (Eds.), *Proceedings of the 4th*

workshop on imaging spectroscopy: New quality in environmental studies, Warsaw, Poland, 87-95.

Harvey, A.M., Silva, P.G., Mather, A.E., Goy, J.L., Stokes, M., & Zazo, C. (1999). The impact of Quaternary sea-level and climatic change on coastal alluvial fans in the Cabo de Gata ranges, southeast Spain. *Geomorphology, 28*, 1-22.

Haubrock, S., Chabrillat, S., Lemmnitz, C., & Kaufmann, H. (2008). Surface soil moisture quantification models from reflectance data under field conditions. *International Journal of Remote Sensing, 29*, 3-29.

Hill, J., & Schütt, B. (2000). Mapping complex patterns of erosion and stability in dry Mediterranean ecosystems. *Remote Sensing of Environment, 74*, 557-569.

Holmgren, G.G.S. (1967). A rapid citrate-dithionite extractable iron procedure. *Soil Science Society America Proceedings, 31*, 210-211.

Huete, A.R. (1987). Soil-dependent spectral response in a developing plant canopy. *Agronomy Journal, 79*, 61-68.

Huete, A.R., Jackson, R.D., & Post, D.F. (1985). Spectral response of a plant canopy with different soil backgrounds. *Remote Sensing of Environment, 17*, 37-53.

Hunt, G.R. (1977). Spectral signatures of particulate minerals in the visible and near infrared. *Geophysics, 42*, 501-513.

Hunt, G.R., & Ashley, R.P. (1979). Spectra of altered rocks in the visible and near infrared. *Economic Geology, 74*, 1613-1629.

Hunt, G.R., & Salisbury, J.W. (1970). Visible and near-infrared spectra of minerals and rocks: I. Silicate minerals. *Modern Geology, 1*, 283-300.

Hunt, G.R., & Salisbury, J.W. (1971). Visible and near-infrared spectra of minerals and rocks: II. Carbonates. *Modern Geology, 2*, 23-30.

Hunt, G.R., Salisbury, J.W., & Lenhoff, C.J. (1971). Visible and near-infrared spectra of minerals and rocks: III. Oxides and hydroxides. *Modern Geology, 2*, 195-205.

Instituto Geologico y Minero de Espana (1983). Mapa geologico de Espana.

Jarmer, T. (2005). Der Einsatz von Refexionsspektrometrie und Satellitenbilddaten zur Erfassung pedochemischer Eigenschaften in semi-ariden und ariden Gebieten Israels. Trier: University of Trier.

Jarmer, T., Hill, J., & Mader, S. (2007). The use of hyperspectral remote sensing data for the assessment of chemical properties of dryland soils in SE Spain. *5th EARSeL Workshop on Imaging Spectroscopy*, Bruges, Belgium, p. 8.

Jarmer, T., Lavee, H., Sarah, P., & Hill, J. (2009). Using reflectance spectroscopy and Landsat data to assess soil inorganic carbon in the Judean Desert (Israel). In Röder, A. & Hill, J. (Eds.), *Recent Advances in Remote Sensing and Geoinformation Processing for Land Degradation Assessment. ISPRS Book Series* (pp. 227-241). London: Taylor & Francis.

Junta de Andalucía (2005). Modelo Digital del Terrano de Andalucía. Relieve y Orografía: Junta de Andalucía.

Junta de Andalucía (2006). Climate data for Almería [online]. Available from: http://www.juntadeandalucia.es/agriculturaypesca/estacionesAgroclimaticas/ListadoEstaciones.jsp?CODPROVINCIA=4 [accessed 18.08.2006].

Karnieli, A., Shachak, M., Tsoar, H., Zaady, E., Kaufman, Y., Danin, A., & Porter, W. (1996). The effect of microphytes on the spectral reflectance of vegetation in semiarid regions. *Remote Sensing of Environment, 57*, 88-96.

Kaufmann, H., Segl, K., Chabrillat, S., Hofer, S., Stuffler, T., Müller, A., Richter, R., Schreier, G., Haydn, R., & Bach, H. (2006). EnMAP – A Hyperspectral Sensor for Environmental Mapping and Analysis (invited paper). *IEEE International Geoscience and Remote Sensing Symposium (IGARSS 2006) & 27th Canadian Symposium on Remote Sensing,* Denver, Colorado, USA, p. 3.

Klute, A. (1986). Methods of soil analysis. Part 1. Physical and mineralogical methods. Madison (WI): ASA and SSSA Publisher.

Krüger, G., Erzinger, J., & Kaufmann, H. (1998). Laboratory and airborne reflectance spectroscopic analyses of lignite overburden dumps. *Journal of Geochemical Exploration, 64*, 47-65.

Lagacherie, P., Baret, F., Feret, J.-B., Madeira, J., & Robbez-Masson, J.M. (2008). Estimation of soil clay and calcium carbonate using laboratory, field and airborne hyperspectral measurements. *Remote Sensing of Environment, 112*, 825-835.

Latorré, J.G., García-Latorré, J., & Sanchez-Picón, A. (2001). Dealing with aridity: socio-economic structures and environmental changes in an arid Mediterranean region. *Land Use Policy, 18*, 53-64.

Lillesand, T.M., & Kiefer, R.W. (1994). *Remote sensing and image interpretation*. John Wiley & Sons, Inc.

Machette, M. (1985). Calcic soils of the southwestern United States. In Geological Society of America (Ed.) *Soils and Quaternary geology of the southwestern United States* (pp. 1-21). Boulder, Colorado, USA: Geological Society of America.

Malley, D.F., Martin, P.D., & Ben-Dor, E. (2004). Application in Analysis of Soils. *Agronomy Monograph, 44*, 729-785.

Margate, D.E., & Shrestha, D.P. The use of hyperspectral data in identifying "desert-like" soil surface features in Tabernas area, Southeast Spain. *22nd Asian Conference on Remote Sensing*, 2001. Singapore (pp. 736-741).

Martens, H., & Næs, T. (1989). *Multivariate calibration*. Chichester, New York: John Wiley & Sons.

Martín, J.M., Braga, J.C., & Betzler, C. (2003). Late Neogene-Recent uplift of the Cabo de Gata volcanic province, Almería, SE Spain. *Geomorphology, 50*, 27-42.

Massé, M., Le Mouélic, S., Bourgeois, O., Combe, J.-P., Le Deit, L., Sotin, C., Bibring, J.-P., Gondet, B., & Langevin, Y. (2008). Mineralogical composition, structure, morphology, and geological history of Aram Chaos crater fill on Mars derived from OMEGA Mars Express data. *Journal of Geophysical Research, 113*, E12006, p.15.

McBratney, A.B., Minasny, B., & Viscarra Rossel, R. (2006). Spectral soil analysis and inference systems: A powerful combination for solving the soil data crisis. *Geoderma, 136*, 272-278.

McFadden, L.D., & Hendricks, D.M. (1985). Changes in the content and composition of pedogenic iron oxyhydroxides in a chronosequence of soils in southern California. *Quaternary Research, 23*, 189-204.

Mirabella, A., & Carnicelli, S. (1992). Iron oxide mineralogy in red and brown soils developed on calcareous rocks in central Italy. *Geoderma, 55*, 95-109.

Morris, R.V., Lauer, H.V., Lawson, C.A., Gibson Jr., E.K., Nace, G.A., & Stewart, C. (1985). Spectral and other physicochemical properites of submicron powders of Hematite (α-Fe_2O_3), Maghematite (γ-Fe_2O_3), Magnetite (Fe_3O_4), Goethite (α-FeOOH), and Lepidocrocite (γ-FeOOH). *Journal of Geophysical Research, 90*, 3126-3144.

Murphy, R.J., & Wadge, G. (1994). The effects of vegetation on the ability to map soils using imaging spectrometer data. *International Journal of Remote Sensing, 15*, 63-86.

Nagler, P.L., Daughtry, C.S.T., & Goward, S.N. (2000). Plant litter and soil reflectance. *Remote Sensing of Environment, 71*, 207-215.

Nagler, P.L., Inoue, Y., Glenn, E.P., Russ, A.L., & Daughtry, C.S.T. (2003). Cellulose absorption index (CAI) to quantify mixed soil-plant litter scenes. *Remote Sensing of Environment, 87*, 310-325.

Navarro, T., Alados, C.L., & Cabezudo, B. (2006). Changes in plant functional types in response to goat and sheep grazing in two semi-arid shrublands of SE Spain. *Journal of Arid Environments, 64*, 298-322.

Nordstorm, K.D., & Alpers, C.N. (1999). Geochemistry of acid mine waters. In Plumlee, G.S. & Logsdon, M.J. (Eds.), *The environmental geochemistry of mineral deposits. Part A: Processes, techniques and health issues* (pp. 133-160). Littleton, CO, USA: Society of Economic Geologists.

Orlov, D.S. (1966). Quantitative patterns of light reflection by soils I. influence of particle (aggregate) size on reflectivity. *Biologicheskiye Nauki, 4*, 206-210.

Oyonarte, C., Mingorance, M.D., Durante, P., Pinero, G., & Barahona, E. (2007). Indicators of change in the organic matter in arid soils. *Science of the Total Environment, 378*, 133-137.

Page, A.L., Miller, R.H., & Keeney, D.R. (1982). *Methods of soil analysis. Part 2*. Madison (WI): ASA and SSSA Publisher.

Palacios-Orueta, A., Pinzón, J.E., & Ustin, S.L. (1999). Remote sensing of soils in the Santa Monica Mountains: II. Hierarchical foreground and background analysis. *Remote Sensing of Environment, 68*, 138-151.

Palacios-Orueta, A., & Ustin, S.L. (1998). Remote sensing of soil properties in the Santa Monica Mountains: I. Spectral analysis. *Remote Sensing of Environment, 65*, 170-183.

Parfitt, R.L., & Childs, C.W. (1988). Estimation of forms of Fe and Al: A review, and analysis of contrasting soils by dissolution and Moessbauer methods. *Australian Journal of Soil Research, 26*, 121-144.

Paruelo, J.M., Piñeiro, G., Oyonarte, C., Alcaraz, D., Cabello, J., & Escribano, P. (2005). Temporal and spatial patterns of ecosystem functioning in protected arid areas in southeastern Spain. *Applied Vegetation Science, 8*, 93-1012.

Peinado, M., Alcaraz, F., & Martinez-Parras, J.M. (1992). *Vegetation of Southeastern Spain*. Berlin, Stuttgart: J. Cramer.

Perez-Trejo, F. (1994). *Desertification and land degradation in the European Mediterranean*. EUR 14850 EN, Luxembourg: Office for Official Publications of the European Communities.

Richter, N., Chabrillat, S., Daebel, A., & Kaufmann, H. (2006). Experimental and methodological development for the determination of soil properties in land degradation studies using imaging spectroscopy (No. 07555). *Geophysical Research Abstracts, 8*, p. 2.

Richter, N., Jarmer, T., Chabrillat, S., Oyonarte, C., Hostert, P., & Kaufmann, H. (2009). Free iron oxide determination in Mediterranean soils using diffuse reflectance spectroscopy. *Soil Science Society of America Journal, 73*, 72-81.

Richter, N., Staenz, K., & Kaufmann, H. (2008). Spectral unmixing of airborne hyperspectral data for baseline mapping of mine tailings areas. *International Journal of Remote Sensing, 29*, 3937-3956.

Richter, R., & Schläpfer, D. (2002). Geo-atmospheric processing of airborne imaging spectrometry data, part 2: Atmospheric / topographic correction. *International Journal of Remote Sensing, 23*, 2631-2649.

Rutz-Armenta, J.R., & Prol-Ledesma, R.M. (1998). Techniques for enhancing the spectral response of hydrothermal alteration minerals in Thematic Mapper images of Central Mexico. *International Journal of Remote Sensing, 19*, 1981-2000.

Rytuba, J.J., Arribas Jr., A., Cunningham, C.G., McKee, E.H., Podwysocki, M.H., Smith, J.G., Kelly, W.C., & Arribas, A. (1990). Mineralized and unmineralized calderas in Spain; Part II, evolution of the Rodalquilar caldera complex and associated gold-alunite deposits. *Mineralium Deposita, 25*, 29-35.

Sachs, L. (2002). *Angewandte Statistik. Anwendung statistischer Methoden*. Springer-Verlag GmbH.

Salisbury, J.W., & Hunt, G.R. (1968). Martian surface materials: Effect of particle size on spectral behavior. *Science*, 365-366.

Scheffer, F., & Schachtschabel, P. (2002). *Lehrbuch der Bodenkunde*. Heidelberg, Berlin: Spektrum Akademischer Verlag.

Scheinost, A.C., & Schwertmann, U. (1999). Color identification of iron oxides and hydroxysulfates: Use and limitations. *Soil Science Society of America Journal, 63*, 1463-1471.

Schläpfer, D., & Richter, R. (2002). Geo-atmospheric processing of airborne imaging spectrometry data, part 1: Parametric orthorectification. *International Journal of Remote Sensing, 23*, 2609–2630.

Schwertmann, U. (1988). Occurrence and formation of iron oxides in various pedoenvironments. In Stucki, J.W. (Ed.) *Iron in Soils and Clay Minerals* (pp. 267-308). München: D. Reidel Publishing Company.

Selige, T., Böhner, J., & Schmidhalter, U. (2006). High resolution topsoil mapping using hyperspectral image and field data in multivariate regression modeling procedures. *Geoderma, 136*, 235-244.

Serbin, G., Daughtry, C.S.T., Hunt Jr, E.R., Reeves III, J.B., & Brown, D.J. (2008). Effects of soil composition and mineralogy on remote sensing of crop residue cover. *Remote Sensing of Environment, 113*, 224-238.

Sherman, D.M., Burns, R.G., & Burns, V.M. (1982). Spectral characteristics of the iron oxides with application to the martian bright region mineralogy. *Journal of Geophysical Research, 87*, 10169-10180.

Stoner, E.R., & Baumgardner, M.F. (1981). Characteristic variations in reflectance of surface soil. *Soil Science Society of America Journal, 45*, 1161-1165.

Stoner, E.R., Baumgardner, M.F., Biehl, L.L., & Robinson, B.F. (1980). *Atlas of soil reflectance properties*, Research Bulletin 962, Purdue/LARS Technical Report 111579. West Lafayette, Indiana, USA: Agricultural Experiment Station, Purdue University.

Tangestani, M.H., & Moore, F. (2001). Comparison of three principal component analysis techniques to porphyry copper alteration mapping: A case study, Meiduk area, Kerman, Iran. *Canadian Journal of Remote Sensing, 27*, 176-181.

Torrent, J., Schwertmann, U., Fechter, H., & Alferez, F. (1983). Quantitative relationships between soil color and hematite content. *Soil Science, 136*, 354-358.

van der Meer, F. (1995). Spectral reflectance of carbonate mineral mixtures and bidirectional reflectance theory: Quantitative analysis techniques for application in remote sensing. *Remote Sensing Reviews, 13*, 67-94.

Weijermars, R. (1991). Geology and tectonics of the Betic Zone, SE Spain. *Earth-Science Reviews, 31*, 153-236.